



OPTIMIZATION OF A MULTILAYER  
PHOTOTHERMAL SENSOR FOR  
INFRARED SPECTROSCOPY

THESIS

Janine O.J. Wiggins, Lieutenant, USAF  
AFIT/GAP/ENP/99M-16

19990402 026

DEPARTMENT OF THE AIR FORCE  
AIR UNIVERSITY  
**AIR FORCE INSTITUTE OF TECHNOLOGY**

Wright-Patterson Air Force Base, Ohio

DTIC QUALITY INSPECTED 2

DISTRIBUTION STATEMENT

**DISTRIBUTION STATEMENT A**  
Approved for Public Release  
Distribution Unlimited

OPTIMIZATION OF A MULTILAYER  
PHOTOTHERMAL SENSORS FOR  
INFRARED SPECTROSCOPY.

THESIS

Janine O. J. Wiggins, Lieutenant, USAF

AFIT/GAP/ENP/99M-16

Approved for public release; distribution unlimited

## DISCLAIMER

The views expressed in this thesis are those of the author and do not reflect the official policy or position of the Department of Defense or the U.S. Government.

OPTIMIZATION OF A MULTILAYER PHOTOTHERMAL SENSOR FOR  
INFRARED SPECTROSCOPY

THESIS

Presented to the Faculty of the Graduate School of Engineering  
of the Air Force Institute of Technology

Air Education and Training Command

In Partial Fulfillment of the Requirements for the  
Degree of Master of Science in Nuclear Engineering.

Janine O. J. Wiggins

Lieutenant, USAF

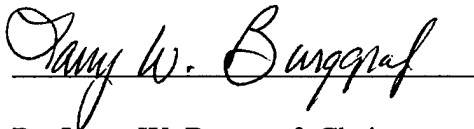
March 1999

Approved for public release, distribution unlimited.

OPTIMIZATION OF A MULTILAYER PHOTOTHERMAL SENSOR FOR  
INFRARED SPECTROSCOPY

Janine O. J. Wiggins, B.S.  
Lieutenant, USAF

Approved:



Dr. Larry W. Burggraf, Chairman  
Associate Professor of Engineering Physics

8 Mar 1999

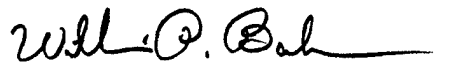
Date



Dr. William F. Bailey  
Associate Professor of Physics

8 Mar 99

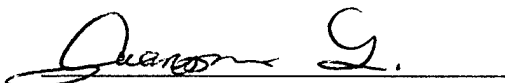
Date



Dr William P. Baker  
Associate Professor of Mathematics

8 Mar 99

Date



Dr Guangming Li  
Senior Research Assistant

8 Mar 99

Date

## Acknowledgements

I give honor to God, who is the head of my life, to His son Jesus Christ, who died to set me free, and to the precious Holy Spirit, who dwells within me. For, "except the Lord buildeth a house, he who labors does so in vain." God is truly good to His children, and I would not have made it through without Him.

I am deeply indebted to my advisor, Dr Larry Burggraf, for his counsel and guidance, to Dr Guangming Li, for his patience, Dr Baker for lending me a small bit of his intelligence, and Dr Bailey for calling me out on weak points of my theory. I must say that this thesis project has given me a new respect for those who do this work for a living!

I give thanks to my husband, Steven Wiggins, for his love and support in this endeavor, even though he would have preferred me at his side. Absence makes the heart grow fonder, right?

And finally, I would like to thank all of the members of Bread of Life, Church of the Living God International for lifting me up when I was down, encouraging me to work when I didn't feel like it, and being there to feed this ever-starving graduate student. I especially want to thank my Pastors, Kenneth and Beverly Baker and Cornelius Hudson, also Ministers Buason Hudson, Maurice and Andrea Spriggs. And what would I have done for stress relief if not for the children? Maurissa, Dominique, Malachi, and Tahzje. The Hotel is always open for you.

Janine O. J. Wiggins

# Table Of Contents

	Page
Acknowledgements .....	ii
Abstract .....	v
1. Introduction .....	1.1
Background .....	1.1
Problem Statement .....	1.4
Research Focus .....	1.4
Research Concerns/Hypotheses .....	1.4
Methodology .....	1.6
Testing .....	1.7
Integration of Reed into System .....	1.8
Assumptions/Limitations .....	1.8
Implications .....	1.9
2. Review .....	2.1
Historical Perspective .....	2.1
Static Mechanical Analysis .....	2.3
Solution to the Thermal Model .....	2.5
Summary of the Thermal Solution .....	2.9
Dynamic Mechanical Modeling .....	2.10
3. Methodology .....	3.1
Experimental Procedure .....	3.1
Preparation of Reed Sensor .....	3.1
Testing with the AFM .....	3.1
Measurement .....	3.2
Determination of Parameters .....	3.3
Mathematical Modeling .....	3.3
Software Package .....	3.3
Approximations .....	3.4
Inputs .....	3.4
Outputs .....	3.4
Typical Values .....	3.5
4. Results .....	4.1
Model Results .....	4.1
Optimum Thickness Ratio .....	4.1
Resonant Frequency .....	4.2
The Thermal Solution .....	4.2
Thermal Solution Applied to Mechanical Model .....	4.4
Phase Lag .....	4.8
Signal to Noise Ratio (SNR) .....	4.9
Experimental Results .....	4.10
Long Vs Short Reed Sensors .....	4.10

Resonance Frequency.....	4.10
Deflection Decrease With Increased Absorber .....	4.11
Mirror .....	4.13
Base .....	4.13
Position of the Light Beam.....	4.14
Reliability.....	4.15
Comparison of Model and Experimental Results .....	4.16
5. Conclusions .....	5.1
Implications of Model Results .....	5.1
Implications of Experimental Results .....	5.1
Conclusion.....	5.1
Suggestions for Further Research .....	5.2
 Bibliography.....	 BB.1
 Appendix A. Useful Data.....	 A.1
 Appendix B. Derivation of the Solution to the Thermal Problem .....	 B.1
 Appendix C. Mathematical Model.....	 C.1
 Vita.....	 V.1



Abstract

Mathematical modeling and atomic force microscopy were used to optimize a multi-layer reed sensor for use in a new infrared detection system. The reed sensor is designed to deflect in response to temperature variations. In this system, a sample absorbs infrared light (modulated at some frequency to reduce noise) and releases heat into the reed. The layers expand differently, causing the reed to deflect. The deflection is influenced by geometric parameters, such as length and thickness of each layer, and also by the frequency of modulation. Deflection is easily measured using an atomic force microscope. This research applied a mathematical model to the reed sensor, explored the effect of varying geometric parameters, and used experimental testing to evaluate the model. Several reeds were tested to validate the model, which predicted sensitivity, maximum deflection, resonance frequency, and signal to noise ratio. Varying concentrations of absorbing chemical were deposited in the reed, to cause a change in deflection.

A cantilever reed having three layers was modeled mathematically using a recently developed thermal model and a mechanical model based on two-layer theory. The predictions mirror theory-based expectations in that for each reed there was an optimum modulating frequency. Also, the model was able to predict optimum thickness ratios, and was used to gain insight into the phase shift behavior of reed deflection.

This model behavior is in line with laboratory experiments, with some exceptions. The model correctly predicts temperature behavior, but currently does not provide accurate quantitative results. The model is found lacking for short, squarer reeds not having the assumed aspect ratio of 10. This type of reed oscillated in higher order modes

than were considered in the mathematical model. To accurately represent these, the thermal and mechanical behavior must be derived using plate theory rather than beam theory. The model is also inadequate in describing the effects of thickening the top layer, probably because it assumes uniform energy deposition throughout the layer. Finally, the deflection signal was observed to decrease with increased concentration of sample deposited.

Sponsor: US Army CBDCOM

# OPTIMIZATION OF A MULTILAYER PHOTOTHERMAL SENSOR FOR INFRARED SPECTROSCOPY

## 1. Introduction

### Background

Several branches of the military have joined in an effort to improve their water contamination detection systems. Some important system requirements are summarized below [10: 1-3]:

- Detect and quantify specified chemical and biological agents
- Achieve Parts-Per-Billion (PPB) Detection level
- Field operability by military personnel
- Be portable by one individual.

This system must be rugged, small, and have rapid measurement capability.

Infrared detectors have good selectivity for measuring a wide variety of agents. Because they are based on measuring very small differences in large signals, current infrared detectors are too noisy at room temperature to be useful in this military application. AFIT proposes to meet this challenge via a new photothermal infrared detection system.

The principle behind this new system is simple. A sample is captured in nanopores in magnesium aluminate, which is the top layer of a cantilever reed (refer to Figure 1 below). To search for a particular contaminant, light of an appropriate wavelength is directed onto the reed. Nanoporous magnesium aluminate, also known as sol-gel, was chosen as the top layer because it is transparent in the IR and near IR. The

chemicals of interest to the military are typically responsive to wavelengths in IR and near IR light. If the contaminant is present, light will be absorbed and re-released as heat. Heat flows to the other layers of the cantilever reed, which expand differently, according to the difference in their thermal expansion coefficients. Because the layers are tightly bound together at the interfaces, the net effect is the bending of the reed. Deflection, then, should be a direct measure of how much contaminant is present in the sol-gel layer.

The novel part of the system is the reed upon which those contaminants are deposited. The reed is made of several layers, beginning with a nanoporous magnesium aluminate (sol-gel,  $\text{MgAl}_2\text{O}_4$ ) layer, typically one micron in thickness. Next is a thin (about 200 Angstroms) layer of gold, followed by layers of silicon, typically eight microns, and aluminum, typically half a micron. The sol-gel layer entraps molecules of the sample to be examined; the gold layer conducts heat to the remainder of the reed, and effectively isolates the silicon and aluminum layers from the stiff sol-gel layer. Deflection is dominated by the expansion of the bottom two layers, with aluminum expanding about ten times more than silicon. Deflection measurement response to wavelength of light provides a quantitative measurement of the quantity of pollutant trapped. The figure below (Figure 1.1) shows this multi-layer reed as used in the laboratory. The sample is located in the sol-gel layer. The reed is held to its silicon base by a clamp and is covered by a reflector, which forces the incoming light to make repeated passes over the reed sensor.

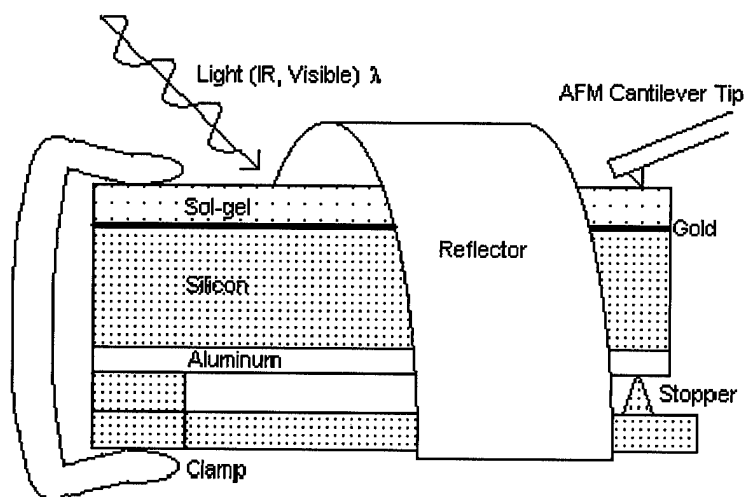


Figure 1.1: Cantilever Reed Design (not to scale)

The sol-gel material was chosen for the first layer because it was available in nanoporous form (which easily traps the sample molecules) and because it is relatively transparent to infrared light [11: 38]. Silicon also absorbs infrared light, as will be discussed later.

There are several systems available for measurement of the cantilever reed deflection. In-house testing using a fiber interferometer was successful, but complicated compared to measurements with an atomic force microscope (AFM). In this project, deflection was measured using the AFM, which employs a photodiode and laser beam (combined to produce a position-sensitive detector), focused on the 100-micron AFM cantilever tip in contact with the end of the reed sensor. This system is small, does not need the cryogenics required by current infrared detectors, and is expected to detect samples at parts-per-billion concentrations. Thus, the system as it currently stands meets all of the system requirements listed earlier, with the exception of the parts-per-billion level of detection. This requirement should be met once the system has been optimized.

Essential in producing the best possible detector is the optimum reed design. The best reed is as thin as possible, while maintaining rigidity. Also, it must be long and wide enough to capture a sufficient amount of sample, but not so long as to be overly sensitive to low frequency noise. Geometric parameters such as thickness, length and width of each layer will be varied and the performance of each reed will be evaluated using models and laboratory testing.

### **Problem Statement**

This research is concerned with optimizing a cantilever reed for use in this photothermal infrared measurement system. Mathematical modeling and laboratory testing of these reeds is used to gain an understanding of how a change in the cantilever reed geometry affects sensitivity. The goal is to increase sensitivity.

### **Research Focus**

The cantilever reed was modeled mathematically and the deflection response to changes in such parameters as length and thickness of layers were calculated. These models, which include a thermal model of the three important layers and a mechanical model based on two-layer theory, predicted sensitivity, maximum deflection, resonance frequency, and signal to noise ratio, all of which must be balanced when determining the optimum reed parameters. Several reeds, of varying dimensions, were constructed and tested to validate the mathematical model.

### **Research Concerns/Hypotheses**

The first step in increasing sensitivity of the reed is minimizing noise sources. Absorption of the IR light by the silicon layer, rather than by the sample trapped within the sol-gel layer, produces a background signal many times larger than the deflection signals due to the sample. Silicon shows strong absorption in the IR, with a prominent band at 1.2 microns.

A silicon filter placed between the light source and the three-layer reed can reduce this problem, by removing the wavelengths of light absorbed by silicon. This would reduce the overall deflection, because less light is hitting the reed, but would increase the percentage of deflection associated with the sample itself.

One proposal to prevent the IR light from exciting the silicon was to use a layer of gold between the sol-gel and the silicon layers. This gold layer would reflect the IR beam back through the sol-gel. This turned out to require too thick a layer, as thick as the wavelength of light used. The presence of the gold, however, helped eliminate the following mechanical problem. The sol-gel material has twice the thermal expansion of silicon. Table A.1 of the Appendix A presents material properties for each of the layers. The sol-gel is also expected to heat up the most because it receives the incoming light directly but loses heat slowly because of its small thermal conductivity and diffusivity. The sol-gel will expand *more* than the silicon. This would cause downward deflection, unless the aluminum absorbs enough energy to force the reed upward. This concern is practically eliminated by the use of the gold layer, which is assumed to be ductile enough to mechanically isolate the stiff sol-gel layer from the silicon/aluminum combination.

This assumption of mechanical isolation of the sol-gel, due to the presence of the gold layer, also simplifies modeling. It is thin enough and conductive enough that it need

not be included in thermal modeling of the reed. Because gold is both ductile and conductive, it essentially separates the sol-gel layer from the other layers, while efficiently conducting heat into the silicon. Thus, two-layer mechanical models may be used, circumventing development of a more complicated multi-layer model. Of course, the solution still requires a three-layer *thermal* solution to determine correct temperature distribution.

Sensitivity of the detector is increased when operating at the mechanical resonant frequency of the reed. At this frequency, the reed deflects strongly with even small changes in temperature. Operating near this frequency makes the reed more sensitive to both temperature change and noise [12: 2486]. Comparison of signal-to-noise ratio (SNR) on and off mechanical resonance frequency was expected to favor operation at the mechanical resonance.

Another way to increase the sensitivity of the reed is to increase its length. Deflection and sensitivity (deflection divided by input energy) are both directly related to length [4: 32]. The difference in length between expanded layers will be increased for a longer reed, and the longer reed will have a larger surface area to trap more pollutant, if other factors are held constant. Increasing the length means that each layer will expand more, resulting in greater deflection. Unfortunately, lengthening the reed can lower the resonant frequency, making the reed is extremely sensitive to low frequency noise.

## **Methodology**

These effects are better understood by using a mathematical model to describe behavior of the reed. First, the diffusion of heat between each of the layers must be



determined. The mechanical portion of the problem then uses the thermal solution to determine deflection and phase lag information.

Current two-layer reed thermal models are inadequate because they describe only the static case [2: 3793, 15: 83]. A dynamic solution is required to describe the deflection amplitude and phase lag resulting from the reed's dynamic temperature change.

Mechanical isolation of the sol-gel allows use of the two-layer mechanical equations, given the correct three-layer temperature distribution.

A model has recently been developed by Dr William Baker, Associate Professor of Mathematics at the Air Force Institute of Technology, to describe thermal behavior of a three-layer reed. It is presented in Chapter 2. Once the model has been used to predict optimum dimensions, several reeds near the optimum reed size can be fabricated and tested.

Testing. Error in deflection measurement was reduced using a chopper to modulate the IR beam. A lock-in amplifier provided phase and amplitude information. Later in the project, faster digital filter methods were developed to improve accuracy of deflection amplitude measurement. Amplitude of the output signal is proportional to the amplitude of the deflection, as expected. Phase information is related to the rate of heat transfer through the sol-gel layer. Phase lag arises from the thermal diffusion rate through layers of the reed. The sol-gel makes the largest contribution to phase lag, because of its small thermal diffusion. Phase lag increases with increased modulation frequency of the IR light.

The modulation frequency was varied and the corresponding deflection and phase lag responses were observed. Varying concentrations of absorbing chemical were

deposited in the reed, to cause a change in deflection. Several reed lengths were tested, with the shorter reeds expected to produce less noisy deflection data.

Integration of Reed Into System. Originally, adhesive was used to attach the reed to the base, but the methanol solvent used to dissolve the absorber (pyridine) dissolved the glue and caused the reeds to fall off. Currently, a clamp is used to attach the reed to its base. This method is undesirable because the clamps themselves tend to shear the reeds at the point of contact. Although this loss can be minimized with careful closing of the clamp, it is better to find a less forceful method of keeping the reed on the base.

A mirror/reflector can increase the deflection signal from the reed. This mirror, typically placed above the reed, would reflect the IR beam back toward the reed. The light beam hits the cantilever reed many times, depositing more energy, and improving sensitivity. Re-usable mirrors of polished brass and aluminum were created and tested.

Silicon is particularly absorptive in the near IR. Heating, due to silicon absorption, causes a deflection response resulting in higher background. A silicon window may solve this problem by absorbing light from the prominent silicon absorption bands before the light hits the reed. This could reduce the background signal when exploring reed properties with a broadband source. Because no mid-IR tunable laser was available, a near IR (from visible to about 8 microns) broad band source was used in this research.

### **Assumptions/Limitations**

The mathematical model assumes that the temperature profile of the reed does not vary with width, and that energy is deposited uniformly in the first layer. Convection and radiation effects are ignored, as are noise sources other than thermal noise. The use of

beam theory to describe the reed sensor requires the aspect ratio (length / width) will always be at least ten and the length to be 24 times greater than thickness. The latter condition is always met within the parameter space of this problem. This former condition is necessary to assume that deflection occurs only as a function of distance down the length of the reed.

Design constraints include the area and wavelength range of the light beam impinging the reed. Width of the reed is bounded on the lower end, by the diameter of the light beam, currently half of a millimeter. A laser source can be focused down to 0.01 mm or less. At these small widths, production constraints define the boundaries. The smallest reed that can be prepared using current techniques is half a millimeter in width and 3 millimeters in length.

### **Implications**

Optimizing the cantilever reed is an important step in the process of optimizing this photothermal infrared detector. The results validate Baker's currently unpublished three-layer thermal equations, presented in Appendix B, which can now be combined with other models so that behavior of even smaller reed sensors can be determined. This research helps AFIT achieve its goals by making the detector more sensitive.

## 2. Review

### Historical Perspective

This is a new application for the position sensitive detection implemented in the atomic force microscope (AFM). Researchers are just now beginning to adapt the cantilever of the AFM itself for use in temperature detection systems.

The AFM measures deflection by measuring the movement of a cantilever whose small tip will be placed on the end of the multi-layer reed. As the reed deflects, the tip is moved up and down. A laser beam directed at the AFM cantilever reflects to a photodiode, which tracks movement of the laser, cantilever and therefore the reed. AFM cantilever properties have been well established, and many of the resulting models apply to other vibrating levers and so can be used in describing the sample laden, multi-layer reed.

In 1997, Moulin, Stephenson and Welland ran a three dimensional model of a two-layer triangular shaped AFM cantilever in order to quantify its mechanical and thermal properties when operating in either air or water. They were able to accurately predict time constant and deflection for bi-layer reeds [9: 590]. Conventional models were using only one of the reed's resonance frequencies and did not account for two-dimensional vibration of the reed. Salapka, et al, used a multi-mode model to characterize the noise present in such measurements, including both additional resonances, and higher modes. These factors were necessary to accurately predict noise in reeds of aspect ratio below eight [12: 2533]. Walters, et al, explored the value of operating in the cantilever's mechanical resonance region and found an increase in signal to noise (S/N) ratio in spite of a marked increase in noise density [14: 3587]. Lai, et al,

optimized a two-layer cantilever for use in a similar thermal sensor. They coated a silicon AFM cantilever with a second layer and measured its deflection response to change in temperature. By optimizing the thickness of the layers, they improved sensitivity by “40% over previous studies” [6: 117].

One notable bit of research is that of J. Barnes, et al reported in 1994. They used a three-layer cantilever in the AFM to measure the presence of a chemical [3: 79]. The multi-layer cantilever was made from a commercially prepared two-layer AFM cantilever (silicon nitride and aluminum) with 140 nm latex spheres deposited on top. They were able to detect samples with this method, claiming a demonstrated sensitivity a factor of 100 higher than previous methods. Though Barnes (et al) measured deflection and resonance response with a third layer, they presented no mathematical description of their reed.

Finally, Burggraf and Li extended the idea to the use of a transparent sol-gel layer on a separate reed [4: 1]. The use of an additional reed increases throughput so that different samples can easily be measured in succession. The  $\text{MgAl}_2\text{O}_4$  sol-gel layer appears to be a good choice because it is transparent in the visible and IR regions of the spectrum (through 7 microns) [11: 38, 5: 21]. The only drawback of using this material is its low thermal diffusion coefficient, which puts a restriction on how fast the IR beam can be modulated. If the beam receives light at too high a frequency, no equilibrium will be reached. Measurement of deflection is made during steady state operation, where the buildup of heat in the top layer equals the amount leaving. No one has yet mathematically characterized the mechanical behavior of multi-layer reeds. Dr William

P. Baker, Associate Professor of Mathematics at the Air Force Institute of Technology has recently developed a description of the thermal behavior of the three-layer reed.

### Static Mechanical Analysis

The fundamental quantities used in describing the mechanical motion of the reed are given below. Additional parameters of interest will be defined as they are discussed. Only the silicon and aluminum layers, layers two and three respectively, are considered in the static analysis of the reed.

*Table 2.1: Definition of Terms*

<u>Name</u>	<u>Quantity</u>	<u>Name</u>	<u>Quantity</u>
z	Vertical deflection (m)	T:	Sensor Temperature (K)
S	Sensitivity (m/W)	K:	Young's Modulus (unitless)
$\alpha_2, \alpha_3$	Thermal Expansion Coefficients (1/K)	L:	Length of the cantilever reed (m)
$\lambda_2, \lambda_3$	Thermal Conductivity (W/(m K))	W:	Width of the cantilever reed (m)
$t_2, t_3$	Thickness (m)	P:	Power absorbed by reed (W)
$T_0$	Ambient Temperature (K)		

Numerical values for each material can be found in the Appendix A. Ambient temperature is that temperature at which the beam lays flat.

Current literature discusses two-layer cantilevers and gives the theory for the static case, where the reed has previously absorbed some amount of energy and has deflected. Assuming that heat losses due to convection and radiation are negligible, the reed sensor can be approximated by a two-layer cantilever acting under uniform (throughout the volume) heating, with an aspect ratio (length / width) of at least ten and a length 24 times greater than thickness [15: 83]. This last condition is always met. If the

required aspect ratio is met, deflection occurs only as a function of  $x$  as defined in Figure 2.1. Deflection of reeds with a smaller aspect ratio depends also on the width axis. The multi-mode mechanical analysis necessary to treat these cases is rather complicated and has only been developed for deflections of single layer cantilevers [12: 2480].

Thickness of the silicon layer is not variable, as these are prefabricated, but the aluminum thickness can be varied. The sol-gel thickness could also be varied using numerical calculations, but was held constant for this modeling. Current reeds are made with a thick silicon layer and a thinner aluminum layer. As the thickness of the aluminum layer is increased, deflection of the reed sensor will also increase [4: 32]. The sensitivity peaks at some optimum value. The sensitivity as a function of the ratio of aluminum thickness to silicon thickness,  $n$ , is [6: 114]:

$$S = \frac{2\alpha_2 L^3 (\beta - 1)(n + 1)}{\lambda_2 t_2^2 w K(n)(\gamma n + 1)} \quad (2.1)$$

where

$$K(n) = 4 + 6n + 4n^2 + \phi n^3 + \frac{1}{\phi n}.$$

Here  $\phi$  is the ratio of the elastic modulus of aluminum to that of silicon,  $\gamma$  is the ratio of thermal, and  $\beta$  is the ratio of thermal expansion coefficients. This equation can be used to determine the optimum thickness of the aluminum layer in terms of the silicon thickness.

By modeling the reed as a lumped-mass spring system, a restorative force (spring) constant,  $k_c$ , and an effective mass of the reed,  $m_{eff}$ , can be used to calculate mechanical

resonant frequency. The following mechanical resonance equations are appropriate for rectangular bi-layer beams with an aspect ratio of at least 8 [13: 13, 23]:

$$k_c = \frac{w}{4L^3} (E_3 t_3^3 + E_2 t_2^3) \quad (2.2)$$

$$m_{eff} = 0.24wL(\rho_3 t_3 + \rho_2 t_2)$$

$$\omega_o = \sqrt{\frac{k_c}{m_{eff}}} = \frac{t_2}{2L^2} \sqrt{\frac{(E_3 n^3 + E_2)}{.24(\rho_3 n + \rho_2)}}$$

For each layer,  $i$ , density is represented by  $\rho_i$ , elastic modulus by  $E_i$ , and thickness by  $t_i$ . Note that with increased mass of material, the resonant frequency will go down.

### Solution to the Thermal Model

During this research, Dr. Baker developed equations describing heat transfer in the reed's layers. They are based on the fundamental heat transfer equation, written for each layer of the reed. A complete derivation can be found in the Appendix B. The origin is placed at the far-left corner of the reed, between the first and second layers, as seen below in Figure 2.1.

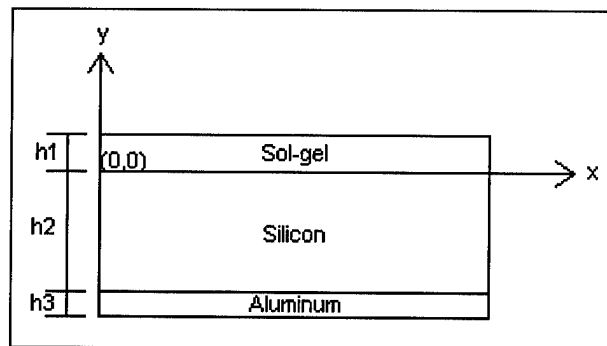


Figure 2.1: Schematic of the Reed



Heat transfer equations, written for all three layers, must be solved to determine the time based temperature profile. Here vertical,  $y$ , and horizontal,  $x$ , directions are modeled. The assumption is made that the temperature profile does not vary with reed width. Convection and radiation remove a negligible amount of heat from the reed and are ignored. Energy is deposited in the first layer by a modulated IR beam at a constant intensity for half of a modulation period. This development assumes uniform energy deposition in the volume of first layer. Also assumed is that the temperature at the left end of the reed is held constant at ambient temperature by the clamp mechanism. This temperature is also the initial temperature of the reed. The other three boundaries of the reed are taken as insulated.

The solutions for each layer are coupled by the additional boundary conditions of continuity of temperature and flux across the interfaces. Let  $w(\xi, \eta, \tau)$  represent a temperature fluctuation from the initial, and ambient, temperature. Here the spatial dimensions have been scaled to the overall length of the reed, that is *length*  $x = L\xi$ , and *depth*  $y = \eta L$ . The thickness of each individual layer is also scaled with respect to the overall length resulting in  $h_i = L\alpha_i$ . Time,  $t$ , is scaled to the period (T) of the modulated IR light beam, or  $t = T\tau$ . The heat transfer equation, describing the fluctuation of temperature from the ambient and written for each layer  $i$ , is:

$$\frac{\partial w^{(i)}(\xi, \eta, \tau)}{\partial \tau} = d_i \nabla^2 w^{(i)}(\xi, \eta, \tau) + \delta_{i,1} F(\tau). \quad (2.3)$$

Here, energy deposition rate from the IR beam is represented as  $F(\tau)$  and is present only in the first layer, hence use of the Kroneker delta,  $\delta_{i,1}$ . The specific function of this

energy source will be considered later. The term  $d_i$  in equation (1) is a scaled diffusion term which includes some constants as a result of scaling:

$$d_i = \frac{TD_i}{L^2}.$$

$D_i$  is the thermal diffusivity for each layer  $i$ . The left end of the reed is held at constant temperature, so the temperature fluctuation,  $w$ , is always zero at  $\xi = 0$ . The reed's top and bottom are insulated, meaning there will be no temperature variation in the vertical ( $y$ ) direction at the top of the sol gel,  $\eta = \alpha_1$ , nor at the bottom of the aluminum layer,  $\eta = -(\alpha_2 + \alpha_3)$ . There is no temperature variation along the horizontal ( $x$ ) at the insulated right end of the reed,  $\xi = 1$ .

Again, the separate equations are coupled by continuity of temperature across the boundaries and continuity of heat flux across the boundaries. Finally, the reed starts, in an undeflected position, at the ambient, initial temperature:  $w^{(i)}(\xi, \eta, 0) = 0$ .

To satisfy boundary conditions at  $\xi = 0, 1$ , the solution will have the form:

$$w^{(i)}(\xi, \eta, \tau) = \sum_{k=0}^{\infty} q_k^{(i)}(\eta, \tau) \text{Sin}(\lambda_k \xi) \quad (2.4)$$

where

$$\lambda_k = (2k + 1) \frac{\pi}{2} \text{ for } k = 0, 1, 2, \dots$$

and  $q_k^{(i)}$  are mode shapes to be determined.

Substituting this solution into the original differential equation, and Laplace transforming the result, yields an equation in  $Q_k^{(i)}(\eta, s) \equiv \mathcal{L}\{q_k^{(i)}(\eta, \tau)\}$ . The solution is easily obtained. Directly inverting the Laplace transform, via calculus of residues,

requires the roots in the transform domain of an algebraic equation (see Appendix B).

These simple roots, labeled  $(-\sigma_k)$ , lie along the negative real axis, and represent the rate of diffusion through the reed. The convolution theorem is used to determine the  $q^{(i)}(\eta, \tau)$ , once the incoming energy is determined. The thermal deposition rate from the IR source,  $F(t)$ , is modulated by a chopper, and takes the form of:

$$F(\tau) = k_a E_0(\tau) = k_a \begin{cases} I_0 & 0 \leq \frac{\tau}{T} \leq t_0 \\ 0 & t_0 < \frac{\tau}{T} < 1 \end{cases} \quad (2.5)$$

Here  $t_0$  represents the fraction of a period,  $T$ , that the beam is turned on. Only a portion,  $k_a$ , of the incident energy,  $E_0$ , is actually converted to heat present in the sol-gel layer. The parameters  $k_a$  (absorption of the sample trapped within the sol-gel layer) and  $I_0$ , (intensity of the incoming energy beam) can be determined experimentally.

Now  $I_k(t)$  is defined by  $I_k(t) = \int_0^t e^{-\sigma_k(t-\tau)} F(\tau) d\tau$  and is found to be

$$I_k(\tau) = \frac{k_a I_0}{\sigma_k} e^{-\sigma_k \tau} \left[ \frac{(e^{\sigma_k t_0} - 1)}{(e^{\sigma_k} - 1)} (e^{\sigma_k p} - 1) - e^{\sigma_k p} \right] + \frac{k_a I_0}{\sigma_k} \begin{cases} 1 & 0 \leq \frac{\tau}{T} \leq t_0 \\ e^{-\sigma_k((\tau-p)-t_0)} & t_0 < \frac{\tau}{T} < 1 \end{cases} \quad (2.6)$$

The first term in  $I_k(t)$  in Equation 2.6 accounts for the build up and decay of energy for each of the previous cycles. The other accounts for the cycling of the current period,  $p$ . Heat in the top layer builds up while the beam is on. Once the beam has shut off ( $\tau/T > t_0$ ), the temperature slowly decays, as heat is transferred to the other layers and the clamp.

Recall that  $(-\sigma_k)$  are roots of the solution in the transform domain, needed to invert the Laplace transform.

Phase analysis can be obtained from the model by noting the time it takes for the temperature to rise and fall to a defined point. A convenient point is half of the magnitude of temperature change.

### Summary of the Thermal Solution.

The final solution for each layer is comprised of a series of solutions. Each series term,  $k$  includes a dynamic description of the energy deposition (Equation 2.6),

modulated in the horizontal ( $x$ ) direction by  $\phi_k(\xi) = \frac{1}{\lambda_k} \text{Sin}(\lambda_k \xi)$ .

The temperature diminishes as it passes through the depth ( $y$ ) of the reed. This behavior, of the scaled temperature, is shown, for each layer  $i$ , by  $\psi_k^i(\eta)$ :

$$\begin{aligned} \psi_k^1(\eta) &= \text{Cos}\left(\frac{\omega_k^{(1)}}{\sqrt{d_1}}(\eta - \alpha_1)\right) \\ \psi_k^2(\eta) &= A_k \text{Cosh}\left(\frac{\omega_k^{(2)}}{\sqrt{d_2}}(\eta + \alpha_2)\right) + B_k \text{Sinh}\left(\frac{\omega_k^{(2)}}{\sqrt{d_2}}(\eta + \alpha_2)\right) \end{aligned} \quad (2.7)$$

where

$$\begin{aligned} A_k &= \text{Cosh}(\omega_k^{(3)} \gamma_3) \\ B_k &= \sqrt{\frac{d_3}{d_2}} \frac{\omega_k^{(3)}}{\omega_k^{(2)}} \text{Sinh}(\omega_k^{(3)} \gamma_3) \\ \psi_k^3(\eta) &= \text{Cosh}\left(\frac{\omega_k^{(3)}}{\sqrt{d_3}}(\eta + \alpha_2 + \alpha_3)\right). \end{aligned}$$

The second layer is far more complex, being trapped between a layer that is constantly introducing more energy into the system (the top) and a layer that quickly equilibrates any temperature differences it sees.

For each unit of energy deposited, there is a temperature change:

$$C_k^{(1)} = \frac{2}{(\omega_k^{(1)})^2 \tilde{D}_k} \left\{ \omega_k^{(2)} \text{Sinh}(\omega_k^{(2)} \gamma_2) \text{Cosh}(\omega_k^{(3)} \gamma_3) + \sqrt{\frac{d_3}{d_2}} \omega_k^{(3)} \text{Cosh}(\omega_k^{(2)} \gamma_2) \text{Sinh}(\omega_k^{(3)} \gamma_3) \right\} \quad (2.8)$$

$$C_k^{(2)} = C_k^{(3)} = 2 \sqrt{\frac{d_1}{d_2}} \frac{\text{Sin}(\omega_k^{(1)} \gamma_1)}{\omega_k^{(1)} \tilde{D}_k}.$$

The function  $\tilde{D}_k$  is defined in Appendix B. For convenience, the following is written:

$$\gamma_i = \frac{\alpha_i}{\sqrt{d_i}} \quad \text{and} \quad \begin{aligned} \sqrt{z_k + d_1 \lambda_k^2} &= i \omega_k^{(1)} \\ \sqrt{z_k + d_2 \lambda_k^2} &= \omega_k^{(2)} \\ \sqrt{z_k + d_3 \lambda_k^2} &= \omega_k^{(3)} \end{aligned}$$

The solution to the thermal behavior for a three-layer reed is then:

$$w(\xi, \eta, \tau) = \sum_{k=0}^{\infty} C_d^{(i)} I_k(\tau) \phi_k(\xi) \psi_k^{(i)}(\eta) \quad (2.9)$$

### Dynamic Mechanical Modeling

The differential equation for the two-layer beam is [15: 118, 2: 3793]:

$$\frac{d^2 z}{dx^2} = 6(\alpha_2 - \alpha_1) \frac{t_1 + t_2}{t_2^2 K} (T - T_o)(x, t) \quad (2.10)$$

The reed is oriented such that the end at  $x = 0$  is fixed and the other, at  $x = L$  is free. The fixed end shows no vertical movement and no slope. Replacing the term (T-

$T_0(x,t)$  with Baker's thermal solution, and solving for the deflection at the top of the reed's free end results in,

$$z_{x=L}(\tau) = 6(\alpha_1 - \alpha_2) \frac{t_1 + t_2}{t_2^2 K} \sum_{k=0}^{\infty} C_d^{(i)} I_k(\tau) \hat{\phi}_k(1) \psi_k^{(i)}(\alpha_1) \quad (2.11)$$

where the functions in the series are defined as before, with the exception of:

$$\hat{\phi}_k(\xi) = \frac{1}{\lambda_k^3} \text{Sin}(\lambda_k \xi) - \frac{\xi}{\lambda_k^2}. \quad (2.12)$$

As mentioned earlier, there are roots associated with each term of the series.

These roots can be viewed as an effective thermal diffusion constant for each mode. The roots for each series of equations must be re-calculated for each parameter change. This makes it difficult to optimize for length, thickness, and operating frequency. To circumvent this problem, and obtain deflection as a function of length and chopper frequency, several approximations were required.

Once the deflection is known, the signal-to-noise ratio (SNR) can be determined, as it is dependent on deflection. This analysis assumes thermal noise dominates all other sources. A two-layer reed sensor, modeled as a spring mass system, will have resonant frequency  $\omega_o$  and spring constant  $k_c$ , when operating at ambient temperature  $T$ . It will have quality factor  $Q$ , which can be determined by the shape of the first resonance peak. Finally, the signal to noise ratio,  $SNR$ , is [13: 31]:

$$SNR = z_{x=L} \sqrt{\frac{Q^2 k_c \omega_o}{4 k_b T}} \quad (2.13)$$

where  $k_b$  is the Boltzmann constant.

Maximizing the SNR is the basis for optimizing the reed sensor's geometry.

### 3. Methodology

#### **Experimental Procedure.**

Preparation of Reed Sensor. Commercially prepared silicon, with a thickness range of five to ten microns, is cut to size, and an evaporator is used to coat a thin layer of gold on one side. A liquid solution containing the sol-gel materials is dropped onto the gold layer and “spun” in a spinner to achieve a sub-micron thick film. Drying the new reed removes any moisture and some organic impurities present in the sol-gel solution [8: 259].

Finally, the aluminum is evaporated onto the other side of the silicon. The process takes about 10 days, and has been nearly perfected by AFIT technician Ms. Belinda Johnson and Dr. Guangming Li.

Once ready for use, a reed is clamped on a silicon base and inserted into the AFM. The base is represented in Figure 1.1 and consists of one layer secured in the AFM, and two small pieces of silicon at either end. The first piece acts as a spacer, keeping the reed from touching the base. The second, as a stopper at the end of the reed, helps damp unwanted vibrations. As a bonus, this became a suitable platform to measure reed deflection, as the force of the AFM tip will continue to push the reed down, if there is nothing stable below. The AFM can then measure the upward force caused by a change in temperature of the reed once it has a stable platform against which to work.

Testing with the AFM. The AFM was used to measure the deflection response to changes in chopper frequency, wavelength of light, sample concentration and use of a reflector. Unfortunately, small variations in the starting position of the AFM tip prevent

the use of software to subtract out such background and zero signals. A schematic of the laboratory setup is given below:

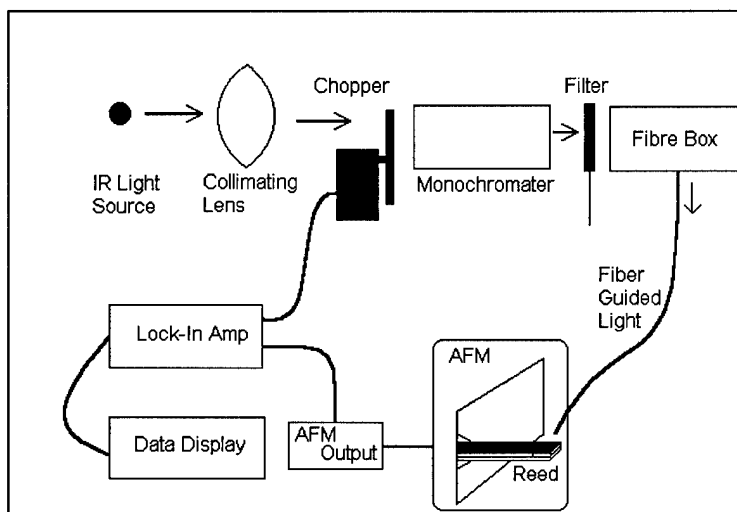


*Figure 3.1 Laboratory Setup*

There are several ways to measure phase and amplitude information. A lock-in amplifier, the standard, but slow, measurement device in this field, provides accurate phase information, but amplitude measurements are highly noisy, due to the laboratory environment. A much faster method to measure amplitude is found in the software accompanying the AFM. Image processing software is able to correct for any tilt of the reed, perhaps owing to variations of the base and stopper heights. The software can also approximate a low pass filter, smoothing out the deflection data and removing power spikes that often throw off the lock-in measurements. Phase information cannot be determined using the AFM without reference to the chopper frequency signal.

Measurement. The light used in most of this analysis was in the visible range. The gratings used were blazed at 500 nm and were relatively inefficient in the 300-400 nm range, but efficient from 500-650. The absorber used in this study was a laser dye, pyridine, which had two absorption peaks: A major peak at 485 nm and a much smaller



peak at about 350 nm. The possibility of attributing deflection peaking from the light source to that resulting from the sample is reduced by taking source spectra to determine the amount of light absorbed by the sample for each wavelength.

Determination of Parameters. The mathematical model will show the trends in reed behavior, but will not provide specific energy, deflection, or absorption predictions without calculating  $k_a$ , the absorption of the sample in the sol-gel layer and  $I_0$ , the intensity of the incoming energy beam. An optical power meter is used to determine the fraction of original energy from the light (90 to 100 Watts) that actually hits the reed. The next step, measuring  $I_0$ , requires measuring the absorption.

### **Mathematical Modeling.**

Software Package. Mathematical modeling was done using the Mathematica software package. Mathematica was chosen mainly for its graphic capabilities. Compared to other popular software packages, it is more user friendly than Fortran, and is able to calculate multiple series and present three-dimensional graphics with far less manipulation than MathCad. Three-dimensional graphics were not heavily used in this research, but it is expected that someone will take over the research and derive relationships involving thickness of the top layer, length, and frequency. These new relationships will produce parameter values for an *optimum* reed, and the relationships will be easier to see with three-dimensional snapshots. This software package does have a distinct disadvantage when working with units, as can be seen in the code presented in Appendix C.

Approximations. Applying the three-layer thermal solution to the two-layer mechanical solution, required use of several approximations and assumptions. First, because the expansion of the second and third layers determines the deflection of the reed, the temperature of the second layer along its top was used to describe the temperature profile of the reed. This profile fed into the deflection equation as presented in the previous chapter. This approach was later validated when the bottom two layers were found to exhibit the same temperature profile.

Parameter space exploration was made difficult by the presence of the root terms, which needed to be re-calculated for each specific reed and chopper frequency. To make the optimization more tractable, approximations were found for the root functions ( $-\sigma_k$ ) and the derivative functions ( $\tilde{D}_k$ ). Approximations for both the roots and the derivative terms were made relative to the baseline case of a reed 0.01 meters in length and operated at 1 Hz (dc). These functions, introduced in the derivation of the thermal solution, were found to follow the simple ratio relationships presented in the fourth chapter.

Inputs. The Mathematica code produced during this project is presented in Appendix C. It requires user knowledge of the reed parameters such as length, thickness and chopper frequency, as well as material properties such as density, elastic modulus, thermal conductivity, thermal expansion, and heat capacity for each layer. Further required quantities, diffusivity for example, can be calculated from those given above.

Outputs. The code calculates first the thermal profile of a given reed and the uses that profile to determine a dynamic deflection profile for the reed under consideration. The static portion of the model can be used to explore resonant frequency, optimum thickness and ratio of the bottom two layers of the reed.

Typical Values. The code has been adapted to be useful over a wide range of reed lengths and chopper frequencies. Most analysis was done for the same case: a reed 2.25 cm long, with the thickness of the three layers (in descending order) being 1 micron, 8 microns, 0.5 micron. The chopper frequency was typically set at 8 hertz. These parameters were used because they were the parameters of the typical reeds used in the laboratory. The absorption coefficient,  $k_a$ , was not determined, and left as unity in many calculations. The degradation of the light signal was accounted for by using values measured in the lab [7: 1].

## 4. Results

### Model Results

Optimum Thickness Ratio. In Chapter 2 we discussed the variation in sensitivity as a function of  $n$ , the ratio of silicon and aluminum thickness. Figure 4.1 below is a plot of sensitivity as a function of the ratio  $n$  and reveals an optimum ratio of  $n = 0.325$ . Thus, for a silicon thickness of 8 microns, the optimum aluminum thickness is 2.6 microns. The aluminum layer cannot be made that thick, as current processing techniques limit the thickness to half a micron. Beyond this thickness, because of the curling following Al evaporation at elevated temperatures, the reed assumes a curled, rather than flat shape as desired.

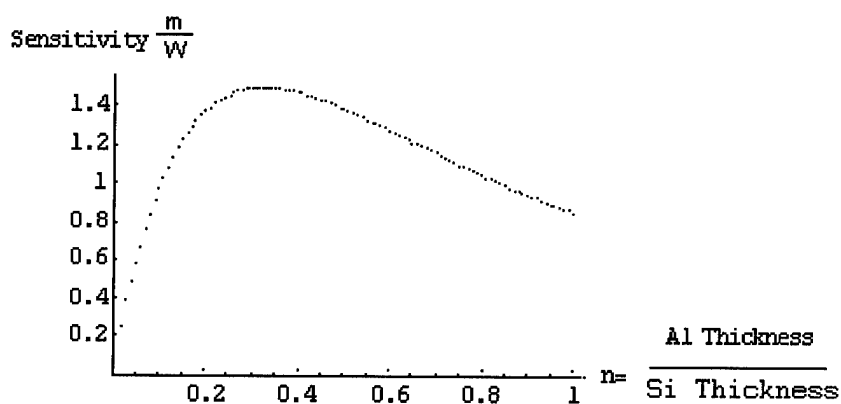


*Figure 4.1 Sensitivity as a Function of (n) From Equation 2.1 Showing Optimum Thickness Ratio*

The silicon thickness is not as constant as desired- being found in the lab to range anywhere from four to sixteen microns. The optimum value for aluminum remains 0.325 regardless of the silicon thickness, another result of static modeling. One way to increase performance of the reed sensor is to use methods that will allow for a larger aluminum thickness.

Resonant Frequency. Static two layer mechanical modeling is used to calculate resonant frequency for a reed of silicon and aluminum. The silicon layer is assumed 8 microns thick, and the aluminum layer takes on values from 0.5 to 8 microns thick. The ratio of aluminum to silicon thickness is noted as  $n$ , according to the resonance equation, Equation 2.2. The resonant frequency has a minimum at where the aluminum thickness = 0.6 of the silicon thickness. This is far too large given current reed production procedures. Other methods of bringing the resonance frequency down to reasonable chopper frequencies must be explored.

### **The Thermal Solution**

Predictions obtained for the dynamic thermal behavior of the reed sensor met expectations. There is a relatively large temperature gradient in the first layer, and the bottom two layers show almost constant temperature. At the end of the reed, the temperature profile is constant throughout all three layers. This condition actually occurs long before the end of the reed, at a point slightly less than half way down. The temperature increases nearly linearly but soon reaches a steady state condition where each layer's temperature oscillates between two constant values. It is this minor vibration that is measured as deflection due to light absorption. This steady state is reached in less than 100 periods. In figure 4.2 the rise to equilibrium can be seen. In figure 4.3, after 200 cycles of the light beam, we see the steady state operation of the reed oscillation.

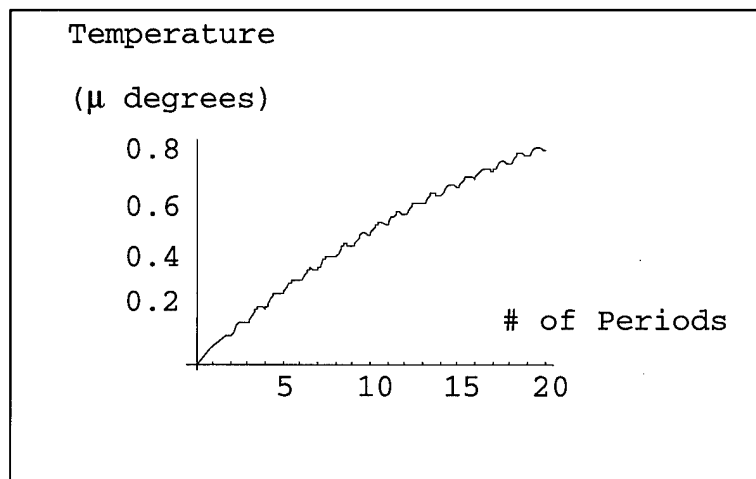


Figure 4.2: Thermal Response of Multi-Layer Reed in Time

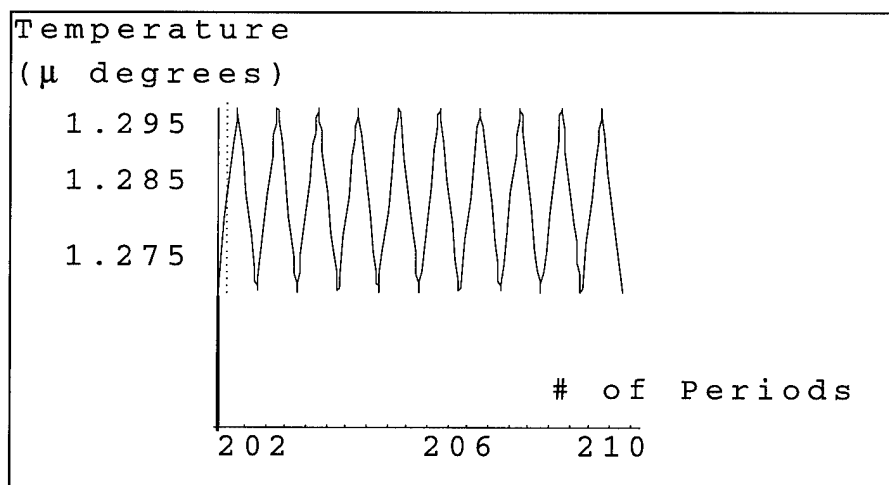
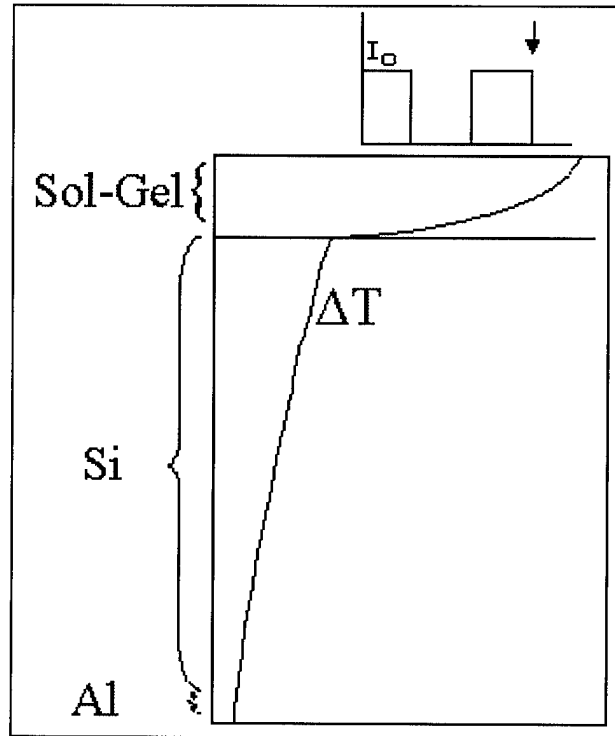


Figure 4.3: Steady State Thermal Behavior of Multi-Layer Reed

During steady state operation, the temperature of the reed just before the start of any period (just before the beam turns on) is constant. The difference in temperatures can be seen in Figure 4.4, which is a plot of the temperature fluctuation as a function of depth into the reed. This snapshot is taken halfway through the 2001<sup>st</sup> period, just as the beam shuts off. At the beginning of the period, the temperature profile had the same shape, but the variation was so slight that it would appear as a straight line, if plotted. The temperature profile is nearly constant when the light begins to strike the beam, but a

difference in profile throughout the depth of the reed quickly develops, peaking when the light turns back off. The calculation was done near the clamped end of the reed to show the maximum temperature difference between the layers.



*Figure 4.4: Temperature Change vs. Depth as Beam Turns Off,  
Steady State Operation*

The difference in temperature between the layers is about  $10^{-10}$  Kelvin for the baseline case mentioned in Chapter 3. The difference in temperature between periods is still small, on the order of  $10^{-8}$  Kelvin. This seemingly small temperature change corresponds to a calculated .01 nm deflection for the typical four-layer reed. Measured deflection values for this reed ranged between 30-200 nm.

Thermal Solution Applied to Mechanical Model. Recall that the thermal solution was an infinite series, each term of which containing a *root* which described the overall heat

transfer of the reed for that mode. These roots had to be numerically recalculated with each change in reed geometry. An analytic representation of these quantities would allow for more convenient application of the thermal and mechanical solutions to the reed sensor problem.

To find such a relationship, these roots were calculated for several different reeds, all compared to a baseline reed 0.01 meters in length modulated at 1 Hertz.. First, plotting the root corresponding to each series term,  $k$ , revealed a *parabolic* relationship in  $k$ . The length was then varied, and the roots were observed to be proportional to *one over square of length* of the reed. Finally, chopper frequency was varied and the roots varied as *one-over-frequency*.

These three effects were combined by first determining the parabolic constants for the roots as a function of  $k$  for the baseline case. That root value is then multiplied by the appropriate ratios in  $L$  and  $\omega$  to determine the value of the root for other lengths and frequencies. The roots ( $-\sigma_k$ ) are then represented by:

$$\sigma_k(k, L, \omega) = \frac{.0001}{\omega L^2} (-2.02072 + 8.19207 * k - 8.20216 * k^2).$$

The term *.0001* has the units Hertz-Square meters, and so the scaled nature of the problem can be maintained by inputting  $L$  in meters and  $\omega$  in Hertz. This term stems from proportions of  $L$  and  $\omega$ , that is, the values  $L = .01$  (roots vary inversely as  $L$  squared)  $\omega = 1$  Hz used in calculating the original parabolic constants.

The derivative terms ( $\tilde{D}_k$ ), introduced in Chapter 2 were also approximated. They too were found to obey simple relationships, but did not show significant variance with  $L$ .  $\tilde{D}_k(k, \omega) = (.0009902715 - 3.328841 * 10^{-9} k - 7.094576316 * 10^{-10} k^2) \sqrt{\omega}$



The  $k$  and  $k^2$  constants above may seem relatively small, but keep in mind that the derivative terms are just as small (on the order of  $10E-4$ ). These small constants make a large difference in approximating higher series terms. The thermal code itself does not require use of series terms higher than 100, but the after approximating the roots and derivatives in this manner, it may become necessary to run the series out to about 200, especially for smaller reeds. Ignoring these tiny terms can result in a 30% error in root terms.

Table 4.1 shows the error introduced when using the data fits. The *Data Point* column shows the conditions under which the root was calculated as follows:

Root [Length in Meters, Chopper Frequency, Series Term].

For example, the first entry represents the root calculation for a reed that was .03 meters long, the chopper frequency was 8 Hertz, and the thermal series was taken out 12 terms. A similar table highlighting the error in the derivative terms is in Appendix A.

*Table 4.1: Error in Roots with Approximation*

Data Point	Actual Root	Approximated Root	%Error
Root[.03,14,12]	-10.1722	-10.1721	.001%
Root[.0225,8,25]	-131.7003	-131.696	.0032%
Root[.01,1,500]	-2.007825*10 <sup>6</sup>	-2.004645*10 <sup>6</sup>	1.9%
Root[.004,29,250]	-106512.	-110041.	3.3%

The variance of the roots and derivatives with respect to length and frequency are based on the change from an initial value, calculated for a reed one centimeter in length modulated at 1 Hz. These approximations allow thermal profile to be determined as a function of length and chopper frequency, and have small error compared to the

predictions obtained by Baker's original equation. The error does grow, however, for very small reeds (less than half a centimeter) at very high series term numbers. The roots at this point are so large that this error hardly effects the overall temperature prediction.

Overall predictions in temperature showed no greater than 1% difference. An important quantity is the difference in temperature that the reed experiences during steady state operation. The approximations modeled this temperature change with an error less than .01%. This study varied the reed length from four millimeters to 25 centimeters and ran the chopper frequency from one Hertz up to about 500 Hertz.

The model calculated the expected temperature profile across the length of the reed (*x direction*), as shown below in Figure 4.5. There are three curves shown in each graph: The lowest curve shows the reed after only one period's worth of light has been absorbed. The middle shows the temperature profile after ten periods have passed, and the highest curve shows the steady state condition resulting after 100 periods have passed. This is temperature in the top layer. The deflection of the reed will be seen in time variations of the height of that steady state curve. The thermal solution and the approximated solution produce the same curves.

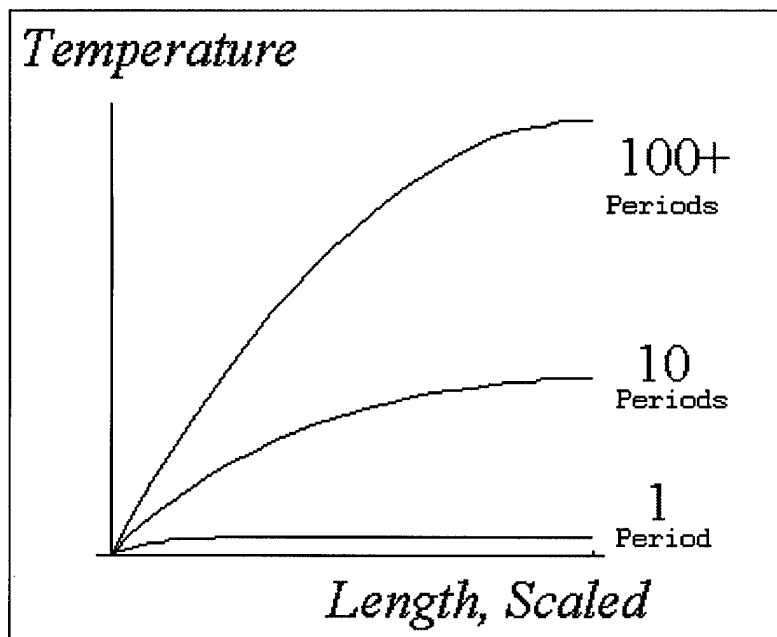


Figure 4.5: Temperature Profile Along Reed Length

### Phase Lag

Phase lag was explored by noting comparing the expanse of time between rise and fall to a specific temperature point. The time at which the reed first heats up to this specific temperature is labeled *t-early*,  $t_e$ , and the time to fall back is labeled *t-late*,  $t_l$ . The change in the difference between these two times for each series term quickly drops to a constant value of one half (See Appendix C). This suggests that accurate phase information can be determined with only the first series (mode) term.

Below is a plot showing combining thermal output of the first layer from two different times. The first curve represents the dynamic temperature profile during the first period. The second was calculated during steady state conditions. Phase in the signal is seen in the difference in the rise and fall of the curve.

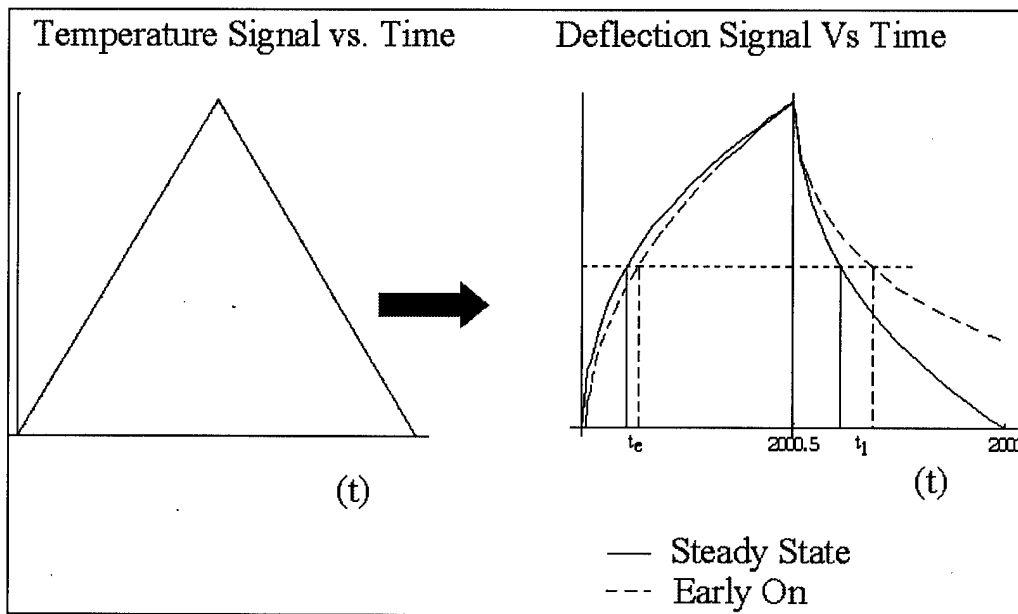


Figure 4.6: Phase Shift of Deflection Signal in Time

Signal to Noise Ratio (SNR). Mathematical modeling produced expected results when tracking the effect of length and frequency on the overall deflection of the reed. As length was increased, total deflection of the reed and noise present increased. As the frequency was increased (beyond mechanical resonance frequency of the reed) the deflection went down.

The model (presented in Appendix C) also shows expected results in that the longer the reed gets, the less sensitive it becomes. Although the deflection of a reed increases along with its length, the longer reeds have very low resonance frequencies. These low frequencies result in a reed sensor that is *very* sensitive to low frequency background noise. SNR was predicted to peak at the resonant frequency and then drop off sharply. The resonant frequency of the long reeds (about 2 cm in length) was as low as our lowest operating frequencies (8Hz) and so resonance peaking was not observed. A three-dimensional plot of predicted SNR, as well as the calculations that produced it, is

presented in Appendix C. For each length, the maximum SNR will be obtained by operating just short of the mechanical resonance frequency of the reed.

## **Experimental Results**

Long Vs Short Reed Sensors. As expected, there was a distinct difference in the signals obtained from small reeds and long reeds. The long reeds (two centimeters and longer) were far more susceptible to acoustic noise, while the short reeds (1.5 centimeters and longer) produced a zero signal except at very low frequencies (due to low frequency noise) and near the resonance frequency. The resonant frequency of the long reeds (about 2 cm in length) was as low as our lowest operating frequencies (8Hz) and so resonance peaking was not observed. Resonance was observed for short reeds, as will be shown later.

Resonance Frequency. The resonant frequency calculations assume that the reed meets beam theory requirements presented in Chapter 2. To see the effect on reeds which violate these requirements, a reed 1.25 centimeters in length and 3 millimeters wide was prepared and tested for its deflection response to chopper frequency. Because the aspect ratio is far from ten (being 4.5), *some* deviation from the predicted resonance of 330 Hertz was expected. Not only did the resonance peak appear at about 425 Hertz, but also the shape of the deflection curve revealed higher order resonances present. This data is presented as below as Figure 4.7. Arrows are placed over the expected and actual resonance peaks. The aspect ratio is so low that beam mechanics no longer apply. The deflection is no longer one-dimensional. There is now resonance behavior across the

width of the reed. To account for this kind of vibration, the thermal and mechanical solutions must be derived using plate mechanics.

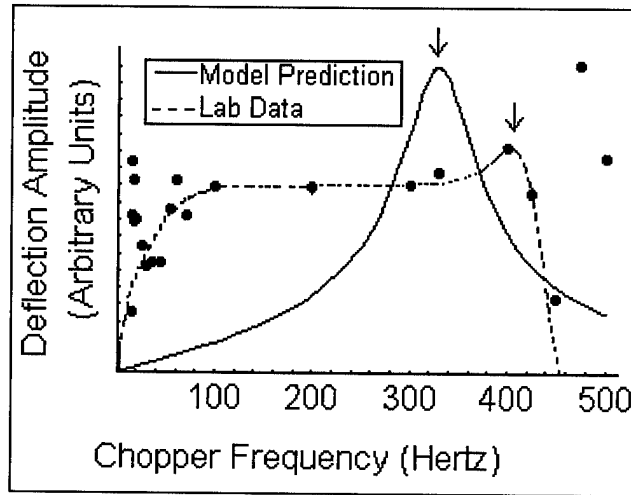


*Figure 4.7: Amplitude of Deflection Signal vs. Chopper Frequency  
for Small Aspect Ratio Reed.*

Deflection Decrease With Increased Absorber. The deflection signal of the reed sensor went down when the amount of absorber went up, as shown below:

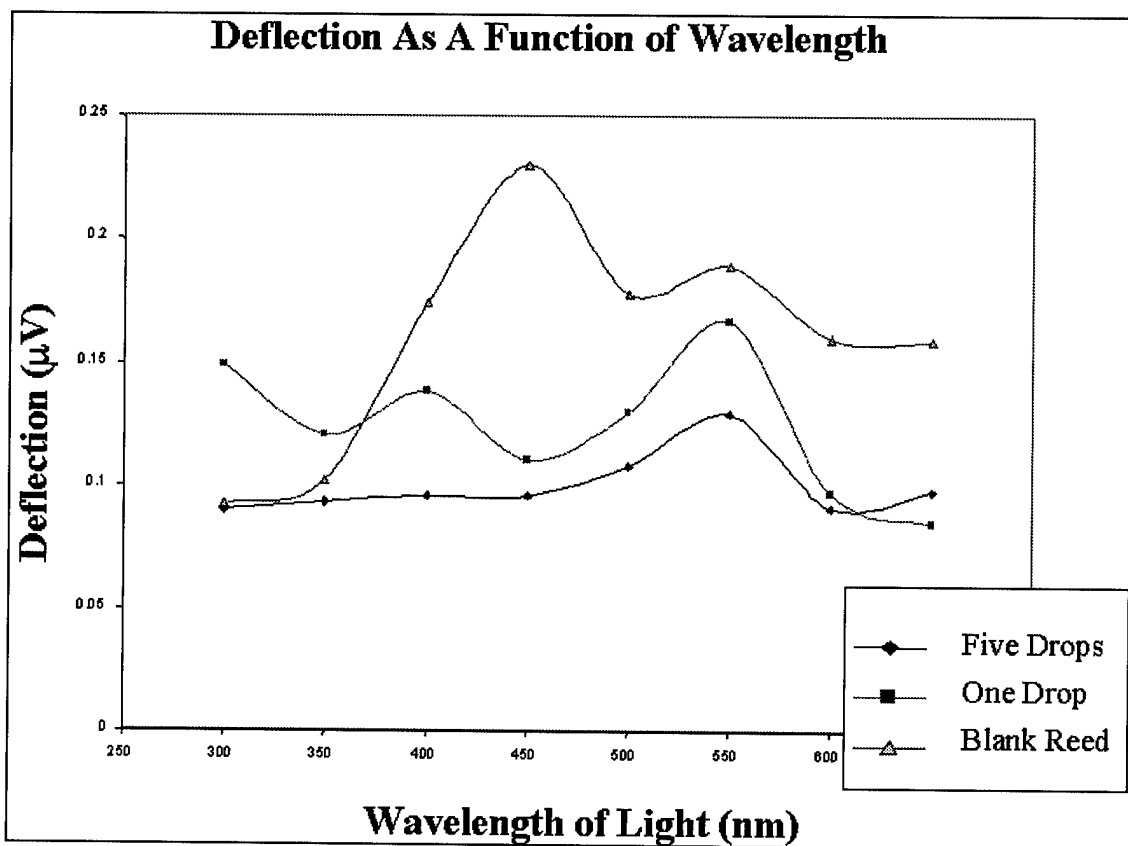


Figure 4.8: Deflection Decreases as Absorber is Increased

There are several likely causes for this. One possibility is that so much of the signal is due to silicon absorption that the absorption of energy by the sample results in less heat transferred to the overall reed. With the absorber on, the silicon itself absorbs less, hence less deflection. Another cause is that the application of the sample to the reed itself. The sample may very well be so thick that the energy absorbed by the top of the sample transfers down through the sol-gel layer and to the rest of the reed. A more likely cause is that the laser dye used did not become “trapped” in the nanopores, but instead formed another layer of its own atop the sol-gel. This addition of mass would be expected to decrease the deflection of the reed.

Mirror. Early on in the project, there was concern that without some sort of mirror or reflector over the cantilever reeds they would not absorb enough energy to deflect noticeably. This is certainly the case, for the monochromator reduces the light several orders of magnitude and the fiber optic line by at least six. Current mirrors are not reliable; made of aluminum foil, they can only be re-used once or twice. Polished brass mirrors were constructed, but tested no better than the aluminum foil.

The mirror had no effect for reeds less than 1.5 centimeters in length. The mirrors were proven effective for longer reeds, and enhanced the deflection signal by about five times. This is probably due to the size of the light beam and the height of the mirror. After hitting the reed once, the light is already exiting the other end of the mirror, as seen below. Lowering the mirror should solve this problem, but the IR beam is currently so wide that the mirror cannot be lowered. To contain the light beam further, a *wall* can be built into the far end. The wall would reflect the light back to its origin and should make the mirror useful for small reeds.

Base. The reed has been held on with a variety of materials, including adhesive and a clamp. The adhesive reacts with the solvent for the laser dye, and so this method was quickly abandoned. The clamp worked well except for the tendency of the jaws to snap down on the reed with too much force, snapping the reed. Also, the lips of the clamp made it hard to fit small reeds into the AFM. This was overcome by filing the lips of the clamp, which made it of proper size, but also made it harder to clamp the reed to the base without snapping the reed. One way of anchoring the reed to the base is to insert the base into the AFM and then lay the reed on top. Massive (relative to the reed) material with similar dimensions to the base is placed on top of this assembly. Small pieces of silicon



were found to be heavy enough to hold the reed in place. This method is by far the easiest on the reed. It is also easier to produce reproducible results as the reed moves far less with placement of this weight than it does with the clamping of the reed.

Position of the Light Beam. In a perfect reed, the heat would be transmitted so quickly that it would not matter where the IR hit. This is not the case, for the diffusion of heat through the first layer is extremely slow. Below is a table showing the results of sampling the reed at three different positions. Position A is closest to the AFM tip, Position B is in the middle of the reed, and Position C is near the base of the reed, where it is clamped down. This test was run on two different reeds: The first, a two-layer reed of silicon (5 microns) and aluminum (0.5 microns) with measurements 2 centimeter x 1.5 mm). The other was a reed of all four layers, sol-gel (1 micron), gold (2 angstrom), silicon (8 microns), and aluminum (0.5 microns) measuring 2.25 cm x 3 mm.

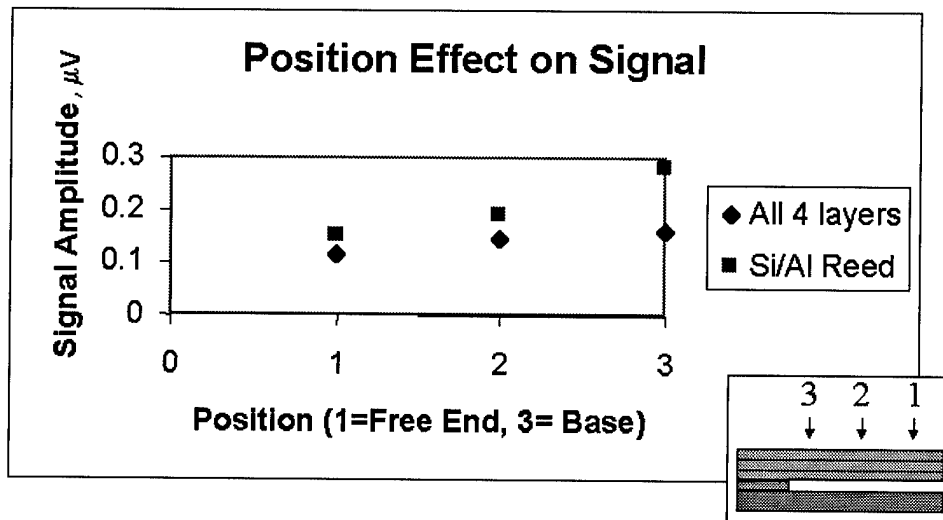


Figure 4.9: Deflection Affected by Position of Fiber

In addition to a decrease in signal as the beam moves further away from the base, notice the marked decrease in signal that comes with adding extra layers. The signal from reed two, the Si/Al reed, is what would contribute to background.

Reliability. The reed housing plays a large role in the repeatability of the measurements. There is a small stopper that sits beneath the free end of the cantilever reed. It was built into the reed's base as a way to keep down unwanted vibrations (read: noise) but now serves two purposes: Reliable results are obtained only after positioning the AFM tip over the area of contact between the cantilever reed and its stopper. This is because the reed itself is not stiff enough to hold up the AFM tip, and so will continue to bend if there is not a stable *stage-like* presence beneath it. By taking care to position the tip in the middle of the reed over the stopper, both problems can be solved.

It was also found important to position the reed in precisely the same place each time. Figure 4.20 shows three data runs with the same reed, a four-layer reed two centimeters in length. The *y axis* signal, measured by the lock-in amplifier, is the voltage component of the deflection signal at the phase indicated on the *x axis*. This phase is relative to the chopper frequency, and was taken from  $45^\circ$  to  $-110^\circ$ . The intent of this particular experiment was to characterize the phase lag associated with this reed, but complete measurements were not obtained. The first two, *Run 1* and *Run 2* were both positioned in the same place on the reed base. The third, *Run 3* hung about a millimeter over the *clamp* end of the base, effectively reducing the length of the reed. Notice the extreme difference in signal.

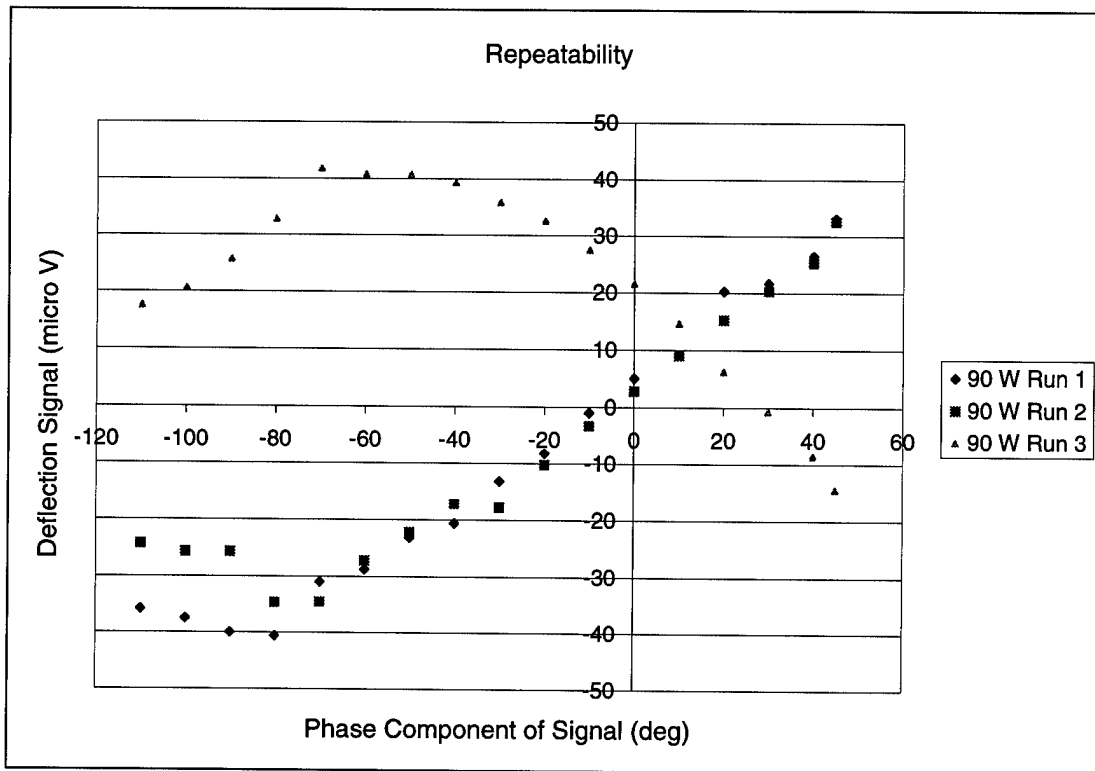


Figure 4.20: Component of Deflection Signal at Phase Differences Relative to Chopper Frequency. Shows the Importance of Positioning the Reed Carefully

### Comparison of Model and Experimental Results

The laboratory results appear to validate the model, except when important assumptions, such as aspect ratio of the beam, are violated. This points to a need for more development of the thermal problem. The reed sensor needs to be described as a plate, rather than a beam.

The model currently gives good qualitative analysis; correctly predicting temperature profile and deflection mode shapes, but is not yet adapted for quantitative predictions.

## 5. Conclusions

### Implications of Model Results

According to the mathematical model, it is best to operate with smaller reeds. Longer reeds are too sensitive to low frequency background noise, and shorter reeds produce too small a deflection signal. The incoming light should be modulated near the reed's mechanical frequency. This resonance must be found experimentally, because higher order resonance effects may be present, depending on the width of the reed.

The aluminum layer thickness should be increased. Unfortunately, current fabrication methods introduce significant curling of the reed if the aluminum layer is made any thicker. With improved construction techniques, the ratio of aluminum to silicon thickness can be brought to the optimum 0.325, rather than the current 0.0625.

### Implications of Experimental Results

Experimental data validates this model for use with long thin beams. This model is not as effective for shorter, wider beams are easier to produce and tend to better hold the deposited sample. For this case, a model based on plate mechanics rather than beam mechanics is necessary.

### Conclusion

This research was successful in applying mathematical models to the reed sensor. The model is applicable to long, thin reeds but does not accurately predict the behavior of short, squat reeds. In lab experiments show that more detailed modeling is necessary to describe these cases as higher order effects become too significant to continue modeling

the reed sensor as a beam. Modeling the reed sensor as a plate would allow for the development of models that would be valid over a broader range of reed parameters.

### **Suggestions for Further Research**

The silicon background signal swamps the deflection due to any sample present on the reed. As mentioned earlier, a decrease in deflection with increased absorber shows that the reed sensor itself is more sensitive to light absorbed in the silicon layer than it is to light absorbed in the sample. This problem must be eliminated, perhaps by use of a silicon filter. Also, it may be beneficial to consider alternative materials for this second layer. For example, diamond is relatively transparent to IR light and will not produce such a large background signal.

Transmission of light from the IR source to the reed is inefficient. The optical fiber introduces a 6 order of magnitude decrease in beam strength. A similar decrease results from use of a monochromator. Often, there is not enough power deposited to cause deflection. Ideas to increase the transmitted fraction of light include shorter fibers, higher quality fiber tools, and light pipes. The first two would bring obvious increases in transmitted fraction. The light pipe, made of highly reflective material, would deposit a greater fraction of beam energy to the reed, but may also spread the beam enough to balance any improvement. Also, the relatively large diameter of such a pipe may spread the IR beam so large that too little light hits the cross-sectional area of the reed.

## Bibliography

1. Baker, W. P. "The Thermal Problem." Private Communication. Winter 1998.
2. Barnes J. R., R. J. Stephenson, C. N. Woodburn, S. J. O'Shea, M. E. Welland, T. Rayment, J. K. Gimzewski, and C. H. Gerber. A Femtojoule Calorimeter Using Micromechanical Sensors. *Rev. Sci. Instrum.* Vol. 65 (12) Dec 94, p 3793.
3. Barnes, J.R., R. J. Stephenson, M. E. Welland, C. H. Gerber, J. K. Gimzewski. Photothermal Spectroscopy with Femtojoule Sensitivity using a Micromechanical Device. *Nature*, 372 (1994) p79-82.
4. Burggraf, L. W. and G. Li. Photothermal Interferometric NIR Detection Using Sol Gel Materials. *SPIE Vol. 3082* p. 30-37, 1997.
5. Hartnett T. M. and Gentilman R. L. Optical and Mechanical Properties of Highly Transparent Spinel and ALON Domes. Raytheon Research Division. RAY/RD/M-45099.
6. Lai J., T. Perazzo, Z. Shi, A. Majumdar. Optimization and performance of high-resolution micro-optomechanical thermal sensors. *Sensors and Actuators A Vol. 58* (1997) p. 113-119.
7. Li, G. "Power Through Fibre vs. Power of Source." Private Communication. Winter 1999.
8. Li, G. and L. W. Burggraf. Laser processing of sol-gel coatings for infrared applications. *SPIE Vol. 3136*. P 257-260, 1997.
9. Moulin A. M., R. J. Stephenson, M. E. Welland. Micromechanical thermal sensors: comparison of experimental results and simulations. *J. Vac. Sci. Technol. B* 15(3) p 590 (1997).
10. Ops Requirements Documents for a Joint Chemical/Biological Agent Water Monitor (JCBAWM)
11. Roy, D. W. and J. L. Hastert. Polycrystalline  $MgAl_2O_4$  (spinel) for use as Windows and Domes from 0.3 to 6.0 Micrometers. Coors Porcelain Company.

12. Salapka, M. V., H. S. Bergh, J. Lai, A. Majumdar, E. McFarland. Multimode Noise Analysis of Cantilevers for Scanning Probe Microscopes. *J. Apply Phys* 81 (1997) 2480-2487.
13. Sarid, Dror. *Scanning Force Microscopy With Application To Electric, Magnetic, And Atomic Forces*. Oxford University Press NY, 1991.
14. Walters, D. A., J. P. Cleveland, N. H. Thomson, P. K. Hansma, M. A. Wendman, G. Gurley, V. Elings. Short cantilevers for atomic force microscopy. *Rev Sci Instrum.* 67 (1996) 3583-3590.
15. Young, W. C. *Formulas for Stress and Strain*, McGraw-Hill, New York, 6<sup>th</sup> ed., pp. 93-232. 1989.

## Appendix A: Useful Data

The following table presents the values that were used in modeling the reed. The numbers in parentheses represent the possible range for that quantity.

*Table A.1: Table of Important Material Parameters [1,2]*

Quantity (symbol)	Units	Sol-Gel MgAl <sub>2</sub> O <sub>4</sub> )	Silicon (Si)	Aluminum (Al)
Thickness (t) (actual range)	μm	1 (.1 – 2)	8 (4 – 15)	.5 (*)
Density (ρ)	kg/m <sup>3</sup>	3580	2328	2702
Elastic Modulus (E)	10 <sup>11</sup> N/m <sup>2</sup>	2.77	1	.8
Thermal Conductivity (λ)	W/[m K]	14.6	150	237
Thermal Expansion (α)	10 <sup>-6</sup> 1/K	6.5	2.6	23.6
Heat Capacity (C <sub>p</sub> )	J/[kg K]	837.360	700	908
Thermal Diffusivity (D)	10 <sup>-6</sup> m <sup>2</sup> /s	4.87	92.05	96.6

The following table shows error introduced by approximating the derivative functions. The error grew quickly for very small reeds, but these reeds are outside of our parameter space.

*Table A.2: Error in Derivatives with Approximation*

Data Point	Baker's Values	Approximated Values	%Error
Root[.03,14,12]	0.00370472	0.00370485	.004
Root[.0225,8,25]	0.00279942	0.00280037	.03
Root[.01,1,500]	0.000811243	0.000823453	1.5
Root[.004,29,250]	0.00508951	0.00402847	26

### References:

1. Hartnett T. M. and Gentilman R. L. Optical and Mechanical Properties of Highly Transparent Spinel and ALON Domes. Raytheon Research Division. RAY/RD/M-45099.
2. Lai J., T. Perazzo, Z. Shi, A. Majundar. Optimization and Performance of High-Resolution Micro-Optomechanical Thermal Sensors. Sensors and Actuators A Vol 58 (1997) p. 113-119.



## Appendix B

### DERIVATION OF THE SOLUTION TO THE THERMAL PROBLEM

#### Fundamental Equations and Conditions.

Dr William Baker, of the Air Force Institute of Technology, has developed equations describing the heat transfer within the reed. They are based on the fundamental heat transfer equation, written for all three layers of the reed. The equation follows a sketch of the reed, as seen from the side.

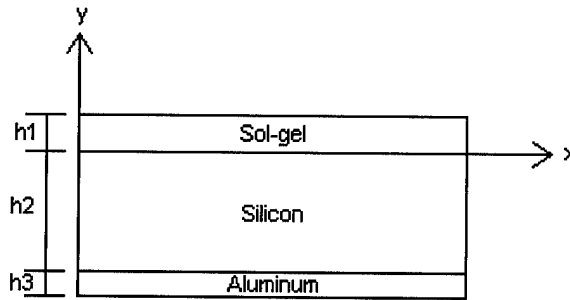


*Figure B.1: Schematic of the Reed*

$$\frac{\partial u^{(i)}(x, y, t)}{\partial t} = D_i \nabla^2 u^{(i)}(x, y, t) + \delta_{i1} k E_0(t)$$

$$\text{for } i=1,2,3; \quad t > 0; \quad 0 < x < L; \quad D_3 > D_2 \gg D_1;$$

$$i=1: \quad 0 < y < h_1; \quad i=2: \quad -h_2 < y < 0; \quad i=3: \quad -(h_2 + h_3) < y < -h_2;$$

$$D_i = \frac{k_i}{\rho_i c_{p,i}}$$

Note that the function  $E_0(t)$  only exists in the first layer, hence use of the Kronecker delta,  $\delta_{i,1}$ .

The heat transfer equation, written for all three layers must be solved to determine the temperature profile. Here the concern is the vertical and horizontal directions. The assumption is made that the temperature profile does not vary with width. Further, it is assumed that the temperature at the left-most boundary of the reed is held constant by the

clamp mechanism holding it in place. This temperature is also the initial temperature of the reed. The other three boundaries of the reed are assumed insulated. Convection and radiation remove a negligible amount of heat from the reed.

The solutions for the three layers are coupled together by the additional conditions of continuity of flux and temperature across the interfaces. These initial and boundary conditions are summarized as follows: For the three insulated edges, that is, top, bottom, and right side:

The top edge is insulated: 
$$\frac{\partial u^{(1)}}{\partial y}(x, h_1, t) = 0$$

The bottom edge is insulated: 
$$\frac{\partial u^{(3)}}{\partial y}(x, -(h_2 + h_3), t) = 0$$

The right edge is insulated (requiring an equation for each layer):

$$\frac{\partial u^{(1)}}{\partial x}(L, y, t) = \frac{\partial u^{(2)}}{\partial x}(L, y, t) = \frac{\partial u^{(3)}}{\partial x}(L, y, t) = 0$$

The left side, held at constant ambient temperature, is represented by:

$$u^{(1)}(0, y, t) = u^{(2)}(0, y, t) = u^{(3)}(0, y, t) = U_0$$

Continuity of Temperature across the interface requires:

$$u^{(1)}(x, 0, t) = u^{(2)}(x, 0, t) \quad \text{and} \quad u^{(2)}(x, -h_2, t) = u^{(3)}(x, -h_2, t)$$

Continuity of flux across the interface further requires:

$$D_1 \frac{\partial u^{(1)}}{\partial y}(x, 0, t) = D_2 \frac{\partial u^{(2)}}{\partial y}(x, 0, t) \quad \text{and} \quad D_2 \frac{\partial u^{(2)}}{\partial y}(x, -h_2, t) = D_3 \frac{\partial u^{(3)}}{\partial y}(x, -h_2, t)$$

Finally, the reed starts, in a straight position, at some initial temperature:

$$u^{(i)}(x, y, 0) = U_0$$

### Scaling the Problem.

For ease of solution, the equation is scaled: lengths are scaled to the overall length of the reed, and time is scaled to the period of the modulated IR light beam. The equation is re-written to reflect the real measure of interest: change in temperature. Assuming that the reed starts at some constant (ambient) temperature, the solution now must be found for the deviation of that temperature with time.

If we set  $x = L\xi$ ,  $y = L\eta$ ,  $t = T\tau$ ,  $h_i = \alpha_i$ , and define

$$u^{(i)}(x, y, t) = U_0 + w(\xi, \eta, \tau)$$

then the equations and boundary conditions become:

$$\begin{aligned} \frac{\partial w^{(i)}(\xi, \eta, \tau)}{\partial \tau} &= d_i \nabla^2 w^{(i)}(\xi, \eta, \tau) + \delta_{i1} F(\tau) & (B.1) \\ F(\tau) &= kTE_0(T\tau) \\ d_i &= \frac{TD_i}{L^2} \end{aligned}$$

Insulated edges:

$$\frac{\partial w^{(1)}}{\partial \eta}(\xi, \alpha_1, \tau) = \frac{\partial w^{(1)}}{\partial \xi}(1, \eta, \tau) = \frac{\partial w^{(2)}}{\partial \xi}(1, \eta, \tau) = \frac{\partial w^{(3)}}{\partial \xi}(1, \eta, \tau) = \frac{\partial w^{(3)}}{\partial \eta}(\xi, -(\alpha_2 + \alpha_3), \tau) = 0$$

Edge at constant ambient temperature:

$$w^{(1)}(0, \eta, \tau) = w^{(2)}(0, \eta, \tau) = w^{(3)}(0, \eta, \tau) = 0$$

Continuity of temperature across the interface gives:

$$w^{(1)}(\xi, 0, \tau) = w^{(2)}(\xi, 0, \tau) \quad \text{and} \quad w^{(2)}(\xi, -\alpha_2, \tau) = w^{(3)}(\xi, -\alpha_2, \tau)$$

Continuity of flux across the interface further requires:

$$d_1 \frac{\partial w^{(1)}}{\partial \eta}(\xi, 0, \tau) = d_2 \frac{\partial w^{(2)}}{\partial \eta}(\xi, 0, \tau) \quad \text{and} \quad d_2 \frac{\partial w^{(2)}}{\partial \eta}(\xi, -\alpha_2, \tau) = d_3 \frac{\partial w^{(3)}}{\partial \eta}(\xi, -\alpha_2, \tau)$$

Finally, the reed starts, in a straight position, at some initial temperature:

$$w^{(i)}(\xi, \eta, 0) = 0$$

### Assuming a Solution.

To satisfy the boundary conditions,

$$\frac{\partial w^{(i)}}{\partial \xi}(1, \eta, \tau) = 0 \quad \text{and} \quad w^{(i)}(0, \eta, \tau) = 0 \quad \text{for } i = 1, 2, 3.$$

the solution must have the form:

$$w^{(i)}(\xi, \eta, \tau) = \sum_{k=0}^{\infty} q^{(i)}(\eta, \tau) \text{Sin}(\lambda_k \xi) \quad (\text{B.2})$$

where

$$\lambda_k = (2k+1) \frac{\pi}{2} \quad \text{for } k = 0, 1, 2, \dots$$

This assumed solution is then inserted into the initial equation, resulting in

$$\frac{\partial w^{(i)}}{\partial \tau} - d_i \nabla^2 w^{(i)} = \sum_{k=0}^{\infty} \text{Sin}(\lambda_k \xi) \left\{ \frac{\partial q_k^{(i)}}{\partial \tau} + d_i \lambda_k^2 q_k^{(i)} - d_i \frac{\partial^2 q_k^{(i)}}{\partial \eta^2} \right\} = \delta_{il} F(\tau)$$

which becomes,

$$\frac{\partial q_k^{(i)}}{\partial \tau} + d_i \lambda_k^2 q_k^{(i)} - d_i \frac{\partial^2 q_k^{(i)}}{\partial \eta^2} = \frac{2\delta_{il} F(\tau)}{\lambda_k}$$

because of orthogonality of the sine function over the interval [0,1].

Similarly treated, the initial and boundary conditions become:

$$\frac{\partial q_k^{(1)}}{\partial \eta}(\alpha_1, \tau) = \frac{\partial q_k^{(3)}}{\partial \eta}(-(\alpha_2 + \alpha_3), \tau) = 0$$

$$q_k^{(1)}(0, \tau) = q_k^{(2)}(0, \tau)$$

$$q_k^{(2)}(-\alpha_2, \tau) = q_k^{(3)}(-\alpha_2, \tau)$$

$$d_1 \frac{\partial q_k^{(1)}}{\partial \eta}(0, \tau) = d_2 \frac{\partial q_k^{(2)}}{\partial \eta}(0, \tau)$$

$$d_2 \frac{\partial q_k^{(2)}}{\partial \eta}(-\alpha_2, \tau) = d_3 \frac{\partial q_k^{(3)}}{\partial \eta}(-\alpha_2, \tau)$$

### Laplace Transform

The series of  $q_k$ 's are Laplace transformed with respect to  $\tau$ . Defining,

$$Q_k^{(i)}(\eta, s) \equiv \mathcal{L}\left\{q_k^{(i)}(\eta, \tau)\right\} = \int_0^\infty e^{-s\tau} q_k^{(i)}(\eta, \tau) d\tau,$$

the differential equations become

$$sQ_k^{(i)} + d_i \lambda_k^2 Q_k^{(i)} - d_i \frac{\partial^2 Q_k^{(i)}}{\partial \eta^2} = \frac{2\delta_{i1} \hat{F}(\tau)}{\lambda_k}$$

Or

$$d_i \frac{\partial^2 Q_k^{(i)}}{\partial \eta^2} - (s + d_i \lambda_k^2) Q_k^{(i)} = -\frac{2\delta_{i1} \hat{F}(\tau)}{\lambda_k}$$

where

$$\hat{F}(\tau) = \int_0^\infty e^{-s\tau} F(\tau) d\tau.$$

A solution is easily obtained in the form:

$$Q_k^{(i)}(\eta, s) = A_i(s) e^{\frac{\mu_i}{\sqrt{d_i}} \eta} + B_i(s) e^{-\frac{\mu_i}{\sqrt{d_i}} \eta} + \frac{2\delta_{i1} \hat{F}(s)}{\lambda_k \mu_i^2}$$

where

$$\mu_i \equiv \sqrt{s + d_i \lambda_k^2}.$$

The unknown coefficients,  $A_i$  and  $B_i$ , are determined by applying the transformed boundary conditions,

- i.  $\frac{\partial Q_k^{(1)}}{\partial \eta}(\alpha_1, s) = \frac{\partial Q_k^{(3)}}{\partial \eta}(-(\alpha_2 + \alpha_3), s) = 0$
- ii.  $Q_k^{(1)}(0, s) = Q_k^{(2)}(0, s)$
- iii.  $d_1 \frac{\partial Q_k^{(1)}}{\partial \eta}(0, s) = d_2 \frac{\partial Q_k^{(2)}}{\partial \eta}(0, s)$
- iv.  $d_2 \frac{\partial Q_k^{(2)}}{\partial \eta}(-\alpha_2, s) = d_3 \frac{\partial Q_k^{(3)}}{\partial \eta}(-\alpha_2, s)$
- v.  $Q_k^{(2)}(-\alpha_2, s) = Q_k^{(3)}(-\alpha_2, s)$

Defining,

$$\gamma_i = \frac{\alpha_i}{\sqrt{d_i}}$$

and employing boundary condition  $i$  results in:

$$Q_k^{(1)}(\eta, s) = A_1(s) \text{Cosh}\left(\frac{\mu_1}{\sqrt{d_1}}(\eta - \alpha_1)\right) + \frac{2\hat{F}(s)}{\lambda_k \mu_1^2}$$

$$Q_k^{(2)}(\eta, s) = A_2(s) e^{\frac{\mu_2}{\sqrt{d_2}}\eta} + B_2(s) e^{-\frac{\mu_2}{\sqrt{d_2}}\eta}$$

$$Q_k^{(3)}(\eta, s) = A_3(s) \text{Cosh}\left(\frac{\mu_3}{\sqrt{d_3}}(\eta + \alpha_2 + \alpha_3)\right)$$

Applying boundary conditions  $ii$  and  $iii$ , along with some algebra, yield:

$$A_2(s) = \frac{H_k(s)}{2} + \frac{A_1(s)}{2} \left( \text{Cosh}(\mu_1 \gamma_1) - \frac{\mu_1}{\mu_2} \sqrt{\frac{d_1}{d_2}} \text{Sinh}(\mu_1 \gamma_1) \right)$$

$$B_2(s) = \frac{H_k(s)}{2} + \frac{A_1(s)}{2} \left( \text{Cosh}(\mu_1 \gamma_1) + \frac{\mu_1}{\mu_2} \sqrt{\frac{d_1}{d_2}} \text{Sinh}(\mu_1 \gamma_1) \right)$$

after defining

$$H_k(s) = \frac{2\hat{F}(s)}{\lambda_k \mu_1^2}$$

Doing the same for conditions  $iv$  and  $v$  results in:

$$A_2(s) = \frac{1}{2} e^{\mu_2 \gamma_2} A_3(s) \left( \text{Cosh}(\mu_3 \gamma_3) + \frac{\mu_3}{\mu_2} \sqrt{\frac{d_3}{d_2}} \text{Sinh}(\mu_3 \gamma_3) \right)$$

$$B_2(s) = \frac{1}{2} e^{-\mu_2 \gamma_2} A_3(s) \left( \text{Cosh}(\mu_3 \gamma_3) - \frac{\mu_3}{\mu_2} \sqrt{\frac{d_3}{d_2}} \text{Sinh}(\mu_3 \gamma_3) \right)$$

If

$$C_i = \text{Cosh}(\mu_i \gamma_i) \quad \text{and} \quad S_i = \frac{\mu_i}{\mu_2} \sqrt{\frac{d_i}{d_2}} \text{Sinh}(\mu_i \gamma_i),$$

then the previous results (combined and rearranged) become

$$A_2(s) = \frac{1}{2} H_k(s) + \frac{1}{2} A_1(s)(C_1 - S_1) = \frac{1}{2} e^{\mu_2 \gamma_2} A_3(s)(C_3 + S_3)$$

$$B_2(s) = \frac{1}{2} H_k(s) + \frac{1}{2} A_1(s)(C_1 + S_1) = \frac{1}{2} e^{-\mu_2 \gamma_2} A_3(s)(C_3 - S_3)$$

And can be manipulated to obtain:

$$\begin{bmatrix} C_1 & -(C_2 C_3 + S_2 S_3) \\ S_1 & (S_2 C_3 + C_2 S_3) \end{bmatrix} \begin{bmatrix} A_1(s) \\ A_3(s) \end{bmatrix} = \begin{bmatrix} -H_k(s) \\ 0 \end{bmatrix}$$

The coefficients  $A_1$  and  $A_3$  are easily solved as,

$$A_1(s) = -\frac{H_k}{D} (S_2 C_3 + C_2 S_3)$$

$$A_3(s) = \frac{H_k}{D} S_1$$

where

$$D = C_1(S_2 C_3 + C_2 S_3) + S_1(C_2 C_3 + S_2 S_3)$$

and substituted to solve for  $A_2$  and  $B_2$ :

$$A_2(s) = \frac{1}{2} e^{\mu_2 \gamma_2} \frac{H_k(s) S_1}{D} (C_3 + S_3)$$

$$B_2(s) = \frac{1}{2} e^{-\mu_2 \gamma_2} \frac{H_k(s) S_1}{D} (C_3 - S_3)$$

Note the distinction between  $s$ , transformed time, and  $S_i$ , a function written for convenience. Finally, the solution for each layer, in the transform domain is:

$$Q_k^{(1)}(\eta, s) = -\frac{H_k}{D} (S_2 C_3 + C_2 S_3) \text{Cosh}\left(\mu_1 \left(\frac{\eta}{\sqrt{d_1}} - \gamma_1\right)\right) + H_k$$

$$Q_k^{(3)}(\eta, s) = \frac{H_k(s) S_1}{D} \text{Cosh}\left(\frac{\mu_3}{\sqrt{d_3}} (\eta + \alpha_2 + \alpha_3)\right)$$

$$Q_k^{(2)}(\eta, s) = \frac{H_k(s) s_1}{D} \left( \frac{1}{2} C_3 \left( e^{\mu_2 \left(\gamma_2 + \frac{\eta}{\sqrt{d_2}}\right)} + e^{-\mu_2 \left(\gamma_2 + \frac{\eta}{\sqrt{d_2}}\right)} \right) \dots \right. \\ \left. + \frac{1}{2} S_3 \left( e^{\mu_2 \left(\gamma_2 + \frac{\eta}{\sqrt{d_2}}\right)} - e^{-\mu_2 \left(\gamma_2 + \frac{\eta}{\sqrt{d_2}}\right)} \right) \right) \\ = \frac{H_k(s) s_1}{D} \left( C_3 \text{Cosh} \mu_2 \left(\gamma_2 + \frac{\eta}{\sqrt{d_2}}\right) + S_3 \text{Sinh} \mu_2 \left(\gamma_2 + \frac{\eta}{\sqrt{d_2}}\right) \right).$$

Careful examination shows there are no branch points, and further, that if  $z$  is a root, then  $\bar{z}$  is as well.

### Inverting the Laplace Transform.

Directly inverting the Laplace transform, via calculus of residues, requires finding the roots of

$$\tilde{D}(s) = \mu_2(s) D(s) = \mu_2(s) (C_1 S_2 C_3 + C_1 C_2 S_3 + S_1 C_2 C_3 + S_1 S_2 S_3).$$



For the parameters of this problem,  $\tilde{D}(s)$  turns out to have a single root for each  $k$ ; lying along the negative real axis.

Defining,

$$\mu_i(z_k) = \sqrt{z_k + d_i \lambda_k^2} = \begin{cases} \omega_k^{(i)} & \text{if } d_i \lambda_k^2 - \sigma_k > 0 \\ i\omega_k^{(i)} & \text{if } d_i \lambda_k^2 - \sigma_k < 0 \end{cases}$$

$$z_k = -\sigma_k$$

The inverse Laplace transform of a representative piece of the solutions becomes

$$\begin{aligned} & L^{-1} \left\{ \frac{A(s)}{D(s)} \text{Cosh}(\mu_i(s)\beta(\eta)) \right\} \\ &= \frac{1}{2\pi i} \int_{c-i\infty}^{c+i\infty} e^{st} \frac{A(s)}{D(s)} \text{Cosh}(\mu_i(s)\beta(\eta)) ds \\ &= \text{Re } s \left\{ z_k ; e^{st} \frac{A(s)}{D(s)} \text{Cosh}(\mu_i(s)\beta(\eta)) \right\} \\ &= e^{-\sigma_k t} \frac{A(-\sigma_k)\mu_2(-\sigma_k)}{\tilde{D}'(-\sigma_k)} \begin{cases} \text{Cosh}(\omega_k^{(i)}(s)\beta(\eta)) & \text{if } d_i \lambda_k^2 - \sigma_k > 0 \\ \text{Cos}(\omega_k^{(i)}(s)\beta(\eta)) & \text{if } d_i \lambda_k^2 - \sigma_k < 0 \end{cases} \end{aligned}$$

where

$$\tilde{D}'(s) = \frac{d}{ds}(\tilde{D}(s)) = \frac{d}{ds}(\mu_2(s)D(s)).$$

Within the parameter space of this problem, these roots and functions evaluate to

$$\begin{aligned} z_k &= -\sigma_k \\ \mu_1(z_k) &= i\omega_k^{(1)} \\ \mu_2(z_k) &= \omega_k^{(2)} \\ \mu_3(z_k) &= \omega_k^{(3)} \\ \tilde{D}_k &= \tilde{D}'(-\sigma_k) \end{aligned}$$

This last term reflects the derivative function being real at each root.

So that the convolution theorem may later be used, the  $Q_k$ 's are written as

$$Q_k^{(i)}(\eta, s) = \frac{2}{\lambda_k} \hat{F}(s) \cdot G_k^{(i)}(\eta, s)$$

$$G_k^{(1)}(\eta, s) = -\frac{H_k}{D} (S_2 C_3 + C_2 S_3) \text{Cosh}(\mu_1 (\frac{\eta}{\sqrt{d_1}} - \gamma_1)) + H_k$$

$$G_k^{(2)}(\eta, s) = \frac{s_1}{\mu_1^2 D} \left( C_3 \text{Cosh} \mu_2 (\gamma_2 + \frac{\eta}{\sqrt{d_2}}) + S_3 \text{Sinh} \mu_2 (\gamma_2 + \frac{\eta}{\sqrt{d_2}}) \right)$$

$$G_k^{(3)}(\eta, s) = \frac{S_1}{\mu_1^2 D} \text{Cosh}(\frac{\mu_3}{\sqrt{d_3}} (\eta + \alpha_2 + \alpha_3))$$

Now, after defining

$$g_k^{(i)}(\eta, s) = L^{-1} \{ G_k^{(i)}(\eta, s) \}$$

$$g_k^{(1)}(\eta, s) = -e^{-\sigma_k t} \frac{1}{(\omega_k^{(1)})^2 \tilde{D}_k} \text{Cos}(\frac{\omega_k^{(1)}}{\sqrt{d_1}} (\eta + \alpha_1)) *$$

$$\left\{ \omega_k^{(2)} \text{Sinh}(\omega_k^{(2)} \gamma_2) \text{Cosh}(\omega_k^{(3)} \gamma_3) + \sqrt{\frac{d_1}{d_2}} \omega_k^{(3)} \text{Cosh}(\omega_k^{(2)} \gamma_2) \text{Sinh}(\omega_k^{(3)} \gamma_3) \right\}$$

$$g_k^{(2)}(\eta, s) = e^{-\sigma_k t} \sqrt{\frac{d_1}{d_2}} \frac{\text{Sinh}(\omega_k^{(1)} \gamma_1)}{\omega_k^{(1)} \tilde{D}_k} *$$

$$\left\{ \text{Cosh}(\omega_k^{(3)} \gamma_3) \text{Cosh}(\frac{\omega_k^{(2)}}{\sqrt{d_2}} (\eta + \gamma_{23})) + \sqrt{\frac{d_3}{d_2}} \frac{\omega_k^{(3)}}{\omega_k^{(2)}} \text{Sinh}(\omega_k^{(3)} \gamma_3) \text{Sinh}(\frac{\omega_k^{(2)}}{\sqrt{d_2}} (\eta + \gamma_{23})) \right\}$$

$$g_k^{(3)}(\eta, s) = e^{-\sigma_k t} \sqrt{\frac{d_1}{d_2}} \frac{\text{Sinh}(\omega_k^{(1)} \gamma_1)}{\omega_k^{(1)} \tilde{D}_k} \text{Cosh}(\frac{\omega_k^{(3)}}{\sqrt{d_3}} (\eta + \alpha_2 + \alpha_3)),$$

the  $q_k^{(i)}(\eta, t)$  are determined by convoluting  $g_k^{(i)}(\eta, t)$  with  $\frac{2}{\lambda_k} F(t)$ . To capture

the time dependence of the  $g_k^{(i)}(\eta, t)$ ,  $I_k(t)$  is defined as

$$I_k(t) = \int_0^t e^{-\sigma_k(t-\tau)} F(\tau) d\tau.$$

### Incoming Energy.

It is time to consider the absorbed energy,  $F(t)$ . This energy, originating from light modulated by a chopper, takes the form of:

$$F(\tau) = kE_0(\tau) = k \begin{cases} I_0 & 0 \leq \frac{\tau}{T} \leq t_0 \\ 0 & t_0 < \frac{\tau}{T} < 1 \end{cases} \quad (\text{B.3})$$

Here  $t_0$  represents the fraction of a period,  $T$ , that the beam is turned on. Only a portion,  $k$ , of the incident energy,  $E_0$ , is deposited in the sol gel layer.

Up to, and including, one period, the solution for the time dependant part of the problem looks like

$$I_k(t) = \frac{kI_0}{\sigma_k} \begin{cases} 1 - e^{-\sigma_k t} & 0 \leq \tau \leq t_0 \\ (e^{\sigma_k t_0} - 1)e^{-\sigma_k t} & t_0 < \tau < T \end{cases}$$

Of course, the following form is needed for  $t$  over many (more than 1) periods:

$$I_k(t) = \frac{kI_0}{\sigma_k} e^{-\sigma_k t} \left[ \frac{(e^{\sigma_k t_0} - 1)}{(e^{\sigma_k} - 1)} (e^{\sigma_k p} - 1) - e^{\sigma_k p} \right] + \frac{kI_0}{\sigma_k} \begin{cases} 1 & 0 \leq \tau \leq t_0 \\ e^{-\sigma_k((t-p)-t_0)} & t_0 < \tau < \end{cases} \quad (\text{B.4})$$

where  $p$  is the number of periods completed. The parameters,  $k$ , and  $I_0$  can be determined experimentally as described in Chapter 3.

### Min and Max.

Casual analysis of the time dependant portion of the solution indicates that the greatest change in temperature will occur when  $t_0$ , the portion of the period that the beam is turned on, is equal to 0.5. The chopper used, by design, is set up such that  $t_0 = 0.5$ .

### Summary of Solution.

The final solution for each layer is comprised of a series of solutions. Each series term,  $k$ , includes a dynamic description of the energy deposition,

$$I_k(t) = \frac{kI_0}{\sigma_k} e^{-\sigma_k t} \left[ \frac{(e^{\sigma_k t_0} - 1)}{(e^{\sigma_k} - 1)} (e^{\sigma_k p} - 1) - e^{\sigma_k p} \right] + \frac{kI_0}{\sigma_k} \begin{cases} 1 & 0 \leq \frac{\tau}{T} \leq t_0 \\ e^{-\sigma_k((t-p)-t_0)} & t_0 < \frac{\tau}{T} < 1 \end{cases},$$

modulated in the horizontal ( $x$ ) direction by  $\phi_k(\xi) = \frac{1}{\lambda_k} \text{Sin}(\lambda_k \xi)$ .

The energy attenuates as it passes through the depth ( $y$ ) of the reed. This behavior is shown, for each layer  $i$ , by  $\psi_k^i(\eta)$ :

$$\psi_k^1(\eta) = \text{Cos}\left(\frac{\omega_k^{(1)}}{\sqrt{d_1}}(\eta + \alpha_1)\right) \quad (\text{B.5})$$

$$\psi_k^2(\eta) = A_k \text{Cosh}\left(\frac{\omega_k^{(2)}}{\sqrt{d_2}}(\eta + \alpha_2)\right) + B_k \text{Sinh}\left(\frac{\omega_k^{(2)}}{\sqrt{d_2}}(\eta + \alpha_2)\right)$$

where

$$A_k = \text{Cosh}(\omega_k^{(3)} \gamma_3)$$

$$B_k = \sqrt{\frac{d_3}{d_2}} \frac{\omega_k^{(3)}}{\omega_k^{(2)}} \text{Sinh}(\omega_k^{(3)} \gamma_3)$$

$$\psi_k^3(\eta) = \text{Cosh}\left(\frac{\omega_k^{(3)}}{\sqrt{d_3}}(\eta + \alpha_2 + \alpha_3)\right).$$

Finally, the solution to the thermal behavior for a three-layer reed can be written:

$$w(\xi, \eta, \tau) = \sum_{k=0}^{\infty} C_k^{(i)} I_k(\tau) \phi_k(\xi) \psi_k^{(i)}(\eta) \quad (\text{B.7})$$

where

$$C_k^{(1)} = \frac{-2}{(\omega_k^{(1)})^2 \tilde{D}_k} \left\{ \omega_k^{(2)} \text{Sinh}(\omega_k^{(2)} \gamma_2) \text{Cosh}(\omega_k^{(3)} \gamma_3) + \sqrt{\frac{d_1}{d_2}} \omega_k^{(3)} \text{Cosh}(\omega_k^{(2)} \gamma_2) \text{Sinh}(\omega_k^{(3)} \gamma_3) \right\}$$

and

$$C_k^{(2)} = C_k^{(3)} = \sqrt{\frac{d_1}{d_2}} \frac{\text{Sinh}(\omega_k^{(1)} \gamma_1)}{\omega_k^{(1)} \tilde{D}_k}.$$

## **Appendix C: Mathematical Model**

### **Thermal Solution Approximation of the Code Application to the Reed Sensor Phase Exploration Resonance and Optimum Thickness Exploration**

#### **■ Reed Parameters**

First, the important thermal parameters are defined: thickness of each layer, length, frequency and period of the chopper, thermal diffusivity

```

(* height of layers *)
h1 = 1 * 10 ^ (-6);
h2 = 8 * 10 ^ (-6);
h3 = .5 * 10 ^ (-6);

(*length of reed,
  assuming Aspect (L/w) ratio of at least 10 *)
L = .0225;

(*Modulation frequency, in Hertz*)
ChopperSpeed = 8;

(*Timescale, in seconds *)
T = N[1 / ChopperSpeed];

(* alphas, scaled height, unitless *)
alpha1 = h1 / L;
alpha2 = h2 / L;
alpha3 = h3 / L;

(* thermal diffusivities, in m^2/s *)
D1 = 4.87 * 10 ^ (-6);
D2 = 92.05 * 10 ^ (-6);
D3 = 96.6 * 10 ^ (-6);

(* scaled diffusion, unitless *)
dd1 = (T * D1) / L ^ 2;
dd2 = (T * D2) / L ^ 2;
dd3 = (T * D3) / L ^ 2;

(* "diffusion speed" scale, unitless *)
gam1 =  $\frac{\alpha1}{\sqrt{dd1}}$ ;
gam2 =  $\frac{\alpha2}{\sqrt{dd2}}$ ;
gam3 =  $\frac{\alpha3}{\sqrt{dd3}}$ ;

```

### ■ The Root Solving Block

Here the relationships are defined and the root terms are calculated. The derivative terms are also calculated.

$$\lambda_k = (2k+1) * \frac{\pi}{2} \quad \text{and} \quad \text{"lams"} = \lambda_k^2$$

```

lams[k_] := ((2 * k + 1) * Pi / 2)^2;
mu_i = Sqrt[s + d_i (lambda_k)^2]

mu1[s_, k_] := Sqrt[s + dd1 * lams[k]];
mu2[s_, k_] := Sqrt[s + dd2 * lams[k]];
mu3[s_, k_] := Sqrt[s + dd3 * lams[k]];
c_i = Cosh(mu_i gamma_i)

cc1[s_, k_] := Cosh[mu1[s, k] * gam1];
cc2[s_, k_] := Cosh[mu2[s, k] * gam2];
cc3[s_, k_] := Cosh[mu3[s, k] * gam3];
s_i = Sqrt[d_i / d_2] * mu_i / mu_2 * Sinh(mu_i gamma_i)

ss1[s_, k_] :=
  Sqrt[dd1 / dd2 * mu1[s, k] / mu2[s, k] * Sinh[mu1[s, k] * gam1];
ss2[s_, k_] := Sinh[mu2[s, k] * gam2]; (* mu2 / mu2 taken out *)
ss3[s_, k_] :=
  Sqrt[dd3 / dd2 * mu3[s, k] / mu2[s, k] * Sinh[mu3[s, k] * gam3];

```

The function we want roots to:  $\tilde{D} = \mu_2(s)D(s) = c_1 c_3 s_2 \mu_2 + c_1 c_2 s_3 \mu_2 + c_2 c_3 s_1 \mu_2 + s_1 s_3 s_2 \mu_2$

```

Dd[s_, k_] := cc1[s, k] * cc3[s, k] * ss2[s, k] * mu2[s, k]
  + cc1[s, k] * cc2[s, k] * ss3[s, k] * mu2[s, k]
  + cc2[s, k] * cc3[s, k] * ss1[s, k] * mu2[s, k]
  + ss1[s, k] * ss2[s, k] * ss3[s, k] * mu2[s, k]

```

Here the root finding block will find the roots, assign them to the values  $\sigma_k$ , and also assign the corresponding values to

$\partial \frac{D}{\partial s}(z_k)$ ,  $\mu_1(z_k)$ ,  $\mu_2(z_k)$ , and  $\mu_3(z_k)$ . *Mathematica* uses Newton's method to search for the root.

Set k max before running it. Also, note that the table which lists all of these values is not printed out, you can easily have it print by removing the comment markers "(\*)" and "(\*)" which bracket it.



```

info = {{ "k", "λk", "-d2λk2", "zk",
          "∂ D̄ / ∂ s (zk", "μ1(zk)", "μ2(zk)", "μ3(zk)" }};
kmax = 100;
Do[ak = √lams[k]; bk = -dd2 * lams[k];
   ck = z /. FindRoot[Dd[z, k] == 0, {z, .99 * bk}];
   sig[k] = Abs[ck];
   dk = (D[Dd[s, k], s] /. s -> ck);
   derv[k] = dk;
   ek = mu1[ck, k];
   w1[k] = Im[ek];
   fk = mu2[ck, k];
   w2[k] = Re[fk];
   gk = mu3[ck, k];
   w3[k] = Re[gk];
   AppendTo[
     info, {k, ak, bk, ck, dk, ek, fk, gk}];, {k, 0, kmax}]
(*NumberForm[TableForm[info, TableSpacing->1], 7] *)

```

Now the series solution:

#### ■ The Constant Functions "ck"

```

ck1[k_] :=
ck1[k] = 
$$\frac{2}{(w1[k])^2 * derv[k]} * \left( w2[k] * Sinh[w2[k] * gam2] * \right.$$


$$Cosh[w3[k] * gam3] + \sqrt{\frac{dd3}{dd2}} w3[k] * \left.$$


$$Cosh[w2[k] * gam2] * Sinh[w3[k] * gam3] \right);$$

ck2[k_] := ck2[k] = 
$$2 * \sqrt{\frac{dd1}{dd2}} * \frac{Sin[w1[k] * gam1]}{w1[k] * derv[k]};$$

ck3[k_] := ck3[k] = 
$$2 * \sqrt{\frac{dd1}{dd2}} * \frac{Sin[w1[k] * gam1]}{w1[k] * derv[k]};$$


```

#### ■ The Time-Energy Behavior "I"

This function describes the deposition of energy into the layers. The expected difference between the layers comes from the modulation of I by the other terms.

```

kk = 1;
(*this k represents an absorption of the top layer*)
Io = 1 * 10^-6; (* this represents
the initial intensity of the incoming beam,
The fibre itself effects a 10^-6 reduction *)
to = .5 (* fraction of period that signal is on,
this cannot change and is due to chopper setup *);
p[t_] := p[t] = IntegerPart[t]

```

$$\begin{aligned}
Ii[t_, k_] := Ii[t, k] = & \frac{kk * Io}{sig[k]} * E^{-sig[k]*t} * \\
& \left( \frac{(E^{sig[k]*to} - 1)}{(E^{sig[k]} - 1)} * (E^{sig[k]*p[t]} - 1) - E^{sig[k]*p[t]} \right) + \\
& \frac{kk * Io}{sig[k]} * If[t - p[t] <= to, 1, E^{-sig[k]*((t-p[t])-to)}];
\end{aligned}$$

#### ■ The X Behavior, $\phi$ , or "Thi"

This series behavior was assumed into the solution, and accounts for the thermal sink on one end and an insulated condition on the other end.

$$\phi_k(\zeta) = \frac{1}{\lambda_k} \text{Sine}(\lambda_k \zeta)$$

$$\text{lam}[k_] := \text{lam}[k] = \left( (2 * k + 1) * \frac{\text{Pi}}{2} \right);$$

$$\text{thi}[\xi_, k_] := \text{thi}[\xi, k] = \frac{1}{\text{lam}[k]} * \text{Sin}[\text{lam}[k] * \xi];$$

#### ■ The Y Behavior, $\psi$ , or "Psi"

Relation for the thermal behavior in the vertical direction.

$$\begin{aligned}
Aa[k_] &:= Aa[k] = \text{Cosh}[w3[k] * gam3]; \\
Bb[k_] &:= Bb[k] = \sqrt{\frac{dd3}{dd2}} * \frac{w3[k]}{w2[k]} * \text{Sinh}[w3[k] * gam3]; \\
Psi1[\eta_, k_] &:= Psi1[\eta, k] = \text{Cos}\left[w1[k] * \left(\frac{\eta}{\sqrt{dd1}} - gam1\right)\right]; \\
Psi2[\eta_, k_] &:= \\
Psi2[\eta, k] &= Aa[k] * \text{Cosh}\left[w2[k] * \left(\frac{\eta}{\sqrt{dd2}} + gam2\right)\right] + \\
&Bb[k] * \text{Sinh}\left[w2[k] * \left(\frac{\eta}{\sqrt{dd2}} + gam2\right)\right]; \\
Psi3[\eta_, k_] &:= \\
Psi3[\eta, k] &= \text{Cosh}\left[\frac{w3[k]}{\sqrt{dd3}} * (\eta + alpha2 + alpha3)\right];
\end{aligned}$$

■ The Final Equation: Putting it all together

$$\begin{aligned}
Ww1[\xi_, \eta_, \tau_] &:= Ww1[\xi, \eta, \tau] = \\
&\sum_{k=0}^{kmax} ck1[k] * Ii[\tau, k] * thi[\xi, k] * Psi1[\eta, k]; \\
Ww2[\xi_, \eta_, \tau_] &:= Ww2[\xi, \eta, \tau] = \\
&\sum_{k=0}^{kmax} ck2[k] * Ii[\tau, k] * thi[\xi, k] * Psi2[\eta, k]; \\
Ww3[\xi_, \eta_, \tau_] &:= Ww3[\xi, \eta, \tau] = \\
&\sum_{k=0}^{kmax} ck3[k] * Ii[\tau, k] * thi[\xi, k] * Psi3[\eta, k];
\end{aligned}$$

■ Sample Calculations:

Here, I present some sample calculations using series terms up to and including 100. The data points seem very small, this is because of the reduction of light intensity as it travels through the beam. Dr Li calculated this to be a  $10^{-6}$  drop:

These next few blocks are groups of six data points. They take place at various points on the x axis, as marked- at one half of the first period (so the beam is just shutting off) and are located at the boundaries.

The first point is on the top of the sol gel layer.

The next two printouts are the boundary between the silicon and sol gel layers (both outputs should match, but they don't). The second set of points represents the boundary between the silicon and aluminum layers and again should match.

Finally, the last data point printed in each set is a point on the very bottom of the aluminum layer.

At the end of the reed, that is  $x=L$

```
Ww1[1, alpha1, 2000.5]
Ww1[1, 0, 2000.5]
Ww2[1, 0, 2000.5]
Ww2[1, -alpha2, 2000.5]
Ww3[1, -alpha2, 2000.5]
Ww3[1, -(alpha2 + alpha3), 2000.5]
```

$1.2955 \times 10^{-6} + 0. I$

$1.2955 \times 10^{-6} + 0. I$

$1.2955 \times 10^{-6} + 0. I$

$1.2955 \times 10^{-6} + 0. I$

$1.2955 \times 10^{-6} + 0. I$

$1.2955 \times 10^{-6} + 0. I$

```
Ww1[1, alpha1, 2000]
Ww1[1, 0, 2000]
Ww2[1, 0, 2000]
Ww2[1, -alpha2, 2000]
Ww3[1, -alpha2, 2000]
Ww3[1, -(alpha2 + alpha3), 2000]
```

$1.26919 \times 10^{-6} + 0. I$

$1.26919 \times 10^{-6} + 0. I$

$1.26919 \times 10^{-6} + 0. I$

$1.26919 \times 10^{-6} + 0. I$

$1.26919 \times 10^{-6} + 0. I$

$1.26919 \times 10^{-6} + 0. I$

x = .01L, that is, near the beginning of the reed

**Ww1[.01, alpha1, 2000.5]**  
**Ww1[.01, 0, 2000.5]**  
**Ww2[.01, 0, 2000.5]**  
**Ww2[.01, -alpha2, 2000.5]**  
**Ww3[.01, -alpha2, 2000.5]**  
**Ww3[.01, -(alpha2 + alpha3), 2000.5]**

$$2.76281 \times 10^{-8} + 0. \text{ I}$$

$$2.7628 \times 10^{-8} + 0. \text{ I}$$

$$2.7628 \times 10^{-8} + 0. \text{ I}$$

$$2.76279 \times 10^{-8} + 0. \text{ I}$$

$$2.76279 \times 10^{-8} + 0. \text{ I}$$

$$2.76279 \times 10^{-8} + 0. \text{ I}$$

x = .01L, again, this time at the beginning of a period, instead of half way through.  
Notice that the layers are all the same.

**Ww1[.01, alpha1, 2000]**  
**Ww1[.01, 0, 2000]**  
**Ww2[.01, 0, 2000]**  
**Ww2[.01, -alpha2, 2000]**  
**Ww3[.01, -alpha2, 2000]**  
**Ww3[.01, -(alpha2 + alpha3), 2000]**

$$2.34155 \times 10^{-8} + 0. \text{ I}$$

$$2.34155 \times 10^{-8} + 0. \text{ I}$$

$$2.34155 \times 10^{-8} + 0. \text{ I}$$

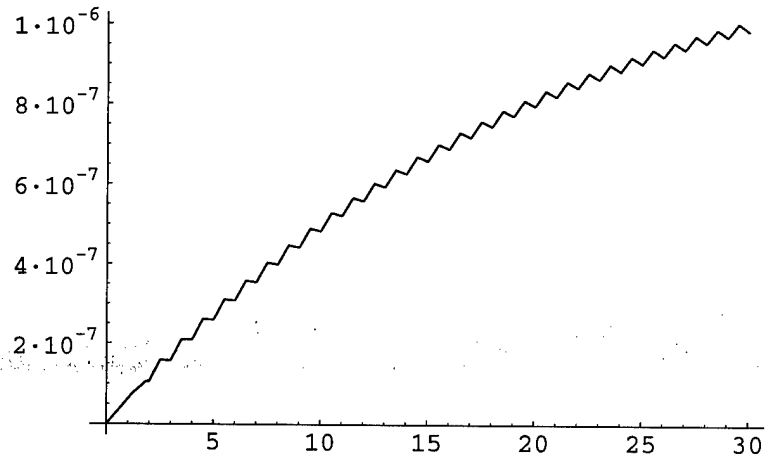
$$2.34155 \times 10^{-8} + 0. \text{ I}$$

$$2.34155 \times 10^{-8} + 0. \text{ I}$$

$$2.34155 \times 10^{-8} + 0. \text{ I}$$

The following graph is temperature vs scaled time, for the top layer:

```
Plot[Abs[Ww1[1, 0, t]], {t, 0, 30}];
```

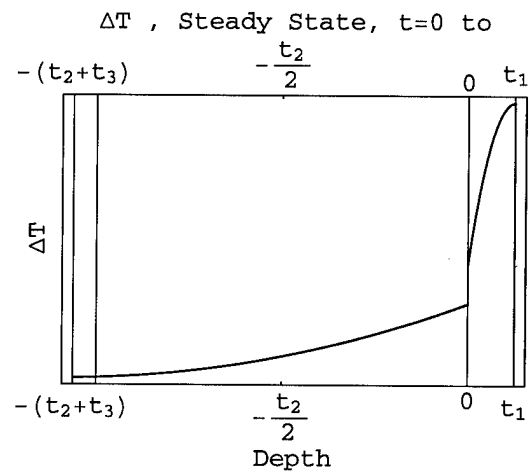


The Below Graph is Temperature Fluctuation vs Depth, combined for all three layers. The first plot is at the beginning of the 2001th period, steady state. The second is halfway through the 2001th period. The gridlines represent the edges of each layer. Note that they both have the same shape. At the beginning of the period has magnitude about  $1.269 \cdot 10^{-6}$  Kelvin, and half a period later, the temperature in the layers has jumped up to the  $1.295 \cdot 10^{-6}$  Kelvin range.

```

a = Plot[Abs[Ww1[1, y, 2000.5]], {y, 0, alpha1}];
b = Plot[Abs[Ww2[1, y, 2000.5]], {y, -alpha2, 0}];
c = Plot[Abs[Ww3[1, y, 2000.5]],
  {y, -(alpha2 + alpha3), -alpha2}];
w = Show[a, b, c,
  Frame -> True, FrameLabel -> {"Depth", " ΔT "},
  FrameTicks -> {{alpha1, "t1"}, 0, { $-\frac{\text{alpha2}}$ , " $-\frac{t_2}{2}$ "},
    {-(alpha2 + alpha3), " $-(t_2+t_3)$ "},
    {.0276281, .0276279}}, GridLines ->
  {{alpha1, 0, -alpha2, -(alpha2 + alpha3)}, None},
  PlotLabel -> "ΔT , Steady State, t=0 to"];

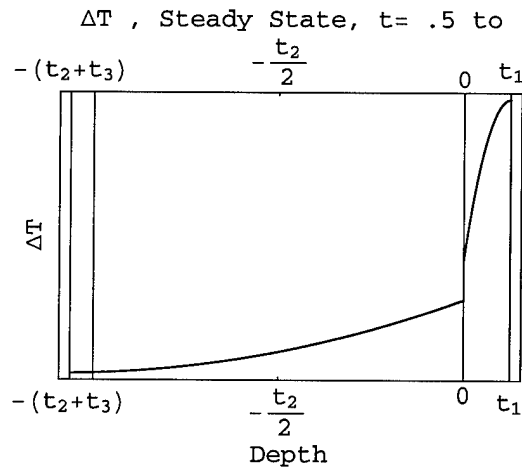
```



```

a = Plot[Abs[Ww1[1, y, 2000]], {y, 0, alpha1}];
b = Plot[Abs[Ww2[1, y, 2000]], {y, -alpha2, 0}];
c = Plot[Abs[Ww3[1, y, 2000]],
  {y, -(alpha2 + alpha3), -alpha2}];
w = Show[a, b, c,
  Frame -> True, FrameLabel -> {"Depth", " ΔT "},
  FrameTicks -> {{alpha1, "t1"}, 0, {-alpha2/2, "- t2/2"},
    {-(alpha2 + alpha3), "-(t2+t3)"}},
  GridLines ->
    {(alpha1, 0, -alpha2, -(alpha2 + alpha3)), None},
  PlotLabel -> "ΔT , Steady State, t= .5 to"];

```



### Approximation

Here I make some approximations to Dr Baker's thermal code. I ran the thermal code for varying lengths and frequencies and fit the data as shown below:

#### ■ Frequency

#### ■ Roots as a function of w, for k=0

Here I create a List of the Frequencies and their Root Values, obtained in another file using Dr Baker's Thermal Code These are all for the first root, that is, k=0:

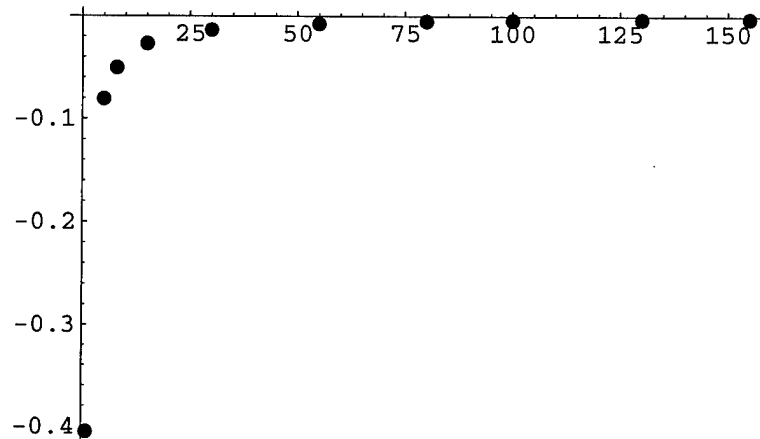


```

root0 = {{1, -.4050890}, {5, -.08101618},
        {8, -0.05063511}, {15, -0.02700539},
        {30, -0.0135027}, {55, -0.0073651078},
        {80, -0.005063511130}, {100, -0.004050809},
        {130, -0.003116007}, {155, -0.002613425}};

a = ListPlot[root0, PlotStyle -> PointSize[.02]];

```



Note that the magnitude of the roots approach zero as the frequencies approach infinity

```

Fit[root0, {1/w, 1, w}, w]

```

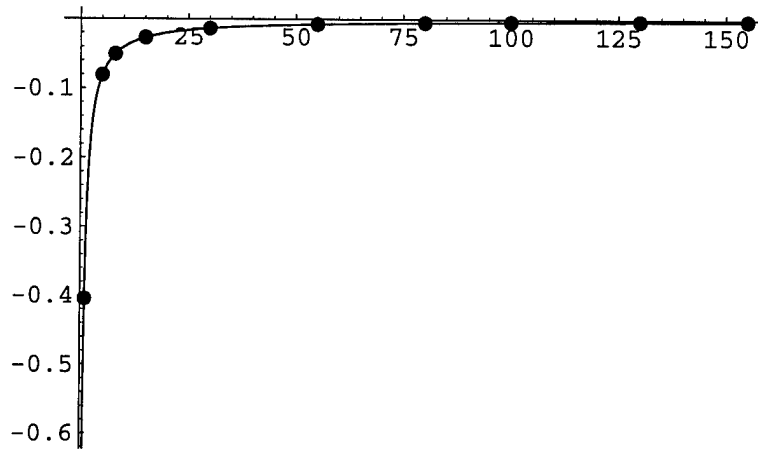
$$9.34387 \times 10^{-7} - \frac{0.40509}{w} - 7.48072 \times 10^{-9} w$$

Testing showed only the middle term to be significant (small coefficients are significant in other fits)

```

a = ListPlot[root0, PlotStyle -> PointSize[.02]];
b = Plot[.405089 / -x, {x, 0, 155}];
Show[a, b];

```



- Derivative as a function of  $w$  for  $k = 0$  (pretty much constant all the way through  $k = 25$ )

Here I create a List of the Frequencies and their Derivative Values,  $\Pi$  for  $k=0$ :

```

deriv0 = {{1, 0.0009901744}, {5, 0.002214097},
          {8, 0.002800636}, {15, 0.003834929},
          {30, 0.005423409}, {55, 0.00734333},
          {80, 0.008856389}, {100, 0.009901744},
          {130, 0.01128973}, {155, 0.01232757}};

```

```

Fit[deriv0, {1,  $\sqrt{w}$ , w}, w]

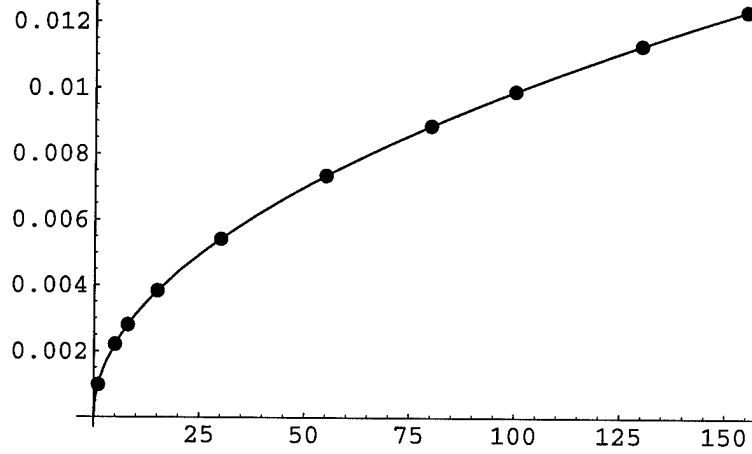
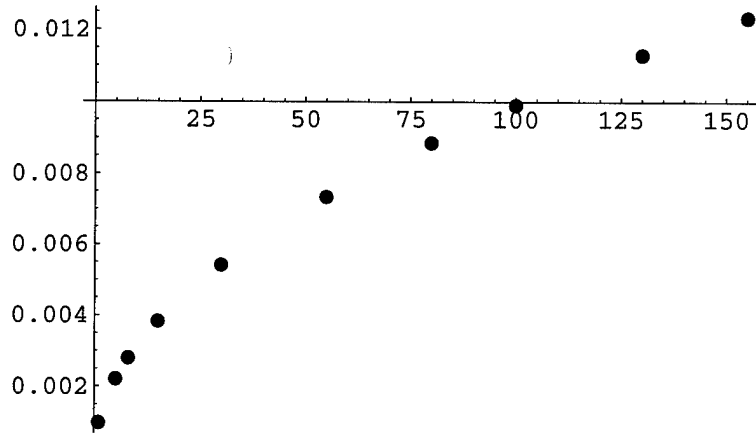
```

$$-4.76512 \times 10^{-10} + 0.000990175 \sqrt{w} - 6.09522 \times 10^{-12} w$$

```

a = ListPlot[deriv0, PlotStyle -> PointSize[.02]];
b = Plot[0.0009901744  $\sqrt{x}$ , {x, 0, 155}];
Show[a, b];

```



■ Length (all for k=0)

■ Roots

```

root0 = {{.01, -2.050722}, {.005, -8.202887},
         {.0075, -3.645728}, {.0125, -1.312462},
         {.015, -0.911432}, {.0175, -0.6696235},
         {.02, -0.5126805}, {.0225, -0.4050809},
         {.025, -0.3281155}};

```

```

Fit[root0, {1/L^2}, L]

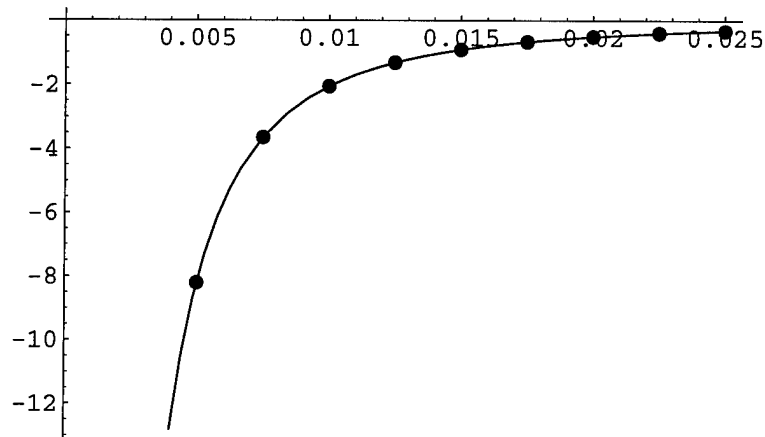
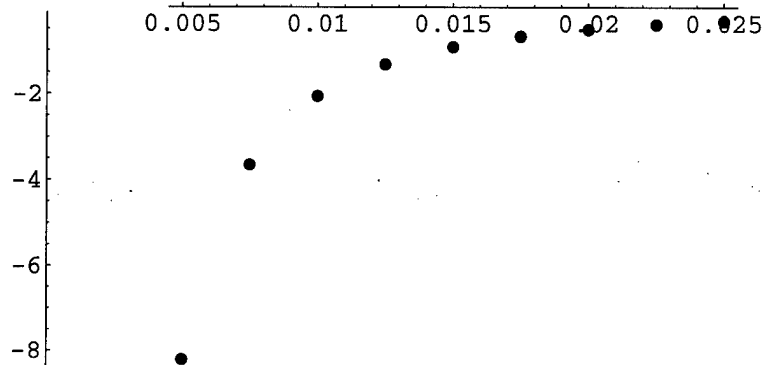
```

$$-\frac{0.000205072}{L^2}$$

```

a = ListPlot[root0,
  PlotStyle -> PointSize[.02], AxesOrigin -> {0, 0}];
b = Plot[.0001
  (x^2) * (-2.050722),
  {x, .004, .025}, AxesOrigin -> {0, 0}];
Show[a, b, AxesOrigin -> {0, 0}];

```



Here the fit is  $Z(L) = .0001 \frac{Z_0}{L^2}$  where  $Z_0 = Z(L=.01)$ , calculated by the root solver used in the thrmal code.

- Derivatives- doesn't vary much with L, there is tiny (7th decimal) variance, but for the most part all the derivatives equal the derivative at L=.01

```

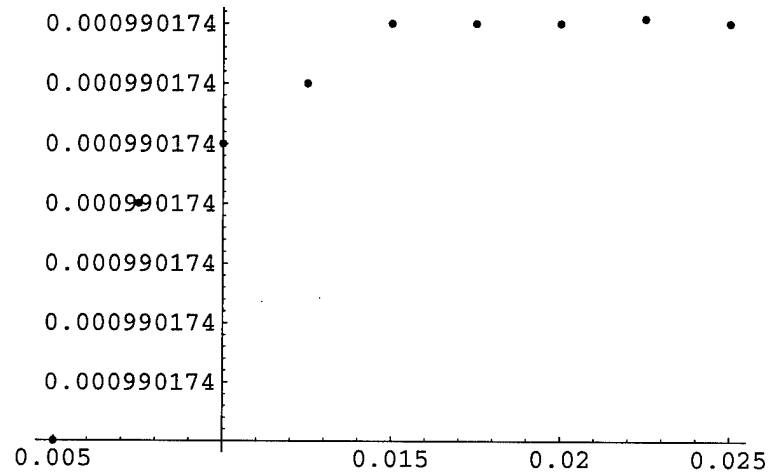
deriv0 = {{.01, 0.0009901742},
  {.005, 0.0009901737}, {.0075, 0.0009901741},
  {.0125, 0.0009901743}, {.015, 0.0009901744},
  {.0175, 0.0009901744}, {.02, 0.0009901744},
  {.0225, .00099017440809}, {.025, 0.0009901744}};

```

```
Fit[deriv0, {1,  $\sqrt{L}$ , L}, L]
```

```
0.000990172 + 4.08705  $\times 10^{-8}$   $\sqrt{L}$  - 1.47073  $\times 10^{-7}$  L
```

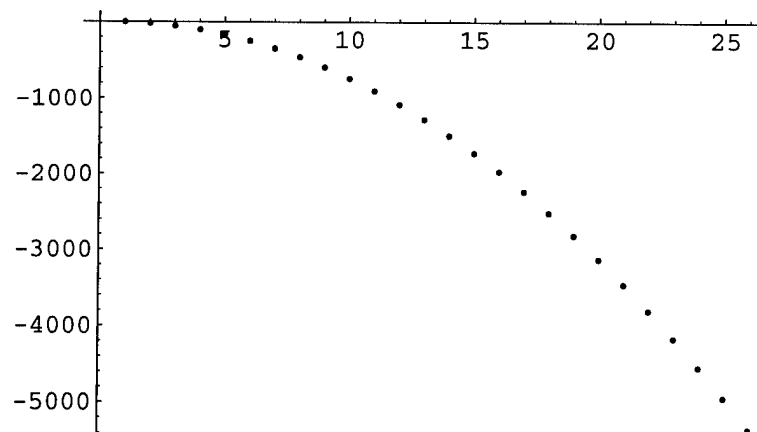
```
ListPlot[deriv0, PlotStyle -> PointSize[.01]];
```



#### ■ Roots Vary With K

The following roots were calculated in the file "varying.nb" for L=.01 with w= 1.

```
roots = -1 * {2.050722, 18.45649, 51.26802,  
100.4853, 166.1082, 248.1366, 346.5706,  
461.41, 592.6545, 740.3055, 904.3608, 1084.821,  
1281.686, 1494.955, 1724.629, 1970.708, 2233.19,  
2512.075, 2807.365, 3119.057, 3447.153, 3791.651,  
4152.551, 4529.853, 4923.557, 5333.662};  
a = ListPlot[roots];
```



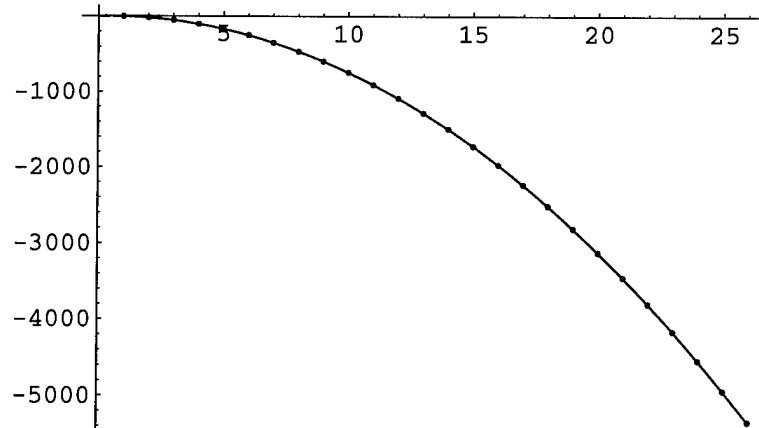
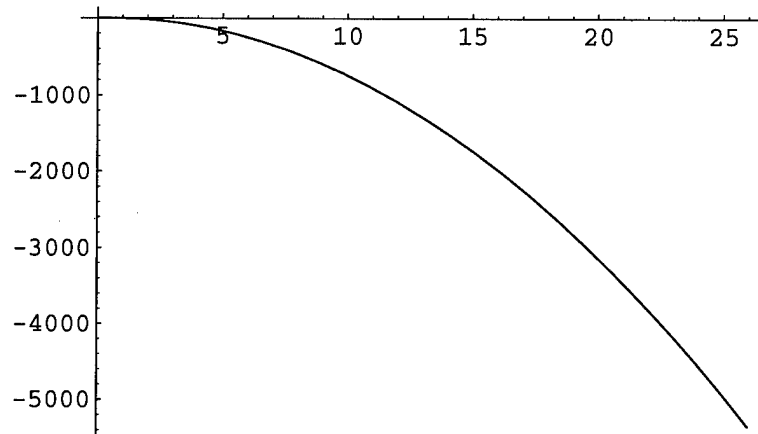
```
Fit[roots, {1, k, k^2}, k]
```

```
-2.02072 + 8.19207 k - 8.20216 k^2
```

```
rootfit[k_] := -2.02072 + 8.19207 * (k) - 8.20216 * (k)^2;
```

```
b = Plot[rootfit[k], {k, 0, 26}];
```

```
Show[a, b];
```



Now to see how well the fit holds for further values. The highest  $k$  I've used is 500. The thermal code generated:  $k=500, zk=-2.007824 \times 10^6$ . This fit gives a value of  $-2.04645 \times 10^6$ . Also, way out here the Derivative function has changed from 0.0009901742 to .0008234526, but by this time, the root is -70,000 so the error shouldn't make much of a difference!

■ **Combine the three effects:**

■ **Roots (All Cases Okay except the Very small (.004):**

I expect that  $Z(L,w,k) = \frac{.0001 * Z_0(k)}{-\omega * L^2}$  where  $Z_0(k)$   
 $= -2.02072 + 8.19207 * k - 8.20216 * k^2$

Here the fit is  $Z(L) = .0001 \frac{Z_0}{L^2}$  where  $Z_0 = Z(L=.01)$ , calculated by the root solver for each reed. Note that *Mathematica* calls  $Z_0[0]$   $Z_0[1]$  hence the use of +1 terms

$$\begin{aligned} \mathbf{z_0[k\_]} &:= -2.02072 + 8.19207 * (\mathbf{k + 1}) - 8.20216 * (\mathbf{k + 1})^2; \\ \mathbf{z_z[L\_ , \omega\_ , k\_]} &:= \frac{.0001 * \mathbf{z_0[k]}}{\omega * L^2}; \end{aligned}$$

Here is How my Approximation Performed for Calculating the Roots:

Data Point	Actual Values	Calculated Values	% Error
Zz[.01,1,500]:	-2.007824 * 10 <sup>6</sup>	-2.04645 * 10 <sup>6</sup>	1.9%
Zz[.01,8,25]:	-666.708	-666.711	.0005%
Zz[.0225,8,25]:	-131.7003	-131.696	.0032%
Zz[.03,14,12]	-10.1722	-10.1721	.001%
Zz[.004,29,250]:	-106512.	-110041.	3.3%
Zz[.225,8,25]:	-1.31702	-1.31696	.004%

■ **Derivatives- All Cases Good Except the Very Small (.004)**

It is seen that the derivatives do not change much with "L" and are essentially constant once calculated for a particular reed at a particular frequency. They do vary very slightly with k, a slight difference here which causes catastrophic differences in the actual temperature calculation!

$$\begin{aligned} \mathbf{Dd[L\_ , \omega\_ , k\_]} &:= \\ & (0.0009902715 - 3.328841 * 10^{-9} * \mathbf{IntegerPart[k]} - \\ & 7.094576316 * 10^{-10} * (\mathbf{IntegerPart[k]})^2) * \\ & \sqrt{\omega} \end{aligned}$$

Here is How my Approximation Performed for Calculating the Roots.

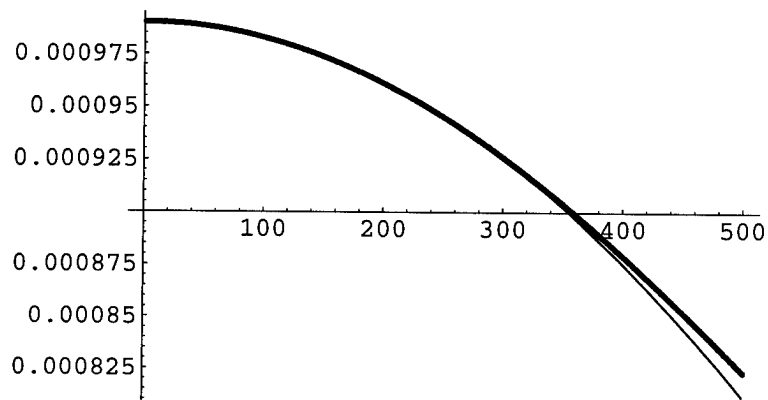
Data Point	Fitted Model	Actual Values	% Error
Dd[.01,1,500]:	0.000811243	0.000823453	1.5%
Dd[.01,8,25]:	0.00279942	0.00279928	.005%
Dd[.0225,8,25]:	0.00279942	0.00280037	.03%
Dd[.03,14,12]	0.00370472	0.00370485	.004%
Dd[.004,29,250]:	0.00508951	0.00402847	26%
Dd[.225,8,25]:	0.00279942	0.00280063	.04%

Here, the values in the list "dervs" have been calculated in the file "varying.nb" for L.01 and T = 1/1 Hz and were imported in without being displayed. The fit is:

```
derv = Flatten[dervs];
Derv[k_] := Fit[derv, {1, x, x^2}, x] /. x -> k
Derv[k]
0.000990272 - 3.32884 × 10-9 k - 7.09458 × 10-10 k2
```

The fit was using a data set up to 250. Now let's check predictability:

```
Derv[k_] :=
0.0009902715 - 3.328841 * 10-9 * IntegerPart[ k ] -
7.094576316 * 10-10 * (IntegerPart[k])2;
b = Plot[Derv[k], {k, 0, 500}];
Show[a, b];
```



### Application

Now to Apply Dr Baker's Solution, and my approximations, to the Mechanical Equations. Here I am only going to use the second layer. We are interested in the temperature profile between the 2nd and 3rd layers and find that the 3rd layer temperature is constant with the bottom of the 2nd layer temperature. I still need the parameters for the first layer, but only the equations for the 2nd layer. The reed parameters are the same as above, except that the alphas, gammas, and "little d's" are now functions of L and  $\omega$ . That block is not re-printed. The variable functions are now re-written as functions of length and chopper frequency.



## ■ The Root Solving Block -Approximations

Recall, above, that the approximations resulted in little error in the roots and derivative terms. However, one trait of these functions is that a slight difference in the fit can change the answer drastically. *Mathematica* calls the first term "1" when it's actually "0" so to calculate the proper terms, I use of "k+1"

```

lams[k_] := ((2 * IntegerPart[k] + 1) * Pi / 2)^2;
root0[k_] := -2.02072 + 8.19207 * IntegerPart[k + 1] -
8.20216 * (IntegerPart[k + 1])^2;
root[L_, ω_, k_] := .0001 * (root0[k]) /
ω * L^2;
sig[L_, ω_, k_] := sig[L, ω, k] = -root[L, ω, k];
derv[ω_, k_] :=
(0.0009902715 - 3.328841 * 10^-9 * IntegerPart[k] -
7.094576316 * 10^-10 * (IntegerPart[k])^2) * Sqrt[ω]
(*the derv is essentially constant with L.*)

w1[L_, ω_, k_] :=
w1[L, ω, k] = Im[Sqrt[(root[L, ω, k] + dd1[L, ω] * lams[k])]];
w2[L_, ω_, k_] :=
w2[L, ω, k] = Re[Sqrt[(root[L, ω, k] + dd2[L, ω] * lams[k])]];
w3[L_, ω_, k_] :=
w3[L, ω, k] = Re[Sqrt[(root[L, ω, k] + dd3[L, ω] * lams[k])]];

```

## ■ The Constant Functions "ck"

```

ck2[L_, ω_, k_] := ck2[L, ω, k] =
2 * Sqrt[dd1[L, ω] / dd2[L, ω]] * Sin[w1[L, ω, k] * gam1[L, ω]] /
w1[L, ω, k] * derv[ω, k];

```

## ■ The Time Behavior "I"

Incoming Energy

```

kk = 1;
(*this k represents an absorption of the top layer*)
Io = 1 * 10-6 (* this represents the initial intensity
of the incoming beam, I figure it's reduced quite
a bit because of the monochrometer and stuff *);
to = .5 (* fraction of period that signal is on,
due to chopper setup *);
p[t_] := p[t] = IntegerPart[t]

```

```

Ii[L_, ω_, t_, k_] := Ii[L, ω, t, k] =
  (kk * Io) / sig[L, ω, k] * E-sig[L, ω, k] * t *
  ( (Esig[L, ω, k] * to - 1) / (Esig[L, ω, k] - 1) *
    (Esig[L, ω, k] * p[t] - 1) - Esig[L, ω, k] * p[t] ) +
  (kk * Io) / sig[L, ω, k] *
  If[t - p[t] <= to, 1, E-sig[L, ω, k] * ((t - p[t]) - to)];

```

■ The X Behavior,  $\phi$ , or "Thi"

This is the only term that is effected by integration of the curvature to get deflection.

$$\phi_k(\zeta) = \frac{1}{\lambda_k^3} \text{Sine}(\lambda_k \zeta) + \frac{\zeta}{\lambda_k^2}$$

$$\text{lam}[k_] := \text{lam}[k] = \left( (2 * \text{IntegerPart}[k] + 1) * \frac{\text{Pi}}{2} \right);$$

$$\text{thiNew}[\xi_, k_] :=$$

$$\text{thiNew}[\xi, k] = \frac{1}{(\text{lam}[k])^3} * \text{Sin}[\text{lam}[k] * \xi] + \xi;$$

■ The Y Behavior,  $\psi$ , or "Psi"

$$\begin{aligned}
 \text{Aa}[L_, \omega_, k_] &:= \\
 \text{Aa}[L, \omega, k] &= \text{Cosh}[w3[L, \omega, k] * \text{gam3}[L, \omega]]; \\
 \text{Bb}[L_, \omega_, k_] &:= \text{Bb}[L, \omega, k] = \sqrt{\frac{dd3[L, \omega]}{dd2[L, \omega]}} * \\
 &\frac{w3[L, \omega, k]}{w2[L, \omega, k]} * \text{Sinh}[w3[L, \omega, k] * \text{gam3}[L, \omega]]; \\
 \text{Psi2}[\eta_, L_, \omega_, k_] &:= \text{Psi2}[\eta, L, \omega, k] = \text{Aa}[L, \omega, k] * \\
 &\text{Cosh}[w2[L, \omega, k] * \left( \frac{\eta}{\sqrt{dd2[L, \omega]}} + \text{gam2}[L, \omega] \right)] + \\
 &\text{Bb}[L, \omega, k] * \\
 &\text{Sinh}[w2[L, \omega, k] * \left( \frac{\eta}{\sqrt{dd2[L, \omega]}} + \text{gam2}[L, \omega] \right)];
 \end{aligned}$$

■ Deflection

*Mathematica* is very strange about using units. It does not like to cancel units even when they obviously cancel, so occasionally I have to force the program to cancel, hence use of such terms as " kelvin, and Meter<sup>2</sup>" For example, *Mathematica* will not cancel  $\frac{1}{\text{Meter}} \sqrt{\text{Meter}^2}$ . The deflection as a function of frequency is adapted from the article "Photothermal measurements at picowatt resolution using uncooled micro-optomechanical sensors" Varesi, Lai et al. Notice that the maximum deflection does NOT occur at resonance here. I expected it to peak there.

```

kmax = 50;
kb = BoltzmannConstant
(* 1.38065800000000017*10-23 in J/K *);
T = 298 Kelvin (* room temperature*);
B = 8; (*Measurement Bandwidth *)
Q = 20; (* FWHM of peak at resonance *)
kc[L_] :=  $\frac{w}{4 * (L \text{ Meter})^3} * (E3 * t3^3 + E2 * t2^3)$ 
m[L_] :=
  (*effective*) SI[.24 * w * (L Meter) * (ro3 * t3 + ro2 * t2)]
wo[L_] := Convert[ $\sqrt{\text{SI}\left[\frac{\text{kc}[L]}{\text{m}[L]}\right] * \text{Second}^2, 1}$ ];
(*output in Hertz *)
zz[L_,  $\omega$ _,  $\tau$ _] := zz[L,  $\omega$ ,  $\tau$ ] = 6 * (alpha3 - alpha2) *
   $\left(\frac{(t3 + t2)}{t2^2 * K}\right) * \sum_{k=0}^{kmax} \text{ck2}[L, \omega, k] * \text{Ii}[L, \omega, \tau, k] * \text{Psi2}[\text{alph1}[L], L, \omega, k] * \text{thiNew}[1, k] \text{ Meter}$ 
   $\text{Meter Kelvin} * \frac{1}{\sqrt{\left(1 + \frac{\omega^2}{(\text{wo}[L])^2}\right)}} * (\text{wo}[L])^2 /$ 
   $\left(\sqrt{\left(\left((\text{wo}[L])^2 - (\omega)^2\right)^2 + \frac{(\text{wo}[L])^2 * (\omega)^2}{Q}\right)}\right);$ 

```

### ■ Thermal Noise

RMS Noise (Thermally Induced Lever Noise), based on Sarid Book.

$$\begin{aligned}
 Wp[L_, \omega_] := & \text{Convert}\left[\sqrt{\frac{4 * kb * T * B}{kc[L] * \text{wo}[L] * Q}} * \right. \\
 & \left. \frac{(\text{wo}[L])^2}{\left(\sqrt{\left(\left((\text{wo}[L])^2 - (\omega)^2\right)^2 + (\text{wo}[L])^2 * (\omega)^2\right)}\right)}, \right. \\
 & \left. \sqrt{\text{Meter}^2}\right] * \\
 & \frac{\text{Meter}}{\sqrt{\text{Meter}^2}};
 \end{aligned}$$

The second term is unitless if both frequencies are written in hertz, so the unit is removed from the terms that already have it to appease Mathematica. Also, the terms below are canceled in terms of Meters, assuring that SNR is the correct breed of unitless.

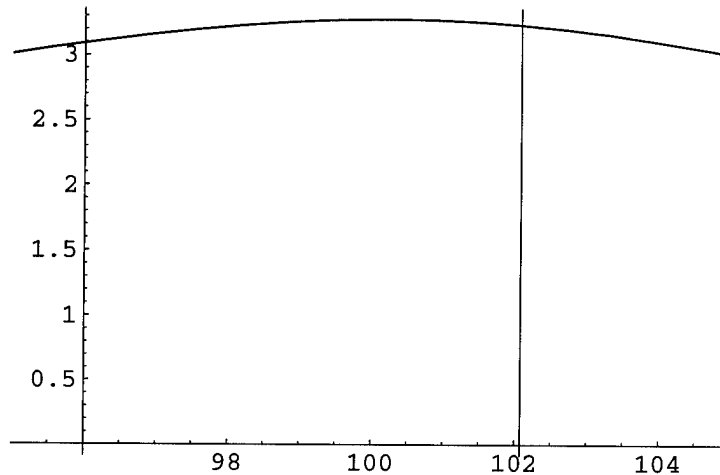
$$\text{SigNoise}[L_, f_] := \text{SigNoise}[L, f] = \frac{\text{zz}[L, f, 20.5]}{\text{Meter}} * \sqrt{\text{Convert}\left[\frac{Q^2 * kc[L] * wo[L]}{4 * kb * T} * \text{Meter}^2, 1\right]}$$

The second term is unitless if both frequencies are written in hertz, so the unit is removed from the terms that already have it to make MMA happy.

### ■ Sample Output

Plot of Deflection vs Chopper frequency, blow up to show that the peak does not occur at the resonant frequency (shown by the line).

```
Plot[ $\frac{\text{zz}[\text{.0225}, f, 20.5]}{\text{Meter}}$ ,
{f, 1, 130}, GridLines -> {{wo[.0225]}, None},
PlotRange -> {{95, 105}, Automatic}];
```



This peaks at 100, with a max at 3.1,  $wo = 102.08$

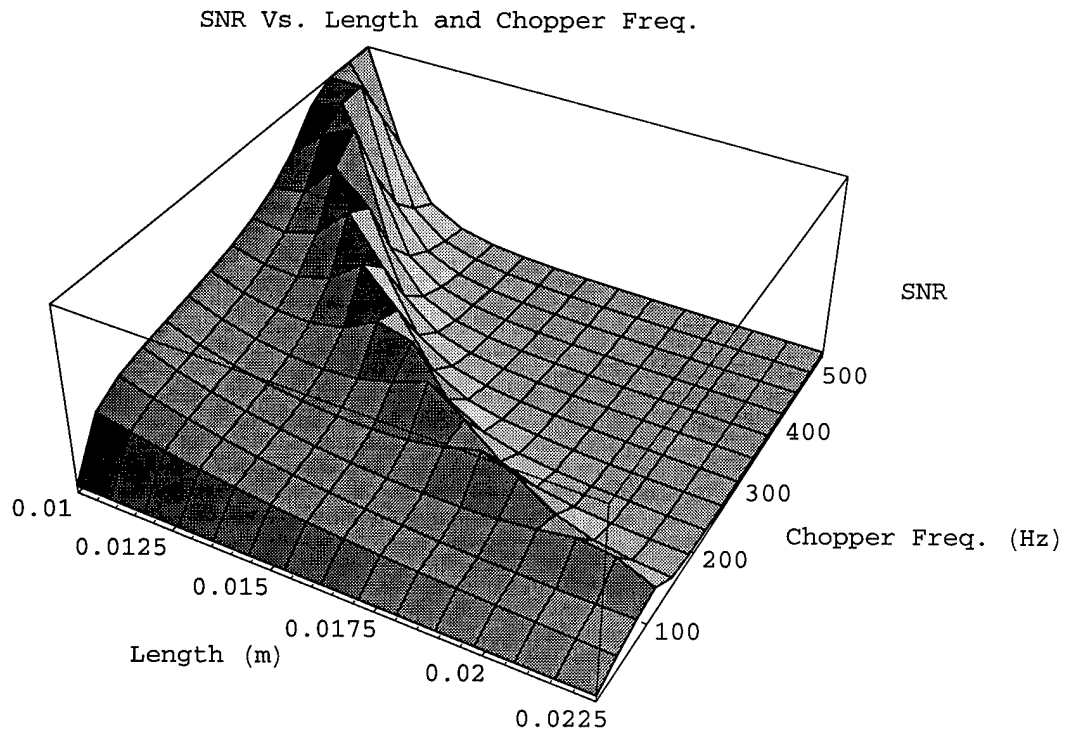
.015 m reed: peaks at 225.5, at again about 3.25,  $wo = 229.7$

.01 m reed: peaks at 508 at 3.25,  $wo = 516.8$

Difference grows inversely proportional to length- ~2, 4, 9 difference, corresponding to a 2%, 1.8% and 1.7% drop.

Now to generate a 3D plot of sensitivity:

```
Plot3D[SigNoise[L, f],  
  {L, .01, .0225}, {f, 1, 525}, AxesLabel ->  
  {"Length (m)", "Chopper Freq. (Hz)", "SNR"},  
  PlotLabel -> "SNR Vs. Length and Chopper Freq.",  
  AxesEdge -> {Automatic, Automatic, {1, 1}},  
  Ticks -> {Automatic, {100, 200, 300, 400, 500}, None}];
```



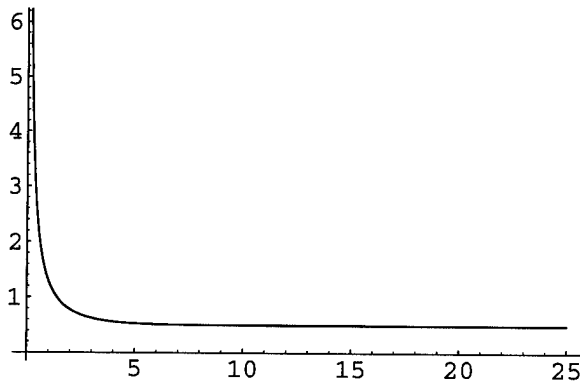
## Phase Analysis

■ T1/2 points

Here, I look at what times the amplitude is one half of maximum. On the rise, this time is called  $t_e$  and on the fall this time is called  $t_L$ . Phase shift will be recognized by a change in the difference between these two times. Using the time varying part of the thermal solution, I, the following equation is obtained for that difference in time, as a function of the root:

$$t_L - t_e = \frac{1}{\sigma} \ln(2 + e^{\frac{\sigma}{2}})$$

```
delt[sig_] := 1/sig * Log[2 + E^(sig/2)];
Plot[N[delt[sig]], {sig, .001, 25}];
```



The function quickly goes to the constant value of 1/2. Thus, phase information can be adequately described by using only the first root term. There is some loss of accuracy, but the general trends will still be observed.

■ Reed Parameters (same as in previous file, not reproduced)

■ The Root Solving Block - We only need the First Root, sig, for now.  
(same as previous file, only root value reproduced)

k	$\lambda_k$	$-d_2 \lambda_k^2$	$z_k$	$\frac{\partial D}{\partial s}(z_k)$	$\mu_1(z_k)$
0	$\frac{\pi}{2}$	-0.05608007	$-0.05063511 + 0. I$	$0.002800636 + 0. I$	$0. + 0.2183303$

## ■ I Analysis, After Many Periods

After a large amount of periods has passed, the incoming energy deposition function can be written as:

```

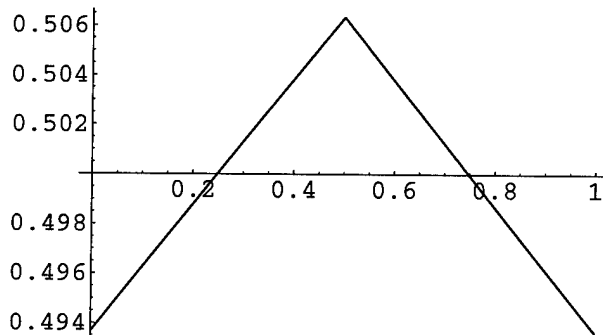
kk = 1;      (* absorption *)
Io = 1;      (* initial intensity *)
to = .5      (* fraction of period that signal is on *);
p[t_] := p[t] = IntegerPart[t]
(*number of periods that has passed thus far *)

(* short term behavior *)
Ia[t_] :=  $\frac{kk * Io}{sig} * E^{-sig * t} * \left( \frac{(E^{sig * to} - 1)}{(E^{sig} - 1)} * (E^{sig * p[t]} - 1) - E^{sig * p[t]} \right) +$ 
 $\frac{kk * Io}{sig} * \text{If}[t - p[t] <= to, 1, E^{-sig * ((t - p[t]) - to)}];$ 

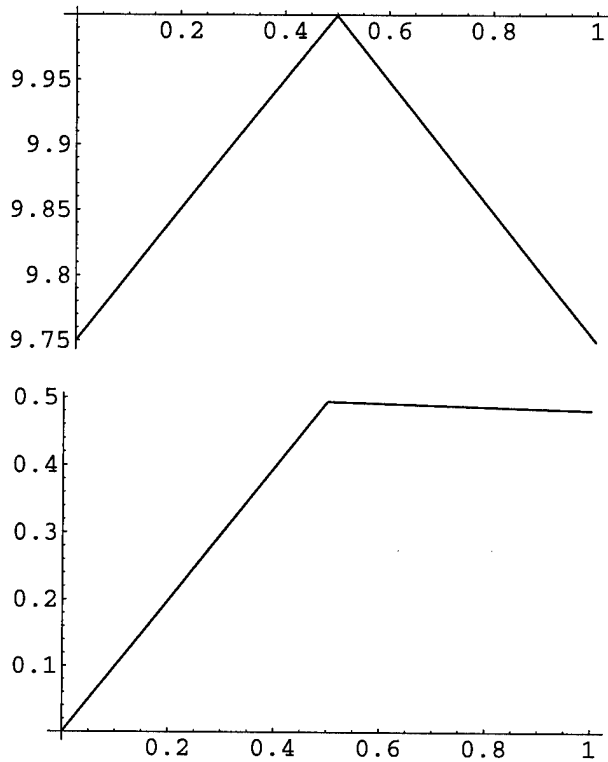
(* long term behavior *)
Ib[t_] :=  $\frac{kk * Io}{sig} * \left( \frac{(E^{sig * to} - 1)}{(E^{sig} - 1)} - 1 \right) * E^{-sig * (t - p[t])} +$ 
 $\frac{kk * Io}{sig} * \text{If}[t - p[t] <= to, 1, E^{-sig * ((t - p[t]) - to)}];$ 

(*long term behavior, not modulated by the constant terms *)
Ic[t_] :=
 $\left( \frac{(E^{sig * to} - 1)}{(E^{sig} - 1)} - 1 \right) * E^{-sig * (t - p[t])} + \text{If}[t - p[t] <= to, 1, E^{-sig * ((t - p[t]) - to)}];$ 
Plot[Ic[t], {t, 0, 1}];
Plot[Ib[t], {t, 0, 1}];
Plot[Ia[t], {t, 0, 1}];

```







This is Strange... the expected shape is not evident. Here it appears linear!

$$I_b[.5] - I_b[0]$$

$$0.249987$$

The amplitude difference in one period is seen as about .25. This is consistent with the following analysis:

#### ■ I Min and Max

For Large Periods, the minimum and maximum values of the time dependant portion are fairly constant. The most important quantity, however is the *difference* between the two. The max, min, and the difference, as a function of the root itself, can be obtained from the long term equation as:

$$I_{\max} = \frac{1}{\sigma} \frac{1}{1+e^{-\frac{\sigma}{2}}}$$

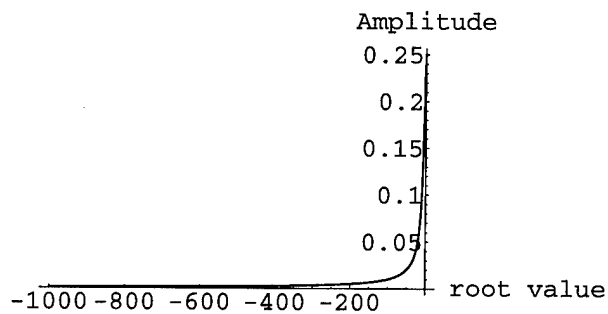
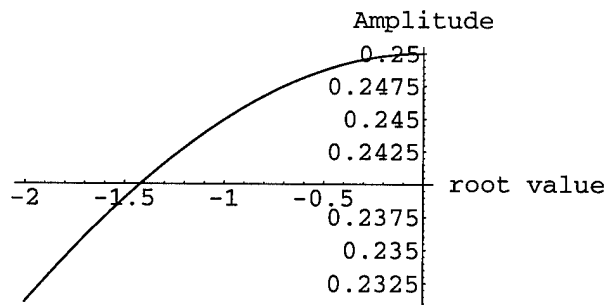
$$I_{\min} = \frac{1}{\sigma} \frac{e^{-\frac{\sigma}{2}}}{1+e^{-\frac{\sigma}{2}}}$$

$$\text{Amplitude} = I_{\max} - I_{\min} = \frac{1}{\sigma} \tanh\left(\frac{\sigma}{4}\right)$$

```

Imax[sig_] :=  $\frac{1}{\text{sig}} \frac{1}{1 + E^{-\frac{\text{sig}}{2}}}$ ;
Imin[sig_] :=  $\frac{1}{\text{sig}} \frac{E^{-\frac{\text{sig}}{2}}}{1 + E^{-\frac{\text{sig}}{2}}}$ ;
Amp[sig_] :=  $\frac{1}{\text{sig}} \text{Tanh}\left[\frac{\text{sig}}{4}\right]$ ;
Plot[{Amp[sig], Imax[sig] - Imin[sig]},
{sig, -2, 0}, AxesLabel -> {"root value", "Amplitude"}];
Plot[{Amp[sig], Imax[sig] - Imin[sig]}, {sig, -1000, 0},
AxesLabel -> {"root value", "Amplitude"}];

```

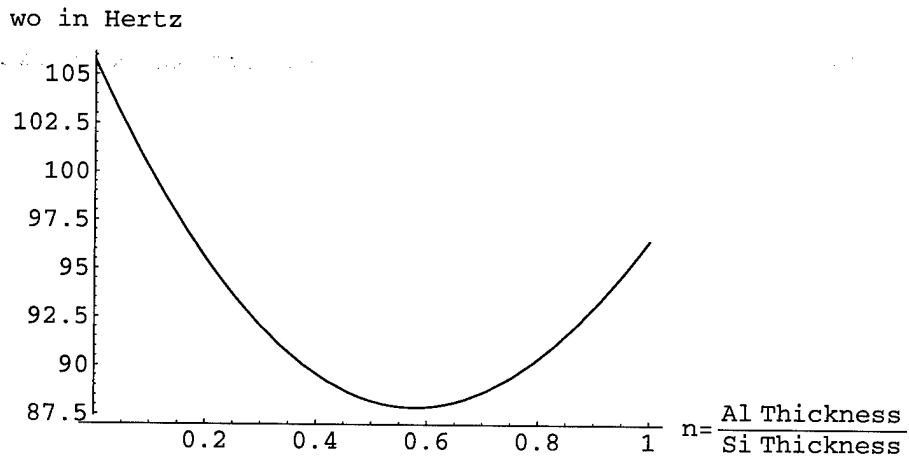


The Amplitude starts off at about .25 for the smaller roots, and quickly approaches zero as the roots grow in magnitude. The roots, as determined previously, start off at a small negative number and then progress quickly to negative numbers far beyond the range of the plot. Thus, using the first root is a valid approximation for future behaviour analysis.

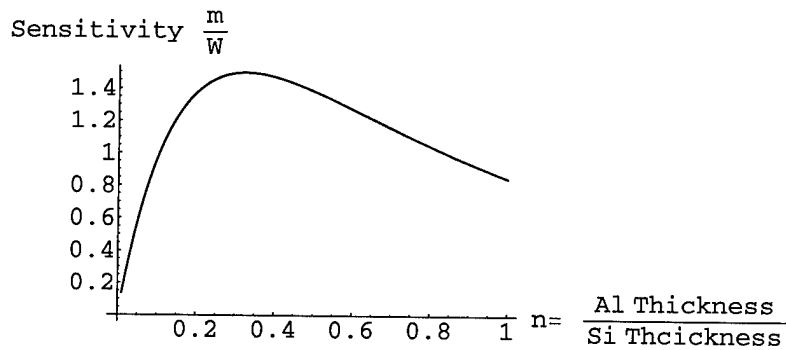
## ■ Resonance and Optimum Thickness Exploration

### ■ Important Results, presented upfront:

wo[.0225 m]= 102.078 Hertz  
wo[.015 m]= 229.676 Hertz  
wo[.01 m]= 516.771 Hertz  
wo[.009 m]= 637.989 Hertz

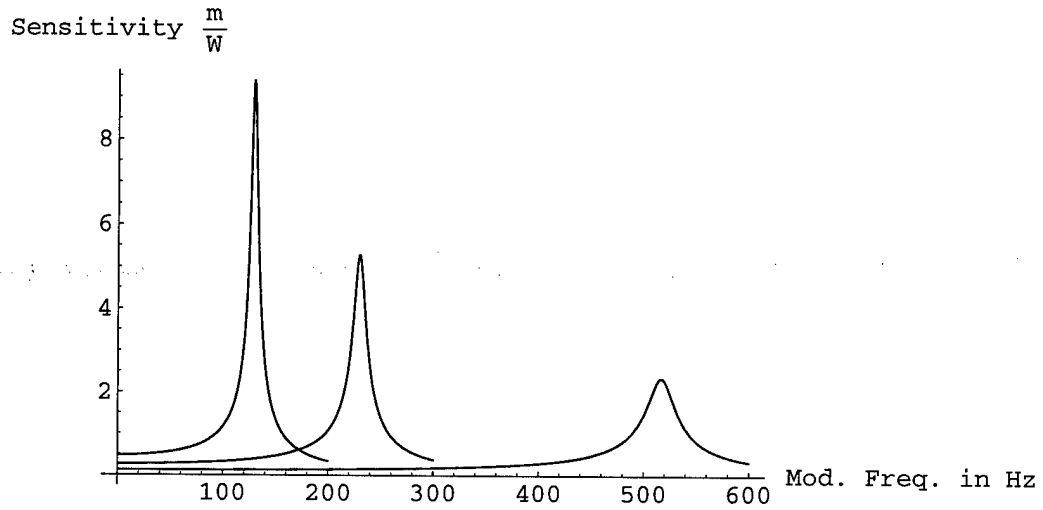


Note that the wider the reed gets, compared to the same length, the less sensitive the reed is overall.

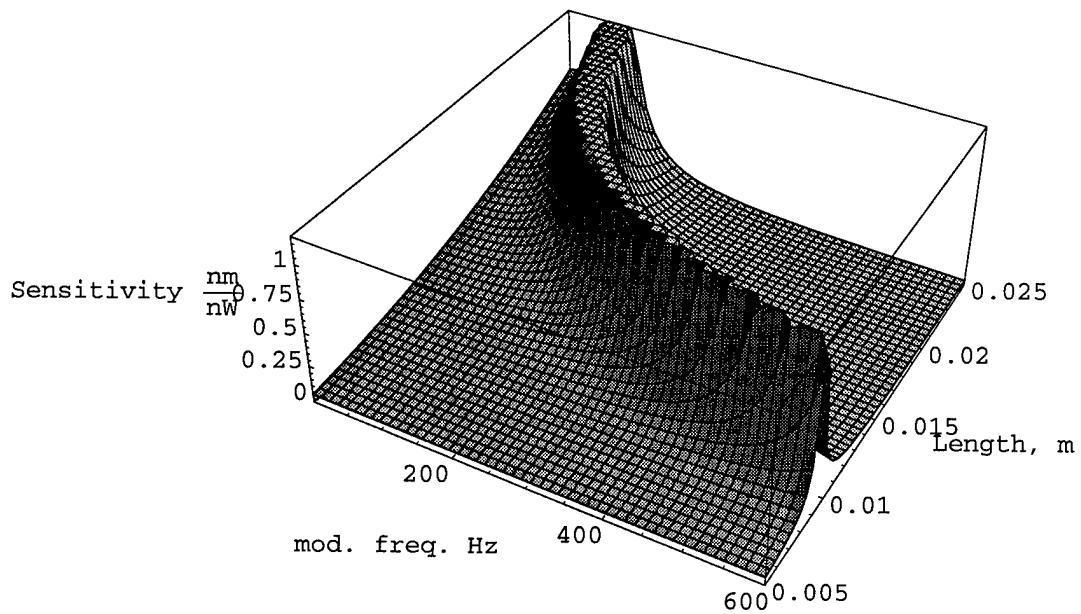


A Close Up reveals the optimum to be at .325, this optimum is not affected by length or width changes.

### Sensitivity Change with length and modulation frequency



As length increases, resonant frequency increases and sensitivity decreases. If the same amount of energy is absorbed in the reed for all three lengths (.02 m, .015 m, and .01 m) then the deflection behavior will be similar to this sensitivity relationship



This 3-D graph shows the effect of chopper frequency and length of the reed on the sensitivity. Notice, from the shape of the graph, that current reeds in testing have resonant frequencies so low that they are already operating in their resonant frequency, their most sensitive area!

#### ■ Reed Parameters

```
<< Miscellaneous`Units`;
<< Miscellaneous`PhysicalConstants`

L = .02 Meter;
w = .002 Meter;

(* Layer one, MgAl2O4: Hartnett's values *)
t1 = 1 * 10-6 Meter;
rho1 = 3.58  $\frac{\text{Gram}}{\text{Centimeter}^3}$ ;
E1 = 2.77 * 1011  $\frac{\text{Newton}}{\text{Meter}^2}$ ; (*elastic modulus*)
```

$$\text{lam1} = 14.6 \frac{\text{Watt}}{\text{Meter} * \text{Kelvin}} (*\text{thermal conductivity} *);$$

$$\text{alpha1} = 6.5 * 10^{-6} \frac{1}{\text{Kelvin}}; (*\text{thermal expansion for 30-00 C} *)$$

$$\text{cp1} = .200 \frac{\text{Calorie}}{\text{Gram} * \text{Celsius}}; (*\text{at 20 C Roy' s value} *)$$

$$\text{Diff1} = \text{Convert} \left[ \frac{\text{lam1}}{\text{cp1} * \text{ro1}}, \frac{\text{Micro Meter}^2}{\text{Second}} \right];$$

(\* Layer two Silicon \*)

$$\text{t2} = 8 * 10^{-6} \text{ Meter};$$

$$\text{ro2} = 2328 \frac{\text{Kilogram}}{\text{Meter}^3};$$

$$\text{E2} = 1 * 10^{11} \frac{\text{Newton}}{\text{Meter}^2};$$

$$\text{lam2} = 150 \frac{\text{Watt}}{\text{Meter Kelvin}};$$

$$\text{alpha2} = 2.6 * 10^{-6} \frac{1}{\text{Kelvin}};$$

$$\text{cp2} = 700 \frac{\text{Joule}}{\text{Kilogram Kelvin}};$$

$$\text{Diff2} = \text{N} \left[ \text{Convert} \left[ \frac{\text{lam2}}{\text{cp2} * \text{ro2}}, \frac{\text{Micro Meter}^2}{\text{Second}} \right] \right];$$

(\* Layer three Aluminum \*)

$$\text{t3} = .5 * 10^{-6} \text{ Meter}; \quad (*\text{thickness} *)$$

$$\text{ro3} = 2702 \frac{\text{Kilogram}}{\text{Meter}^3}; \quad (* \text{ density } *)$$

$$\text{E3} = .8 * 10^{11} \frac{\text{Newton}}{\text{Meter}^2}; \quad (* \text{ Elastic Modulus } *)$$

$$\text{lam3} = 237 \frac{\text{Watt}}{\text{Meter Kelvin}}; \quad (*\text{thermal conductivity} *)$$

$$\text{alpha3} = 23.6 * 10^{-6} \frac{1}{\text{Kelvin}}; \quad (*\text{thermal expansion} *)$$

$$\text{cp3} = 908 \frac{\text{Joule}}{\text{Kilogram Kelvin}}; \quad (*\text{heat capacity} *)$$

$$\text{Diff3} = \text{N} \left[ \text{Convert} \left[ \frac{\text{lam3}}{\text{cp3} * \text{ro3}}, \frac{\text{Micro Meter}^2}{\text{Second}} \right] \right];$$

Printout of the Diffusion Coefficients:

Diff1

Diff2

Diff3

$$\frac{4.87032 \text{ Meter}^2 \text{ Micro}}{\text{Second}}$$

$$\frac{92.0471 \text{ Meter}^2 \text{ Micro}}{\text{Second}}$$

$$\frac{96.6 \text{ Meter}^2 \text{ Micro}}{\text{Second}}$$

### ■ Mechanical Resonance Prediction

$$k[L_, n_] := \frac{w}{4 * (L \text{ Meter})^3} * t2^3 (E3 * n^3 + E2)$$

$$m[L_, n_] := (*effective*) SI[.24 * w * (L \text{ Meter}) * t2 (ro3 * n + ro2)]$$

$$wo[L_, n_] := \text{Convert} \left[ \sqrt{\text{SI} \left[ \frac{k[L, n]}{m[L, n]} \right] * \text{Second}^2, 1} \right] \text{ Hertz};$$

wo[.0225, .0625]

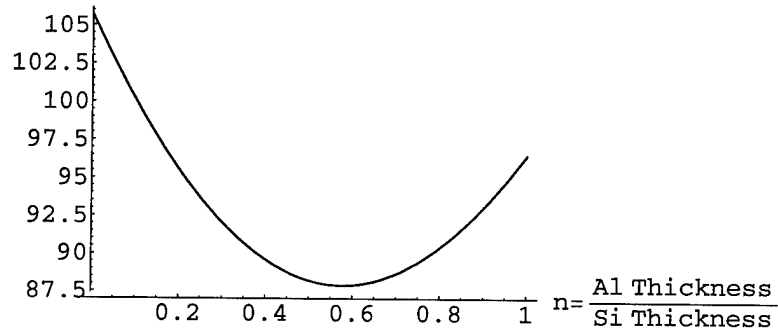
102.078 Hertz

Plot[ $\frac{wo[.0225, n]}{\text{Hertz}}$ , {n, 0, 1},

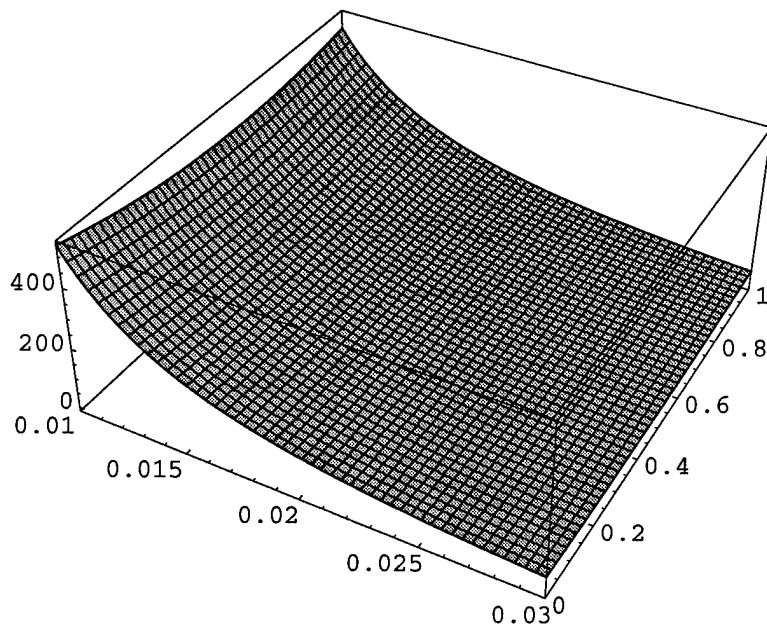
AxisLabel -> {"n="  $\frac{\text{Al Thickness}}{\text{Si Thickness}}$  ", "wo in Hertz"},

AxisOrigin -> {0, 87}];

wo in Hertz



```
Plot3D[ $\frac{\omega[L, n]}{\text{Hertz}}$ , {L, .01, .03}, {n, 0, 1}, PlotPoints -> 50];
```



Be sure to note that  $n$  is the ratio. ( $n = \frac{\text{Al Thickness}}{\text{Si Thickness}}$ ) The change of Resonant frequency WRT length has the same shape for each thickness of Aluminum layer. As is better seen in the 2D graph, the resonant frequency hits a minimum at about  $n = .6$ . This means for minimum resonant frequency, we'd want to operate with an aluminum layer that was 4.8 microns thick. We may want to operate at minimum resonant frequency, because the tests show that smaller reeds are more stable- also, the equipment may be more stable if we can bring the resonant frequency down.

■ **Optimum Thickness Ratio Prediction**

■ **thickness ratio ( $n$ ) effect on sensitivity:**

Here the effect on varying the thickness of the Aluminum layer with respect to that of the Silicon layer is explored. The silicon layer is held constant because it is the pre-purchased material. The ratio  $n = \frac{t_3}{t_2}$  or  $\frac{\text{Al thickness}}{\text{Si thickness}}$ .



(\* Young's Modulus \*)

$$n = \frac{t1}{t2};$$

$$thi = \frac{E1}{E2};$$

$$K = 4 + 6 * n + 4 * n^2 + thi * n^3 + \frac{1}{thi * n}$$

7.706

(\* Several Other Ratios of  $\frac{Al}{Si}$  that are handy: \*)

$$\gamma = \frac{\lambda_3}{\lambda_2};$$

$$\beta = \frac{\alpha_3}{\alpha_2};$$

$$\theta = \frac{(\beta - 1) * (n + 1)}{K * (\gamma * n + 1)};$$

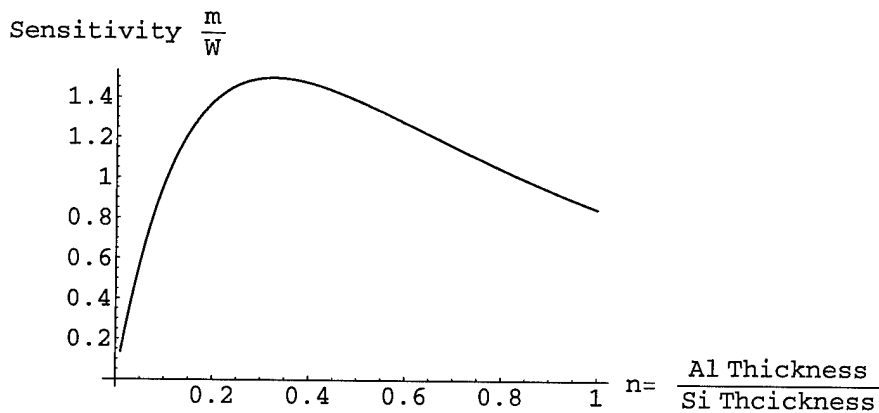
$$\psi = \frac{r_3}{r_2};$$

S[n, L, w] :=

$$2 * \frac{\alpha_2}{\lambda_2} \frac{L^3}{t^2 * w} * \frac{(\beta - 1) * (n + 1)}{(4 + 6 * n + 4 * n^2 + thi * n^3 + \frac{1}{thi * n}) * (\gamma * n + 1)}$$

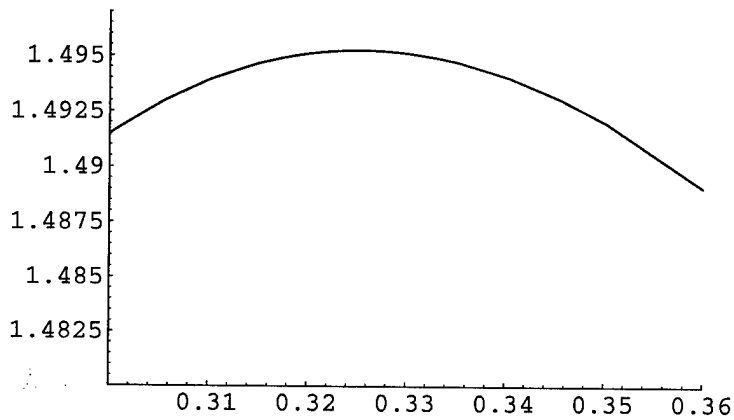
Plot[(S[n, L, w] \*  $\frac{\text{Watt}}{\text{Meter}}$ ), {n, .01, 1}, PlotPoints -> 100,

AxisLabel -> {"n =  $\frac{\text{Al Thickness}}{\text{Si Thickness}}$ ", "Sensitivity  $\frac{m}{W}$ "}];

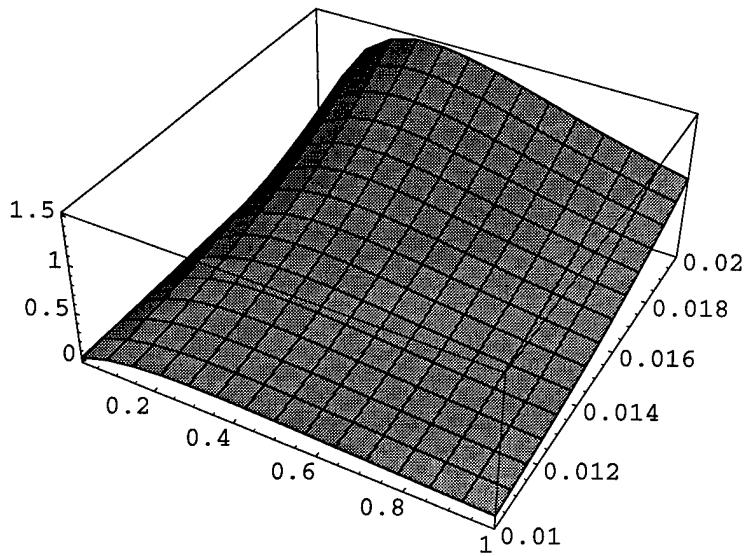


A close up reveals the optimum to be at 0.325:

```
Plot[ (S[n, L, w] *  $\frac{\text{Watt}}{\text{Meter}}$ ), {n, .01, 1}, PlotPoints -> 100,
PlotRange -> {{.3, .36}, {1.48, 1.497}}];
```



```
Plot3D[S[n, L Meter, w] *  $\frac{\text{Watt}}{\text{Meter}}$ , {n, .01, 1}, {L, .01, .02}];
```



Note that the ridge stays along  $n=0.325$ . Also, note that the wider the reed gets, compared to the same length, the less sensitive the reed is overall.

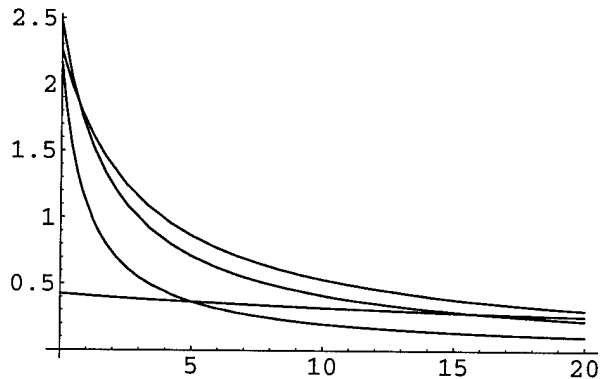
■ Sensitivity Optimum Other Ratios? Conductivity, Expansion?

```

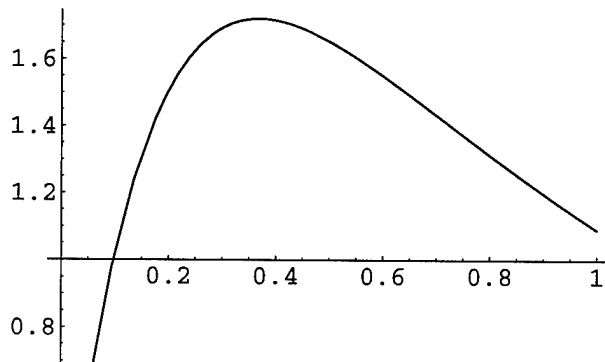
S[n_, ga_] :=
  2 *  $\frac{\alpha^2}{\lambda^2} \frac{L^3}{t^2 * w} * \frac{(\beta - 1) * (n + 1)}{(4 + 6 * n + 4 * n^2 + \theta_i * n^3 + \frac{1}{\theta_i * n}) * (g_a * n + 1)}$ ;
a = Plot[S[.0325, ga] *  $\frac{\text{Watt}}{\text{Meter}}$ , {ga, .01, 20} (*, PlotPoints->100*)
  (*, AxesLabel->{"ga=  $\frac{\text{Al Conduc.}}{\text{Si Conduc.}}$ ", "Sensitivity  $\frac{\text{m}}{\text{W}}$ "})];
b = Plot[S[.325, ga] *  $\frac{\text{Watt}}{\text{Meter}}$ , {ga, .01, 20} (*, PlotPoints->100*)
  (*, AxesLabel->{"ga=  $\frac{\text{Al Conduc.}}{\text{Si Conduc.}}$ ", "Sensitivity  $\frac{\text{m}}{\text{W}}$ "})];
c = Plot[S[.5, ga] *  $\frac{\text{Watt}}{\text{Meter}}$ , {ga, .01, 20} (*, PlotPoints->100*)
  (*, AxesLabel->{"ga=  $\frac{\text{Al Conduc.}}{\text{Si Conduc.}}$ ", "Sensitivity  $\frac{\text{m}}{\text{W}}$ "})];
d = Plot[S[1, ga] *  $\frac{\text{Watt}}{\text{Meter}}$ , {ga, .01, 20} (*, PlotPoints->100*)
  (*, AxesLabel->{"ga=  $\frac{\text{Al Conduc.}}{\text{Si Conduc.}}$ ", "Sensitivity  $\frac{\text{m}}{\text{W}}$ "})];
Show[a, b, c, d];

```

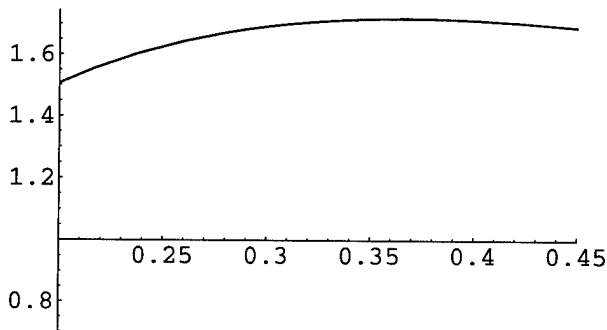
Below is a plot of sensitivity variance with conductivity ratios, the conductivity of the bottom material divided by the silicon conductivity.



```
Plot[S[n, 1] *  $\frac{\text{Watt}}{\text{Meter}}$ , {n, .01, 1}];
```



```
Plot[S[n, 1] *  $\frac{\text{Watt}}{\text{Meter}}$ , {n, .01, 1},  
PlotRange -> {{.2, .45}, Automatic}];
```



For a conductivity ratio of 1, the optimum thickness ratio changes to  $n = .367$ . Also, went up from 1.495 at max to about 1.718 This makes sense. If you make the bottom layer less conductive, it will require more of itself to keep in balance.

■ **Sensitivity as a function of frequency (assuming  $w = .1 L$ ) for three different lengths**

Also Assuming  $Q=20$ , a value that seems reasonable judging from the literature. This must actually be measured in the lab once the resonance peak has been graphed out and is dependent on resonant frequency, thus also length of the reed though I've assumed it constant.

Reed Parameters block, identical to that printed earlier in this file, has been hidden for printing.

- 2 cm Reed (the equations are reproduced only for this case, but similar ones were used to produce the other peaks on the graph)

Units are thrown around and balanced because *Mathematica* does not like to operate on units as well as it could.

$$L = .02 \text{ Meter};$$

$$w = .1 * L;$$

$$k = \frac{w}{4 * (L)^3} * (E3 * t3^3 + E2 * t2^3)$$

$$m = (*effective*) SI[.24 * w * (L) * (ro3 * t3 + ro2 * t2)]$$

$$\frac{k}{m}$$

$$wo = \text{Convert}\left[\sqrt{SI\left[\frac{k}{m}\right] * \text{Second}^2}, 1\right] \text{ Hertz}$$

$$S[\text{cm}_] := 2 * (\text{alpha1} - \text{alpha2}) * \left(\frac{(t1 + t2)}{t2^2 * K}\right) *$$

$$\frac{L^3}{(\text{lam1} * t1 + \text{lam2} * t2) * w} * \frac{wo^2}{\sqrt{\left((wo^2 - \text{cm}^2)^2 + \frac{wo^2 * \text{cm}^2}{Q^2}\right) * \frac{1}{\text{Hertz}^4}} \text{ Hertz}^2};$$

Sen[4 Hertz]

$$\frac{0.00320062 \text{ Newton}}{\text{Meter}}$$

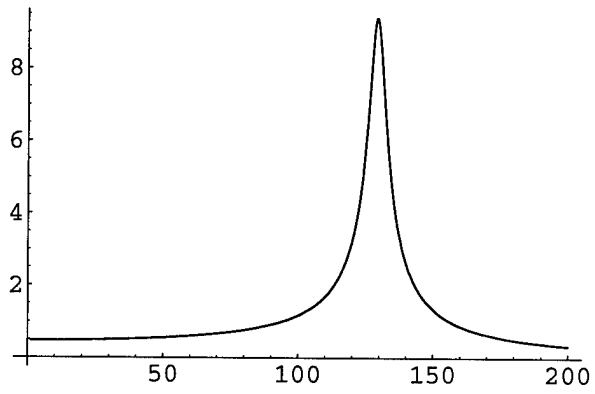
$$1.9176 \times 10^{-7} \text{ Kilogram}$$

$$\frac{16690.8 \text{ Newton}}{\text{Kilogram Meter}}$$

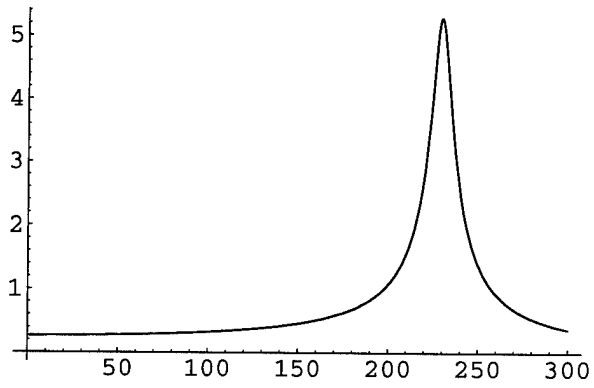
$$129.193 \text{ Hertz}$$

$$\frac{0.469214 \text{ Meter}}{\text{Watt}}$$

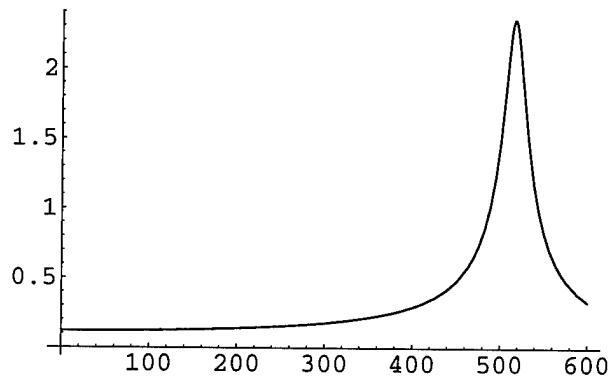
a = Plot [S[cm Hertz] \*  $\frac{\text{Watt}}{\text{Meter}}$ , {cm, 1, 200}];



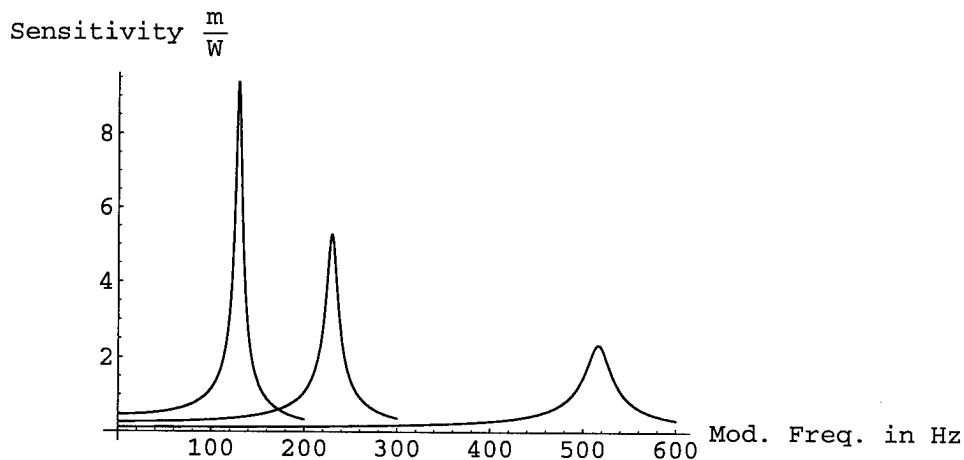
■ 1.5 cm Reed



■ 1 cm Reed



Show[a, b, c, AxesLabel -> {"Mod. Freq. in Hz", "Sensitivity  $\frac{m}{W}$ "}];



■ 3D Plot, length along one axis, and frequency along another, assuming  $w = .1 L$ .

The first half of the equation is normal, but the unit play in the second half is because of *Mathematica's* intrinsic funnyness. Originally, this program was chosen for ease of use, but this is only the case for scaled work.

```
w[L_] := .1 * L;
kk[L_] :=  $\frac{w[L]}{4 * (L \text{ Meter})^3} * (E3 * t3^3 + E2 * t2^3)$ 
mm[L_] := (*effective*) SI[.24 * w[L] * (L Meter) * (ro3 * t3 + ro2 * t2)]
wwo[L_] := Convert[ $\sqrt{SI[\frac{kk[L]}{mm[L]}] * \text{Second}^2, 1}$ ] Hertz;
Sen[cm_, L_] :=

$$2 * (\text{alpha1} - \text{alpha2}) * \left( \frac{(t1 + t2)}{t2^2 * K} \right) * \frac{L^3}{(\text{lam1} * t1 + \text{lam2} * t2) * w[L]} * \frac{(wwo[\frac{L}{\text{Meter}}])^2}{\sqrt{\left( (wwo[\frac{L}{\text{Meter}}])^2 - \text{cm}^2 \right)^2 + \frac{(wwo[\frac{L}{\text{Meter}}])^2 * \text{cm}^2}{Q^2}}} * \frac{1}{\text{Hertz}^4} \text{Hertz}^2$$
;
Sen[4 Hertz, .02 Meter]

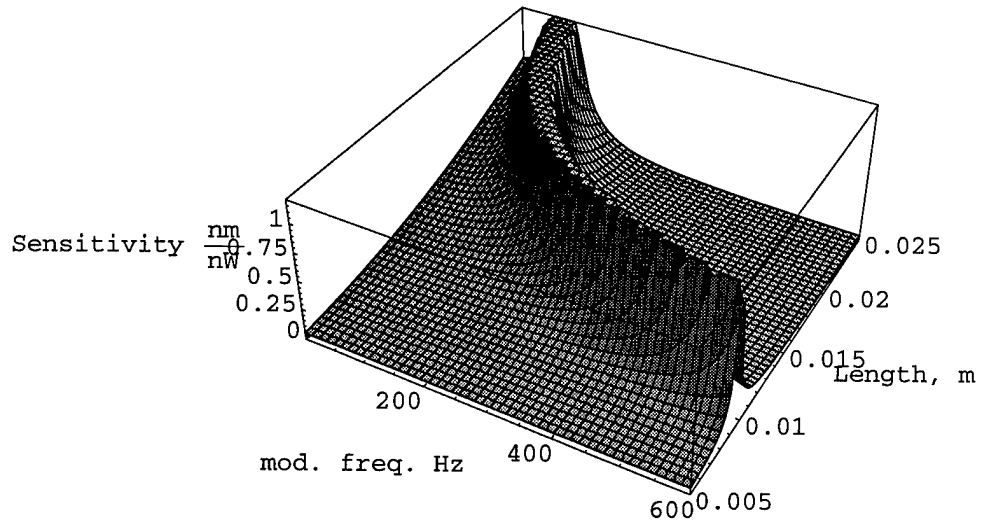
$$\frac{0.469214 \text{ Meter}}{\text{Watt}}$$

```

```

Plot3D[
  Sen[cm Hertz, L Meter] *  $\frac{\text{Watt}}{\text{Meter}}$ , {cm, 1, 600}, {L, .005, .025},
  AxesLabel -> {"mod. freq. Hz", "Length, m", "Sensitivity  $\frac{\text{nm}}{\text{nW}}$ "},
  PlotPoints -> 50];

```





■ More Resonance Plots

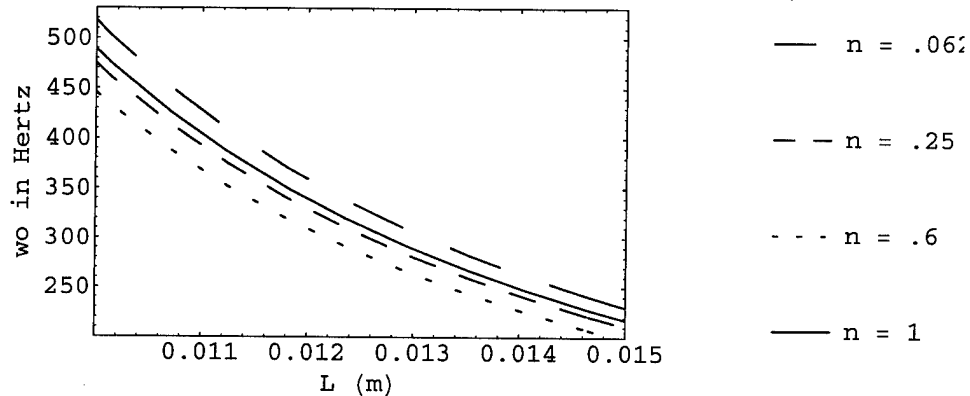
```

<< Graphics`Legend`;
k[L_, n_] :=  $\frac{w}{4 * (L \text{ Meter})^3} * t2^3 (E3 * n^3 + E2)$ 
m[L_, n_] := (*effective*)SI[.24 * w * (L Meter) * t2 (ro3 * n + ro2)]
wo[L_, n_] := Convert[ $\sqrt{\text{SI}[\frac{k[L, n]}{m[L, n]}] * \text{Second}^2, 1}$ ] Hertz;

Plot[{ $\frac{wo[L, .0625]}{\text{Hertz}}$ ,
       $\frac{wo[L, .25]}{\text{Hertz}}$ ,  $\frac{wo[L, .6]}{\text{Hertz}}$ ,  $\frac{wo[L, 1]}{\text{Hertz}}$ }, {L, .009, .0225},
Frame -> True, FrameLabel -> {"L (m)", "wo in Hertz"},
AxesOrigin -> {.01, 200}, PlotStyle -> {Dashing[ {.1, .1}],
      Dashing[ {.05, .05}], Dashing[ {.01, .05}], RGBColor[0, 0, 0]},
PlotLegend -> {"n = .0625", "n = .25", "n = .6", "n = 1"},
LegendPosition -> {1, -.5},
LegendShadow -> None, LegendSize -> {.5, 1},
PlotRange -> {{.01, .015}, {200, 530}}, PlotLabel ->
  "Resonant Frequency vs Length (in efficient length range)"];

```

Resonant Frequency vs Length (in efficient length range)



■ Estimate for Deflection due to constant  $1.269 * 10^{-6}$  amplitude temperature vibrations.

Using lab data to approximate  $I_0$ , temperature fluctuations between  $1.269 * 10^{-6}$  Kelvin, and  $1.295 * 10^{-6}$  Kelvin were calculated for the 2.25 cm four – layer reed. Below is the corresponding deflection :

```
z[delt_] := 3 * (alpha3 - alpha2) *  $\frac{(t2 + t3)}{t2^2 * K}$  * L^2 * delt;
```

```
delt = 1.295 * 10-6 Kelvin - 1.269 * 10-6 Kelvin
```

```
Convert[z[delt], Nano Meter]
```

```
2.6 * 10-8 Kelvin
```

```
0.0112923 Meter Nano
```

This is small compared to the ~ 1-10 nm measurements currently observed in the lab.

## Vita

Lieutenant Janine O. J. Wiggins was born in Wilkes-Barre Pennsylvania on May 28, 1975. She graduated from Plattsburgh High School in 1993 and entered undergraduate studies at the United States Air Force Academy in Colorado Springs, Colorado. She graduated with a Bachelor of Science Degree in Space Physics and was commissioned on 28 May 1997. In less than a month, she was married to her husband, Steven. She is currently a minister in the Church of the Living God International Incorporated. She entered the School of Engineering, Air Force Institute of Technology in August 1997.

Permanent Address:           1 Sacramento Dr # 13  
  Hampton, VA 23666

REPORT DOCUMENTATION PAGE			Form Approved OMB No. 0704-0188	
Public reporting burden for this collection of information is estimated to average 1 hour per response, including the time for reviewing instructions, searching existing data sources, gathering and maintaining the data needed, and completing and reviewing the collection of information. Send comments regarding this burden estimate or any other aspect of this collection of information, including suggestions for reducing this burden, to Washington Headquarters Services, Directorate for Information Operations and Reports, 1215 Jefferson Davis Highway, Suite 1204, Arlington, VA 22202-4302, and to the Office of Management and Budget, Paperwork Reduction Project (0704-0188), Washington, DC 20503.				
1. AGENCY USE ONLY (Leave blank)	2. REPORT DATE March 99	3. REPORT TYPE AND DATES COVERED Master's Thesis		
4. TITLE AND SUBTITLE OPTIMIZATION OF A MULTILAYER PHOTOTHERMAL SENSOR FOR INFRARED SPECTROSCOPY			5. FUNDING NUMBERS AF18509867HES01	
6. AUTHOR(S) Janine O. J. Wiggins, Lieutenant, USAF				
7. PERFORMING ORGANIZATION NAME(S) AND ADDRESS(ES) Air Force Institute of Technology 2950 P Street WPAFB OH 45433-7765			8. PERFORMING ORGANIZATION REPORT NUMBER  AFIT/GAP/ENP/99M-16	
9. SPONSORING/MONITORING AGENCY NAME(S) AND ADDRESS(ES) US ARMY ERDEC HQ CBDCOM ATTN SCBRD RTE/ E5554 Aberdeen Proving Ground MD 21010-5423			10. SPONSORING/MONITORING AGENCY REPORT NUMBER	
11. SUPPLEMENTARY NOTES Prof L. W. Burggraf, ENP				
12a. DISTRIBUTION AVAILABILITY STATEMENT Approved for public release; distribution unlimited			12b. DISTRIBUTION CODE	
13. ABSTRACT (Maximum 200 words) Tri-layer thermal diffusion modeling was applied to the optimization of a multi-layer reed sensor for use in a photothermal infrared detector. The multi-layer reed sensor deflects in response to increased temperature. Deflection, of angstroms or larger, is measured using an atomic force microscope. A newly developed thermal diffusion model for three layer reeds was combined with an existing two-layer cantilever model, in order to explore the effects of length, operating frequency, and layer thickness on signal to noise ratio. Model behavior is presented, and compared to laboratory results.				
14. SUBJECT TERMS Photothermal sensor, magnesium aluminate, multi-layer cantilever, vibration			15. NUMBER OF PAGES 111	
			16. PRICE CODE	
17. SECURITY CLASSIFICATION OF REPORT UNCLASSIFIED	18. SECURITY CLASSIFICATION OF THIS PAGE UNCLASSIFIED	19. SECURITY CLASSIFICATION OF ABSTRACT UNCLASSIFIED	20. LIMITATION OF ABSTRACT UL	